2012

Interferometric switches for transparent networks : development and integration

Jin-Wei Tioh
Iowa State University

Interferometric switches for transparent networks: development and integration

by

Jin-Wei Tioh

A dissertation submitted to the graduate faculty

in partial fulfillment of the requirements for the degree of

DOCTOR OF PHILOSOPHY

Major: Electical Engineering

Program of Study Committee:
Mani Mina, Co-Major Professor
Robert J. Weber, Co-Major Professor
Arun K. Somani
Gary Tuttle
Lawrence Genalo

Iowa State University

Ames, Iowa

2012

TABLE OF CONTENTS

LIST OF FIGURES

LIST OF TABLES

ABSTRACT

Magneto-optic devices are a potential enabler of better scaling, transparent networks that are bit-rate, protocol and format insensitive. Transparency is critical given the paradigm shift from connection-oriented communications to IP-centric packet switched data traffic driven by the influx of high bandwidth applications. This is made more urgent by the large and growing optical-electronic bandwidth mismatch as well as the rapid approach of device dimensions to the quantum limit.

Fiber-based switches utilizing bismuth-substituted iron garnets as Faraday rotators in Mach-Zehnder and Sagnac interferometer configurations are proposed, analyzed and characterized. The issues and limitations of these switches are investigated and efforts are undertaken to model and optimize the field generating coil impedance parameters. While alleviating the concerns associated with free-space switches and being compatible with contemporary optical networks, the performance of the fiber-based interferometric switches is still below theoretical limits and could be improved. Moreover, the discrete components of a fiber-based implementation engender scalability concerns.

In keeping with the spirit of Richard Feynman's lectures, the maturity of planar lithographic techniques that are widely used in microelectronics is leveraged to realize integrated versions of the fiber-based interferometric switches. The design, analysis, fabrication and characterization of these integrated switches are detailed herein, including the selection of a suitable material system, design of the waveguide geometry, creation and calibration of a fabrication process based on direct-write scanning electron-beam lithography as well as determination of the switches' fabrication tolerance.

While the larger waveguide cross-section of the microphotonic switches enables efficient coupling to fiber and greatly reduces geometrical birefringence, the weak confinement results in longer device lengths. Moreover, the small but finite birefringence induces some polarization dependence in switch performance. Consequently, compact and nominally non-birefringent nanophotonic versions of the interferometric switches are proposed and analyzed in the interest of further improving switch performance and scalability.

ACKNOWLEDGEMENTS

Appreciation is a wonderful thing. It makes what is excellent in others belong to us as well.

-Voltaire

First and foremost, I would like to thank Prof. Mani Mina who supported and advised me throughout my sojourn at Iowa State. He instilled in me and reinforced the value and importance of being a life-long learner, continually challenging and encouraging me since my undergraduate days. I am also grateful to Prof. Robert J. Weber for imparting his mastery of engineering, his wonderful ideas and his patience. I hold great esteem for his unfailing enthusiasm and physical insight. I am also deeply indebted to both Prof. Mina and Prof. Weber for giving me a tremendous amount of latitude in setting my own goals and seeking solutions to problems, yet remaining approachable and encouraging whenever I reached an impasse. Additionally, I am thankful to Prof. Arun K. Somani, Prof. Gary Tuttle and Prof. Lawrence Genalo who agreed to serve on my committee and oversee my work.

I feel it necessary to express my appreciation for my colleagues who have also been a great source of friendship; Rashmi Bahuguna, Nathan VanderHorn, Sasha Oster, Ryan Gerdes, Perry Li, Bruce Fu, Harry Cao, Saalini Sekar, Jacob Sloat, Jiwon Lee and many others. It has been my pleasure and privilege to work alongside each of you.

Last but not least, I would like to acknowledge my family for their tireless love and support over the years. My brother, Jin-Ning Tioh who is also at Iowa State, for his camaraderie and the unique companionship of a sibling. My parents, Ngee-Heng Tioh and Meng-Gek Lim, for working hard to provide me with the best opportunities in life, embodying the ideals I aspire to achieve and teaching me far more than mere words can express.

CHAPTER 1. PREAMBLE

John Donne stated in 1623 that "…No man is an island, entire of itself…" in Devotions Upon Emergent Occasions, Meditation XVII. Human beings do not thrive when isolated from others and thus his sermon underscores the immense importance of communication. Thus, it is no surprise that optical communication dates back to antiquity; from fire and smoke signals to signaling lamps, flags and semaphores.

One of the earliest documented optical networks is the Roman smoke signal telegraph, which dates back to 150 A.D. To keep pace with the rapid expansion of their empire the Romans developed a highly sophisticated network of towers within visible range of each other. This first optical network spanned a total distance of 4,500km and used smoke signals to relay military messages.

Another famous optical network is the Chappe optical telegraph network of the 18th century. The French revolution, epoch of the rise of capitalism, required France to defend itself from enemies both within and without. This situation highlighted the importance of high-speed, long distance communications and Claude Chappe, a former priest, designed and built the first optical telegraph. Spanning a distance of 200km, it linked Lille and Paris via a series of 15 towers space 12-25km apart. Each tower was equipped with telescopes and mechanical semaphore arms, which could be reconfigured to display 196 distinct characters. These were manually relayed by operators from tower to tower and peak message speeds of 3,000km/h were achieved. This network was highly successful and continued to expand until 1846, spanning 5,000km with 556 stations. Many concepts in modern networks, eg. flow control, error detection and synchronization had their inception in the Chappe telegraph (Holzmann & Pehrson 1994).

Samuel Morse ushered in the era of electrical communications in 1837 with the invention of the telegraph (Morse 1840). For the ensuing century, optical communications remained largely supplanted. Its comeback had roots in the 1870 demonstration of transmission of light by total internal reflection in a stream of water by John Tyndall, which marked the inauguration of research into the guided transmission of light. About a decade later, Alexander Graham Bell developed a voice transmission system, dubbed the photophone (Bell 1880), which employed free-space optics and had a range of 200m. Limited by line-of-sight requirements, it was not until the invention of both a powerful coherent optical source that could be modulated (lasers (Maiman 1960)) and a flexible, sufficiently low-loss transmission medium (optical fibers (Kao & Hockham 1966; Kapron, Keck & Maurer 1970)) that the tide was turned.

1.1 Modern Optical Communications

Contemporary optical fibers are a far cry from their original counterparts (see Figure 1). Due to their characteristics, modern optical communications utilizes the medium (1310nm) and long (1550nm) wavelength bands or transmission windows due to the least dispersion and attenuation in those windows respectively. The availability of sources and amplifiers at these wavelength windows is also an integral factor for communications purposes. The latest Zero Water Peak (ZWP) fibers manufactured using vapor-phase axial deposition removes the attenuation peak at 1383nm due to optical absorption and scattering by water ions. This opens up a very broad wavelength window spanning 1285-1625nm with an attenuation constant of 0.33dB/km at 1310nm, 0.31dB/km at 1383nm and 0.19dB/km at 1550nm (PureBand® Zero Water Peak Fiber Specification 2008).

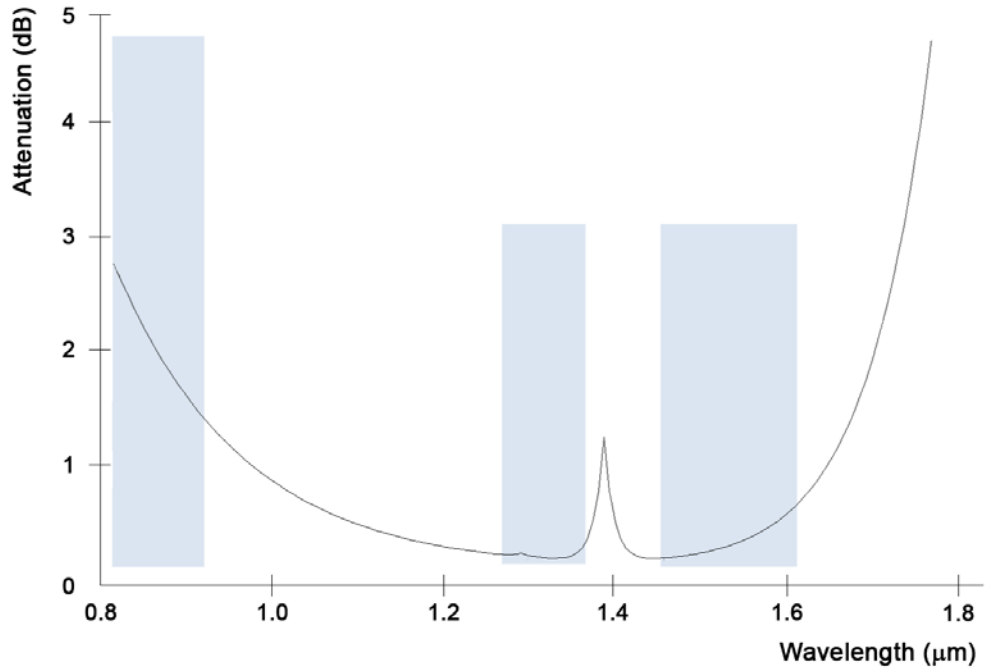

Figure 1 : Optical transmission windows. The curve is for modern fiber with a water attenuation peak at 1383nm.

Commensurate with the wavelength windows identified above, optical fibers have an enormous potential transmission capacity. The amount of information that can be transmitted is directly related to the frequency range over which the carrier operates. An increase in the carrier frequency theoretically increases the transmission bandwidth. Referring to Figure 1, it is seen that both the medium and long wavelength bands exhibit very low loss, around 0.4dB/km for the second window (medium wavelength, 1250-1350nm) and 0.2dB/km for the third window (long wavelength, 1450-1600nm). The useful wavelength range is therefore about 250nm.

Expressed in terms of analogue bandwidth, a 1nm waveband translates to a bandwidth of 178GHz at 1300nm and 133GHz at 1500nm. Thus optical fibers have a total usable bandwidth of approximately 30THz. The information carrying capacity depends on the modulation technique used. Assuming the widely used on-off keying format, which has a

maximum theoretical bandwidth efficiency of 1bps/Hz, one can expect a digital bandwidth of 30Tbit/s if fiber non-idealities are ignored. The removal of the water absorption peaks by ZWP fibers serves to further increase this already phenomenal figure.

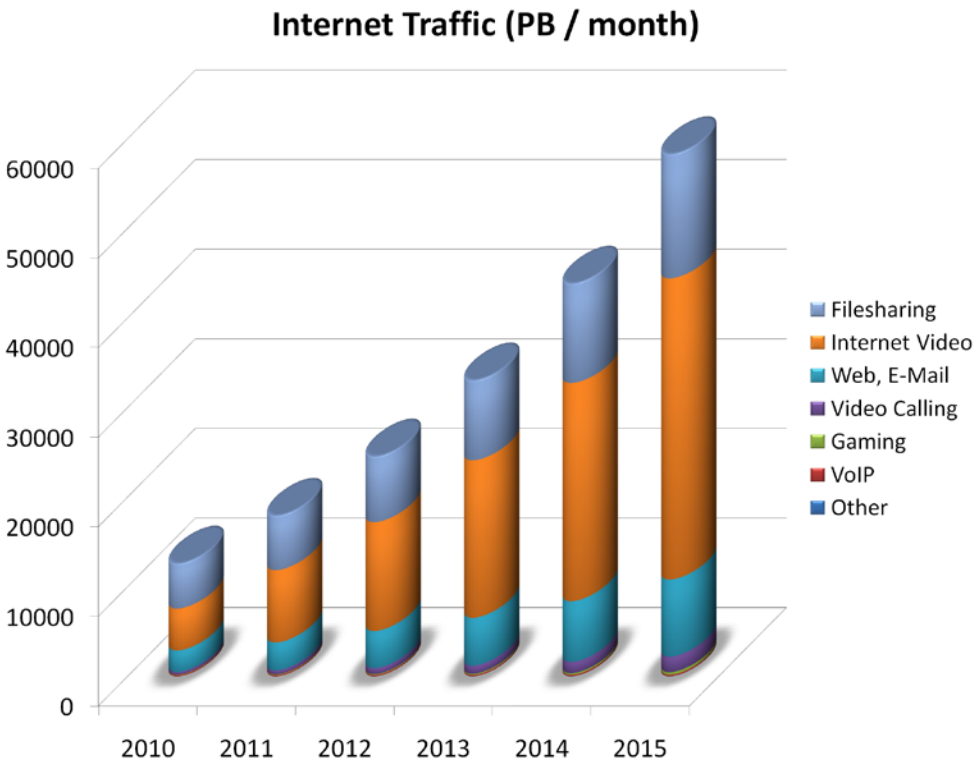

Figure 2 : Forecasted growth of global IP traffic.

Given the immense potential of optical fibers, it comes as no surprise that they are predominantly replacing copper as the transmission medium of choice, vastly increasing single-link bandwidth in the process. As shown in Figure 2, the past decade has witnessed a networking paradigm shift from connection-oriented communication to high bandwidth IP-centric packet switched data traffic, driven by the influx of high bandwidth applications (Cisco Systems Inc. 2011). Home entertainment applications such as HDTV are pushing the capabilities of current cable network technologies, video conferencing applications are

challenging current commercial network technologies and the growing complexity of commercial and military aircraft, including multifaceted sensor arrays and high definition flight displays, are pushing avionics networks to their limit.

The availability of such applications relies heavily upon the ability to transport data in a fast and reliable manner without significantly increasing operating and ownership costs. As these applications are pushing current network technologies to their capacity limits, researchers are being forced to create high-speed networks capable of supporting the varied bit-rates, protocols and formats required by these applications in a highly scalable manner.

A communications network is essentially an arrangement of physical links in which messages may be passed from one part of a network to another using either a single or multiple links. As modern networks continue to evolve in both size and complexity, new technologies have emerged to facilitate the most basic networking functions to efficiently utilize the potential of optical fibers; routing, switching and multiplexing.

1.2 Contemporary Networks

Wavelength-division multiplexing (WDM) technology was initially developed to increase the capacity of point-to-point fiber links. WDM enabled networks allow multiple opaque point-to-point connections to be established where the optical signal must undergo optical-electronic-optical (OEO) conversion at each intermediate node in the network. Network designers are able to occupy multiple wavelengths leading to increased bandwidth and fault tolerance while decreasing congestion and blocking.

A pressing concern in current commercial WDM implementations is the lack of network transparency. One can define network transparency based on the parameters of

the physical layer (bandwidth, signal-to-noise ratio, etc). It can also be the measurement of the signals remaining in the optical domain as opposed to interchanging between optical and electronic. Another issue is the type of signals the system can support including modulation formats and bit rates. The concept of an all-optical network is commonly defined as a network where the signal remains in the optical domain throughout the network. Transparent networks are attractive due to their flexible capabilities as well as higher data rate. A network is considered opaque if it requires its constituent nodes to be aware of the underlying packet format and bit rate.

The lack of transparency is a pressing concern in current networks as the need to handle data streams in the electrical domain engenders a large optical-electronic bandwidth mismatch (Sabapathia & Sundaravadivelub 2010). The bandwidth on a single wavelength is 10Gb/s (OC-192 / STM-64) today and is likely to exceed 100Gb/s (OC-3072 / STM-1024) in the near future. The enabling technologies for electronic processing of data at such high speeds are both costly and underdeveloped. Moreover, electronics will be hard-pressed to keep pace with the optical data rate as it spirals upwards since device dimensions are fast approaching the quantum limit (Powell 2008).

An additional concern associated with the requirement of high-speed electronics is the prohibitive cost of infrastructure upgrades. For instance, if a legacy switch operating at 2.5Gbps is present anywhere in the core network, all data passing through that switch is limited to data rate of 2.5Gbps. Any network upgrade requires the replacement of all legacy equipment (a "forklift upgrade"), which involves the massive overhaul of existing infrastructure. All-optical networks avoid this problem as the data rate is only limited by the end station capabilities. Thus, connection upgrades do not require changes in the core,

enabling metro operators to scale their networks to meet customer requirements and enhance their services.

Finally, current WDM implementations lack sub-wavelength granularity. Once a lightpath is established the entire wavelength is used exclusively by the connection's source-destination pair; no sub-wavelength sharing between nodes along the lightpath is allowed. Given the bursty and highly variable nature of IP traffic, underutilization of wavelength capacity tends to occur unless the source and destination nodes efficiently aggregate traffic.

1.3 Next Generation Networks

With the advancement of device implementation technologies, it is possible to design all-optical networks in which optical signals on an arriving wavelength can be switched to an output link of the same wavelength without conversion to the electronic domain. Signals on these all-optical networks can be of different bit rates and formats as they are never terminated inside the core network. This bit rate, format and protocol transparency is of vital importance in next generation optical networks. Several optical networking switching techniques have been proposed as possible solutions, which are discussed below.

1.3.1 Optical Burst Switching (OBS)

OBS was introduced into the industry as the first step towards eliminating dynamic switching elements that must decode each packet to make a routing decision from inside the network core (Qiao & Yoo 1999). It is a switching concept, which lies between circuit and packet switching. Operating at the sub-wavelength level, it is designed for better wavelength utilization by rapidly setting up and tearing down lightpaths for incoming traffic bursts. These

lightpaths are established by configuring the switches along the desired path using a control packet after which data packets follow after a guard time delay.

One disadvantage of OBS is that intermediate nodes are denied access to the wavelength path. This reserves resources along the entire burst path and can lead to network underutilization. Additionally since the constant reconfiguration of optical switches is required for provisioning networks on a per-burst level, there is a lack of implementation technology to enable practicable ratios of burst length to lightpath setup time. Thus OBS offers little advantage over traditional circuit and packet switching schemes involving OEO conversion.

1.3.2 Multiprotocol Label Switching (MPLS)

MPLS was developed as a packet-based technology to service converged data and voice networks by essentially gluing connectionless IP to connection-oriented optical networks (Callon et al. 1997; Rosen, Viswanathan & Callon 1997). It can be used to carry many different kinds of traffic, including native ATM, SONET, and Ethernet frames. MPLS is similar to OBS in that it involves the establishment of a lightpath between edge nodes (the point connecting a MPLS and non-MPLS enabled router) for a given traffic flow. However, MPLS differs from OBS in its provisioning mechanisms, using small identifiers that are either implicit or explicitly placed in traffic termed labels. These labels allow MPLS enabled routers to create a label switched path that is transparent from source to destination in which intermediate routing decisions can be made more efficiently. The provisioning timescale is on the order of hours or days depending upon the availability of network resources and connection requirements.

Although relaxing the switching element speed requirements compared to OBS, MPLS still suffers from an inability to provide sub-wavelength granularity and denial of access to intermediate nodes.

1.3.3 Optical Packet Switching (OPS)

OPS is the true optical equivalent of electronic packet switching, reading the embedded packet header information to make switching decisions. It thus offers the ability of true IP-over-WDM, operating in a connectionless fashion. This offers the key advantage of flexible and efficient utilization of the immense bandwidth of optical fibers and facilitates network support for more diverse services.

Current OPS implementations include the European Advanced Communications Technology and Services KEOPS (Keys to Optical Packet Switching) project (Guillemot et al. 2000) in which electronic header processing and control is employed for switching decisions. Native OPS implementations require optical domain buffering and switching. The only current realizable approach for buffering is the use of fiber delay lines, which requires an impractical fiber length of 200m at 10Gbit/s for a single Ethernet frame. As alluded to earlier, while all-optical switch implementation technologies have been suggested the severe speed requirements for switching on packet timescales makes a non-OEO OPS implementation highly unlikely at this point in time.

1.3.4 Light-trail (LT)

The concept of LTs was first proposed by (Gumaste & Chlamtac 2003) as an enhanced all-optical networking architecture and protocol that addresses the shortcomings of OBS, MPLS and OPS. LTs attempts to alleviate the problems associated with sustaining

IP-centric communication at the optical layer by side-stepping the requirement of costly and restrictive OEO switching at intermediate nodes and thereby offering complete signal format, bit-rate and protocol transparency. It achieves sub-wavelength granularity by allowing the dynamic establishment of an optical circuit between any chosen source and destination nodes in which the intermediate nodes can still access the shared channel without the need for optical switch reconfiguration or OEO conversion. Another benefit stemming from the shared channel is the inherent capability of multicasting, a crucial network capability for "bandwidth-killer" applications, eg. push media, file distribution and caching, interactive distance education, resource discovery and data collection.

LTs also aim to minimize the amount and speed requirements of active switching components by allowing intermediate nodes to use pre-established optical circuits. In this manner, connections are not constantly being setup and torn down, but rather exist for as long as they are being used by any of the nodes along the LT. This coupled with the dynamic provisioning of connections effectively offers a "bandwidth on demand" feature, which aids the network immensely in efficiently handling the bursty and highly variable nature of IP traffic as opposed to conventional circuit-switched networks. Since provisioning occurs on a time scale longer than burst or packet switched networks the speed requirements of the switching elements are relaxed, enabling LTs to avoid the pitfalls of immature implementation technologies.

A LT can be viewed as a unidirectional optical bus between a head and end node with the additional characteristic that intermediate nodes along the path retain access to the bus. This is in stark contrast to conventional architectures where communications is restricted to source-destination node pairs. The LT protocol utilizes an out-of-band communication channel, which is dropped and processed at each node. This channel

carries information pertaining to the setup and dimensioning of LTs and is responsible for provisioning connections within existing light-trails and assisting media access control.

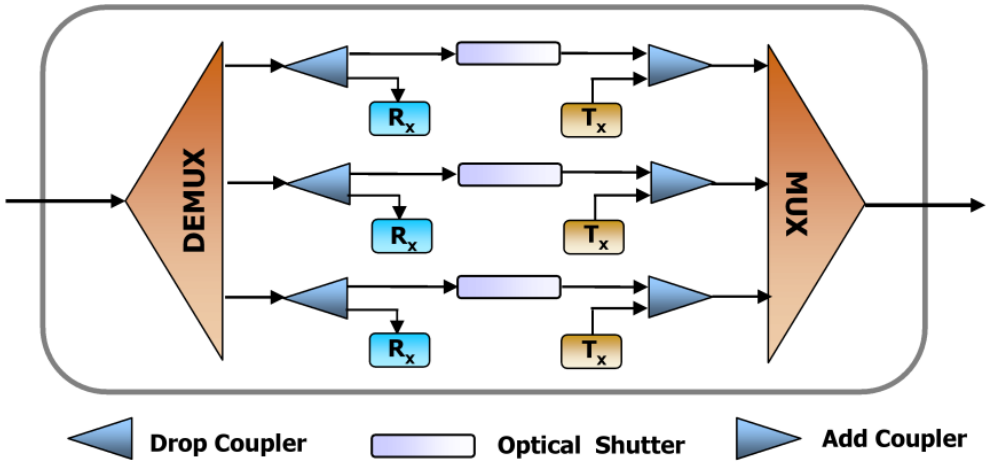

Figure 3 : Multiple wavelength LT node.

Figure 3 illustrates a typical node in a multiple wavelength LT network. Each node consists of wavelength multiplexers and demultiplexers as well as multiple LT access units (LAUs). Each LAU is comprised of optical couplers to enable each node to tap a sufficient amount of power for processing and source local data as well as an optical shutter to control the initiation and termination of LTs. An out-of-band electrical signaling channel controls the shutters.

An example single wavelength four node LT is shown in Figure 4. The head and end nodes have their shutters in the OFF state while intermediate nodes allow the optical signal to propagate down the bus unimpeded. This isolates the specific trail operational wavelength from the rest of the network, allowing wavelength reuse via spatial diversity. During operation the first three nodes are permitted to send information (bursts or time differentiated lightpaths) to any of their respective downstream neighbors without the need

for any optical switch reconfiguration. Thus, it is seen that a LT of N nodes supports connection between *N! / (2! (N-2)!)* different source-destination node pairs within the LT.

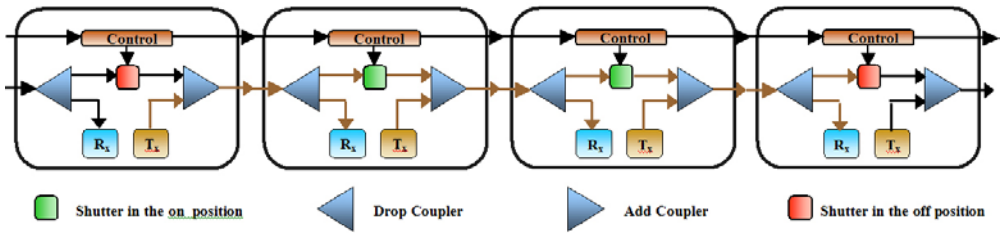

Figure 4 : A four node LT showing the primary LAU components.

Examining the operation of the simple LT in Figure 4 underscores the virtual topology defined by the combination of multiple LTs, which may be embedded over a physical network and hence form a more general IP framework. Additionally, while the unidirectional nature of the LT may appear to be a disadvantage, it is actually quite well suited to the asymmetric traffic patterns that are prevalent on the Internet.

1.4 All-optical Switches

Optical switches are useful for a great variety of photonic applications. In optical communications, they can be broadly classified as either opaque or transparent depending on their implementation technologies. Opaque switches, also billed as optical cross-connects, convert the incoming optical signals into electrical form. The actual switching is then performed electronically using a switching fabric with the resultant signals converted back to optical form at the output. Conversion to the electrical domain offers several advantages including regeneration, free wavelength translation, as well as performance and fault management. However, the presence of OEO conversions brings with it the aforementioned complications.

Transparent switches, also billed as photonic cross-connects, do not perform any OEO conversions. This allows them to function independent of the data type, format or rate, albeit only over a range of wavelengths termed the passband. Researchers have been exploring different ways of supplanting the electronic switch fabrics present in current commercial optical networks. Viable photonic cross-connect technologies should demonstrate superiority in switching speed, extinction ratio, scalability, insertion loss, polarization-dependent loss, crosstalk and power consumption.

The main switch technologies are microelectromechnical systems, acousto-optic, electro-optic, thermal-optic and magneto-optic. The technologies discussed below have individual niche areas and it is highly likely that they will co-exist on networks as each type represents different engineering trade-offs.

1.4.1 Microelectromechanical Systems (MEMS)

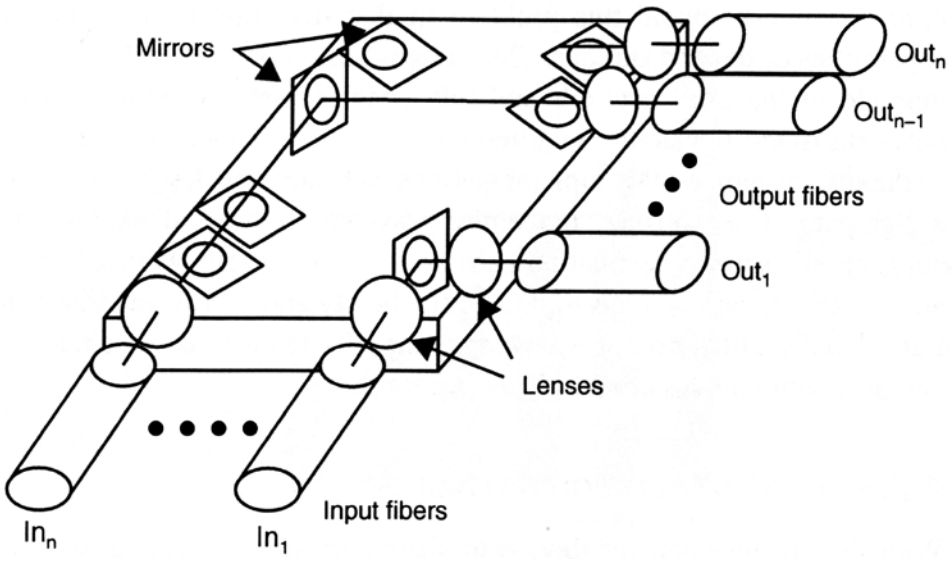

Figure 5 : Example crossbar 2D MEMS switch.

MEMS is a powerful means of implementing optical switches due to its unique capability of integrating optical, mechanical and electrical components onto a single wafer. MEMS switches use micro-mirrors that redirect light beams to the desired output port (Abdulla et al. 2011; Chen et al. 2010; Suzuki et al. 2008). They vary in the actuation mechanism used; electrostatic vs. magnetostatic, latching vs. non-latching and can be further categorized into either 2D or 3D MEMS. 2D switches are easier to control and have less forgiving tolerances but do not scale up as well due to optical loss. 3D switches alleviate the scalability problem by allowing movement on two axes but consequently have much tighter tolerances. MEMS switches tend to suffer from higher insertion losses due to beam divergence (~3dB), slower switching times (ms), high actuation voltage / current requirements and higher power dissipation for non-latching configurations (~80mW). An example 2D MEMs switch is shown in Figure 5.

1.4.2 Acousto-optic

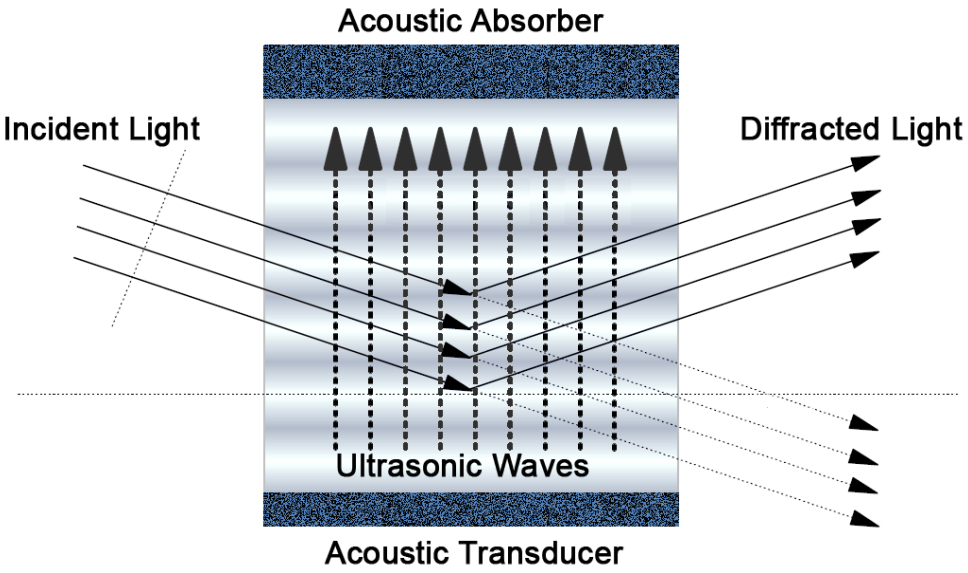

Figure 6 : Creation of diffraction grating by ultrasonic waves.

Acousto-optic switches are based on ultrasonic waves travelling within a crystal or planar waveguide that deflect light from one path to another (Aubin et al. 2004; Park et al. 2001; Sapriel et al. 2002) as illustrated in Figure 6. Mechanical vibration introduces regular zones of compression and tension within a material. In most materials this causes changes in the refractive index. This periodic pattern of refractive index changes forms a diffraction grating that causes the incoming light to be diffracted. Control of the ultrasonic wave amplitude and frequency enables control of the amount and wavelength of light that is diffracted. Acousto-optic switches are able to handle high power levels and offer reasonable insertion losses (~3dB) and switch times (~40μs) but suffer from poor isolation (~-20dB) and power efficiency as well as inherent wavelength dependency.

1.4.3 Electro-optic

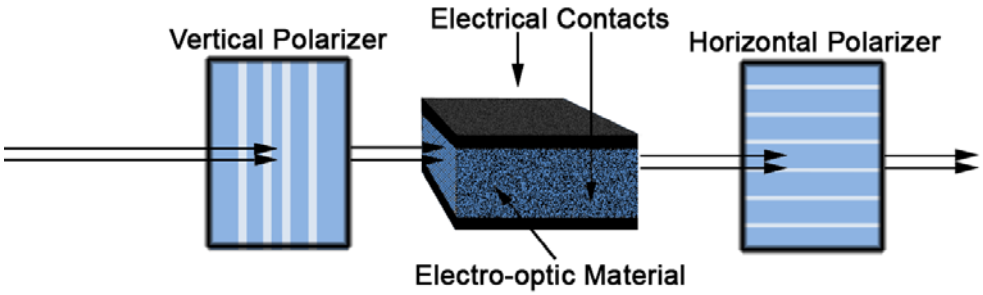

Figure 7 : Electro-optic modulator using $LiNbO_3$ crystal.

Electro-optic switches take advantage of the changes in physical properties of materials caused by the application of a voltage. It is arguably the most mature technology available and switches have been implemented using liquid crystals, switchable waveguide Bragg gratings, semiconductor optical amplifiers (SOAs) and $LiNbO_3$ (Chen et al. 2011; Donisi et al. 2010; Kuratani & Kadota 2010; Wang et al. 2011). An electro-optic switch using

$LiNbO_3$ to affect a change in the refractive index of the material that varies linearly with field strength is shown in Figure 7. Depending on the variant, they offer switch times from 10ns – 1ms, isolations of -10 – -40dB and insertion losses ranging from < 1 – 10dB. However most of them have a strong wavelength dependency and those that do not require higher driving voltages. SOA-based switches also suffer from a limited dynamic range, potentially creating cross-modulation and inter-modulation.

1.4.4 Thermal-optic

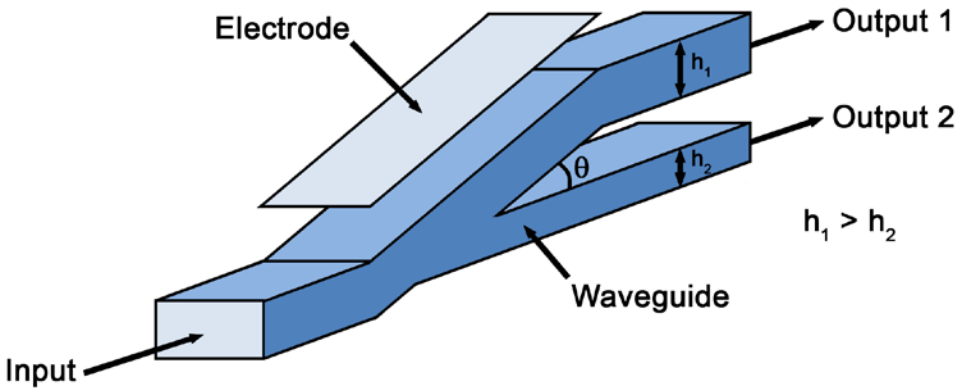

Figure 8 : Digital thermo-optic waveguide switch.

Thermal-optic switches are based on either the waveguide thermo-optic effect or the thermal behavior of materials (Al-Hetar et al. 2011; Hasizume et al. 2010; Zhong et al. 2007). Interferometric thermal-optic switches heat the material in one of the interferometer legs to generate a phase shift relative to the other leg, leading to interference effects between the two light beams when they are recombined. Digital thermal-optic switches utilize the interaction of two silica waveguides on silicon as shown in Figure 8. Heating the material changes the refractive index of the waveguide, imparting a phase difference and

thereby altering the selectivity of the output ports. While having excellent polarization-dependent loss, they consume more power due to the heating process (~70mW) and have a slow switch time (~10ms).

1.4.5 Magneto-optic

Magneto-optic switches are based on the Faraday rotation of polarized light when it passes through a magneto-optic material in the direction of an applied field. Changing the polarization of an electromagnetic wave is an indirect method of controlling the relative phase of its constituent orthogonal components. One method of achieving this is via the exploitation of the Faraday effect in a magneto-optic material, which rotates the state of polarization by the Faraday rotation angle θ_F. Magneto-optic switches use an interferometer to convert this phase modulation to an amplitude modulation and hold the distinct advantage of having high-power handling capability.

While some work has previously been done investigating these types of switches (Didosyan, Hauser & Reider 2002), the work was hampered due to the lack of sufficiently high quality magneto-optic materials. Recent advances in bismuth-substituted iron garnets and orthoferrites (Bolduc et al. 2006; Fratello, Licht & Brandle 1996; Kalandadze 2008; Nomura et al. 2011; Shaoying et al. 2007; Tkachuk et al. 2009; Zhang, Yang & Bai 2011) have yielded materials with a high magneto-optic figure of merit, giving low insertion losses, ultrawide bandwidths and more rotation for less applied field. Given these advances, this discourse focuses on the development and integration of magneto-optic switches for next generation, transparent networks.

.

CHAPTER 2. MAGNETO-OPTICS

Michael Faraday made the fundamental discovery of the first relationship between light and magnetism in 1845 (Faraday 1855). He demonstrated that the vibration plane of light is rotated when the light passes through certain magnetisable bodies along the lines of force. In his last experimental work, Faraday attempted unsuccessfully to detect the effect of a magnetic field on the spectral lines emitted by sodium vapor, with the best available magnet and spectroscope.

Half a century later, Pieter Zeeman, while studying the Kerr phenomenon was induced by “reasons of minor importance” to try to detect a magnetically induced change in the light of a sodium flame. Although initially failing, his attention was subsequently drawn to Maxwell’s sketch of Faraday’s life, in which Faraday’s last experiment is mentioned. "If a Faraday thought of the possibility of the above mentioned relation, perhaps it might be yet worthwhile to try the experiment again with the excellent auxiliaries of spectroscopy of the present time." Finally, using an improved grating and 10kGauss Ruhmkorff magnet, Zeeman successfully observed a broadening of the spectral lines emitted by sodium vapor (Zeeman 1897).

Since these pioneering discoveries, magneto-optics has become a captivating field of research, finding a great many scientific and practical applications (Gao, Li & Niu 2010; Ghosh et al. 2008; Kikkawa & Awschalom 2008; Moses, Williams & Hoshtanar 2005; Panmand et al. 2011; White, McHale & Goerz 2010). In optical networking, magneto-optic devices are a potential enabler of better scaling, transparent networks that are bit-rate, protocol and format insensitive. This chapter provides the theoretical foundation for understanding magneto-optic phenomena.

2.1 Polarization

Polarization is a property ascribed to electromagnetic waves that describes the orientation of their field vectors. Thus a study of the polarization of light denotes an investigation into how the field vector associated with the wave temporally evolves at a fixed point of space. If this evolution is the same in every point of space, the field is said to be polarized. The standard convention is to only consider the electric field vector as the magnetic field vector is both proportional and perpendicular to it.

As a three dimensional object, an electromagnetic wave can be considered to be a superposition of its two orthogonal components orientated in a plane perpendicular to the propagation direction (Pedrotti, Pedrotti & Pedrotti 2007). If propagation in the Z direction is assumed, the single frequency (or time harmonic) wave can expressed as :

$$\vec{E} = \vec{a}_x E_{0x} \cos(\omega t - \beta z) + \vec{a}_y E_{0y} \cos(\omega t - \beta z + \phi) \tag{2.1}$$

These components are oscillating in time with the same frequency. Depending on the X and Y component magnitudes and the value of the relative phase shift ϕ between the two orthogonal components, the propagating wave is said to be either linearly, circularly or elliptically polarized. A linear polarization results if the two components are in phase, ie. $\phi = 0^o \pm n180^o$. They add at every plane to give an electric vector that has a fixed direction determined by the relative amplitudes of the components. The designation *linear* stems from the fact that the electric vector maintains its direction in space.

A circular polarization results if the relative phase is an odd multiple of 90^o, ie. $\phi = 90^o \pm n180^o$ and the component amplitudes are equal. Looking in the direction of propagation, $\phi < 0^o$ leads to a clockwise sense of circular polarization, which is also termed

right circularly polarized. Conversely, $\phi > 0^o$ leads to a counterclockwise sense of circular polarization, which is also termed left circularly polarized.

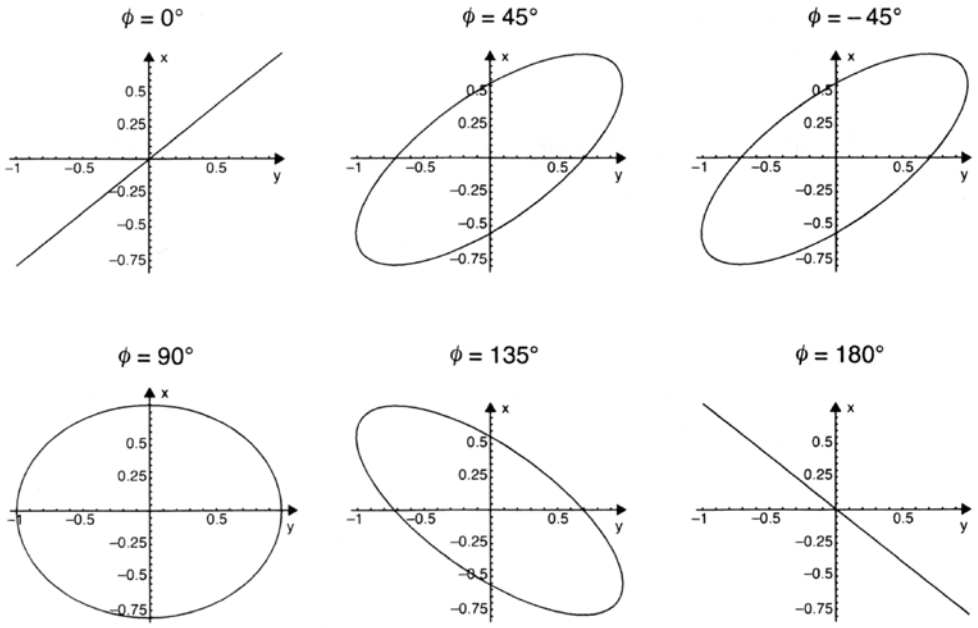

Figure 9 : Example Lissajous figures plotted for an amplitude ratio of 0.75 and various relative phases.

The most general case, which occurs for all other combinations of component amplitudes and relative phase is an elliptical polarization. Figure 9 illustrates the influence of the relative phase on the resulting Lissajous figures for fixed, unequal amplitudes. Linear and elliptical polarizations are shown. Circular polarization would have occurred when $\phi = 90^o$ if the component amplitudes were equal.

Pragmatically speaking, changing the polarization of an electromagnetic wave is an indirect method of controlling the relative phase of its constituent orthogonal components. In the devices investigated in this work, this change is affected via the Faraday effect.

2.2 Faraday Effect

The Faraday effect was the first experimentally observed magneto-optic effect and originates from the interaction between light passing through or reflecting from a medium and the electron spin due to the spin-orbit coupling. It is manifested as a different response of the electrons to left and right circularly polarized light. This is further detailed in (Kahn, Pershan & Remeika 1969).

The macroscopic theory of magneto-optic effects originate from the use of Maxwell's equations for material media, which are approximate in that spatial averages are taken over volume elements that are large compared to the interatomic dimensions (Lorentz 1915; Van Vleck 1932). The propagation of electromagnetic waves through an optically isotropic insulator is described by the solutions of the Maxwell equations and use of the constitutive relations :

$$\nabla \times \vec{E} = -\frac{\partial \vec{B}}{\partial t} \tag{2.2}$$

$$\nabla \times \vec{H} = \vec{J} + \frac{\partial \vec{D}}{\partial t} \tag{2.3}$$

$$\vec{B} = \mu \vec{H} \tag{2.4}$$

$$\vec{D} = \varepsilon \vec{E} \tag{2.5}$$

From a mathematical point of view, magneto-optic effects could be derived from either a permeability or permittivity tensor. However, due to the inertia of the magnetization process at optical frequencies, the gyromagnetic effects described by the permeability tensor are negligible, ie. μ is very close to unity and assumed to be a simple scalar (Landau & Lifschitz 1984). Thus ε now becomes a second rank tensor containing both the gyrotropic and birefringent properties of the material :

$$\varepsilon = \begin{bmatrix} \varepsilon_{xx} & -j\varepsilon_{xy} & 0 \\ j\varepsilon_{xy} & \varepsilon_{yy} & 0 \\ 0 & 0 & \varepsilon_{zz} \end{bmatrix} \tag{2.6}$$

where the direction of either the applied magnetic field or material magnetization is taken as the Z-axis. Generally speaking, all the permittivity tensor elements are complex and completely describe the optical behavior of the material; the imaginary portion describing its absorption behavior and the real portion describing the effect of such behavior on the refractive index. The diagonal elements (ε_{xx}, ε_{yy} and ε_{zz}) are usually weak functions of the applied magnetic field (or magnetization) and assumed to be constants. Thus, they represent the optical properties of the material in the absence of magneto-optic effects. The justification for treating the diagonal elements as constants stems from their origin due to small distortions in cubic symmetry. The symmetry perturbations induce additional birefringence, which has the effect of making the material biaxial and this is phenomenologically described by changes to the diagonal tensor elements. However, this birefringence is small and can usually be ignored, depending on the specific material being considered. Conversely, the off-diagonal elements have a first order linear dependence on the applied magnetic field (or magnetization) and are the source of the majority of magneto-optic effects that are considered in this work.

Depending on the boundary conditions set by the specific application, the Maxwell equations combined with Equation 2.6 describe the transmission and reflection characteristics of the material (Hunt 1967). The influence on the intensity and polarization of light impinging on the material constitutes the magneto-optic effects and are classified as either the Faraday effect (light transmission) or Kerr effect (light reflection). As a first step to

obtaining the magnitude of the magneto-optic effects, the plane wave solutions to Maxwell equations using the permittivity tensor as defined in Equation 2.6 are desired. The solutions can be expressed as specific polarization states (eigenmodes) that will propagate through the magneto-optic material unchanged and the eigenvalues are the effective refractive indices for these polarizations.

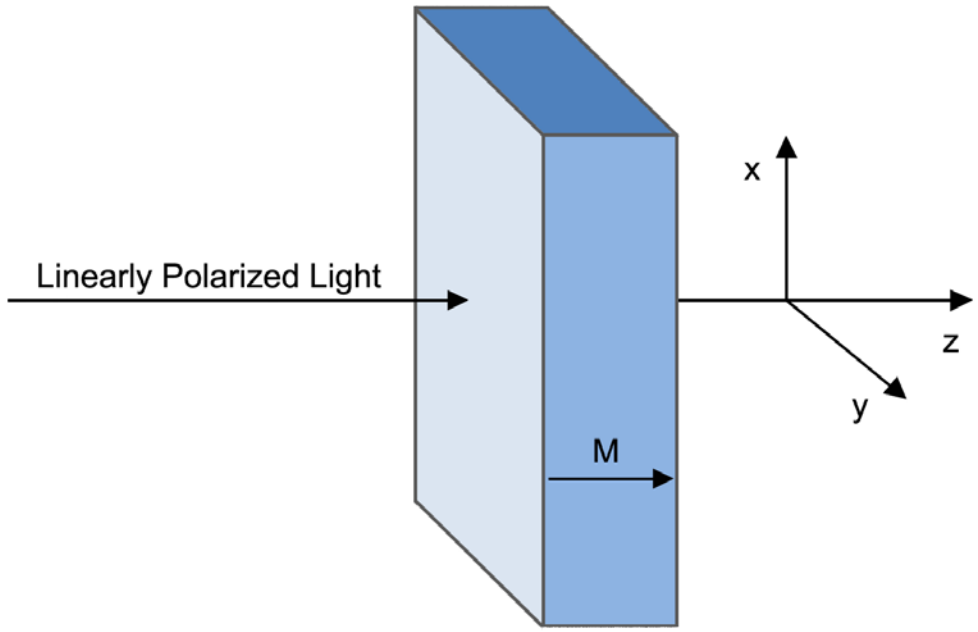

Figure 10 : Polar geometry of the Faraday effect.

In the case of rare earth iron garnets, light is assumed to propagate in a direction parallel to the applied magnetic field, which forms the polar geometry of the Faraday effect as shown in Figure 10. Additionally, the cubic symmetry perturbations mentioned earlier are neglected and it is assumed that $\varepsilon_{xx} = \varepsilon_{yy}$. Taken together, these assumptions imply that the garnets are being treated as having a single optical axis and that this axis coincides with both the direction of the applied magnetic field and light propagation vector. The

eigenmodes for this case are the left and right circularly polarized states with complex effective refractive indices given by :

$$n_{\pm}^2 = \varepsilon_{xx} \pm \varepsilon_{xy} \tag{2.7}$$

where n_+ and n_- are the effective refractive indices for the left and right circularly polarized states respectively. Faraday rotation arises from the real (dispersive) component of the difference in n_+ and n_-, where a phase difference develops between the left and right circularly polarized components of linearly polarized light that is transmitted through the magneto-optic material. This manifests itself as a rotation of the linear polarization by the Faraday rotation angle θ_F with the overall process illustrated in Figure 11.

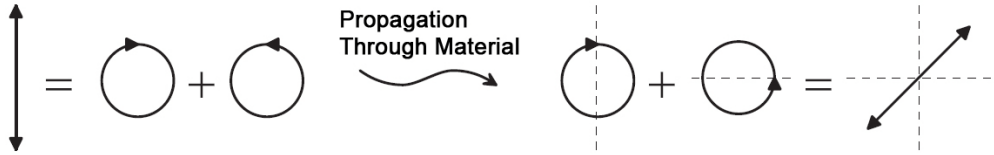

Figure 11 : Illustration of the Faraday rotation mechanism.

For light having a wavelength λ and a magneto-optic material of thickness *t*, the Faraday rotation is defined as :

$$\theta_F = \mathrm{Re}\left(\frac{\pi t(n_+ - n_-)}{\lambda}\right) = \mathrm{Re}\left(\frac{\pi t \varepsilon_{xy}}{\lambda\sqrt{\varepsilon_{xx}}}\right) \tag{2.8}$$

where positive rotation is defined according to the right-hand rule as shown in Figure 12. This rotation is non-reciprocal, which distinguishes it from optical activity. The sign of the rotation angle (with respect to a fixed reference frame) does not change when the direction

of propagation is reversed stemming from a sign change of the off-diagonal elements in Equation 2.6. This means that linearly polarized light making two passes in opposite directions accumulates $2\theta_F$ of rotation rather returning to its incident state, which is the principle relied on in devices such as optical isolators.

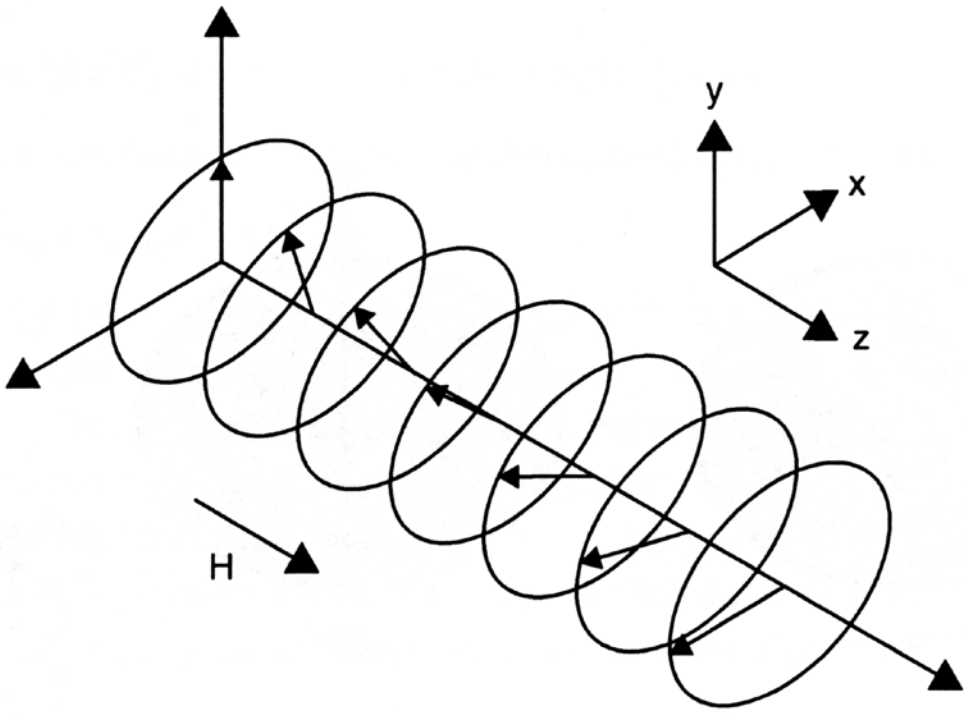

Figure 12 : Right-hand rule for Faraday rotation, defined as the electric field vector rotation of light propagation in the positive z direction.

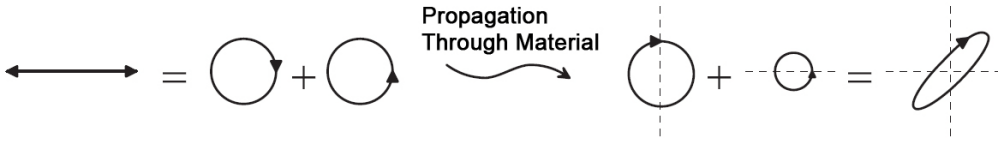

Figure 13 : Illustration of the Faraday ellipticity mechanism.

Although only the Faraday rotation is of interest as the working basis of an all-optical switch, it should be mentioned that the imaginary (absorptive) components of the difference

delinearizes the polarization of the incident light due to differing degrees of absorption for the left and right circularly polarized components. This manifests itself as Faraday ellipticity, which is defined as the imaginary components of the expression in Equation 2.8 and illustrated in Figure 13. Given garnets with sufficiently high magneto-optic figures of merit, they can be assumed sufficiently transparent that the absorptive components can reasonably be ignored. Additionally the analysis above neglects reflections at the magneto-optic material boundaries, which has a similar effect as the optical loss due to material absorption (Grzegorczyk & Kong 2005). Finally, different geometries give rise to the other magneto-optic effects such as the Kerr effect, magnetic linear birefringence and magnetic circular dichroism.

2.2.1 Quantum Numbers

Quantum mechanics (or wave mechanics) is embodied in the Schrödinger wave equation. In principle, the wave equation can be utilized to determine many aspects of sub-atomic phenomena. In practice however, the direct application of the Schrödinger equation presents enormous complexity when dealing with anything but the simplest atoms. Thus, quantum numbers were developed to aid in describing electron behavior. Schrödinger found that three variables would help establish specific aspects of electron behavior. These quantum numbers are designated n, l and m_l. Eventually, a fourth quantum number was added – the spin quantum number, s.

Table 1 lists the four quantum numbers together with their allowed values and function. n, the principal quantum number, has allowed integer values from 1 to ∞ and is the quantum number that mainly governs the energy of an electron, as well as the size of an electron orbital.

Table 1 : Atomic quantum numbers.

Quantum Number	Allowed Values	Function
n	1, 2, 3, …	Dictates the energy level and size of electron orbital
l	(*n*-1), (*n*-2), …, 0	Dictates the shape of the orbital and the angular momentum of an electron
m_l	$\pm l$, $\pm(l-1)$, …, 0	Dictates the behavior of orbital electrons in a magnetic field
s	+½	Dictates the magnitude of the spin angular momentum

l, the orbital (sometimes also called azimuthal) quantum number also has allowed integer values. However, these must be less than *n* and must be ≥ 0. Therefore if *n* = 1 for instance, *l* can be either 2, 1 or 0. *l* governs the shape of the orbital and the angular momentum of an electron as it circulates about the nucleus in its orbital. It is standard convention that the *l* = 1 orbital is termed the P subshell. Table 2 outlines the naming conventions for the orbitals, where S = Sharp, P = Principle, D = Diffuse, F = Fundamental, and with the subsequent orbitals just named alphabetically (ie. G, H, etc.).

Table 2 : Orbital / subshell names.

l	0	1	2	3	4	5
Orbital / Subshell Name	S	P	D	F	G	H

m_l, the magnetic quantum number, also has allowed integer values that are dependent on *l*. However, m_l can take negative integer values. Thus for *l* = 3 for instance, m_l can take the values of ±2, ±1 or 0. As its label implies, m_l denotes the behavior of electrons in orbitals when the atom is placed in a magnetic field as an electron "flowing" in an orbital

can be seen as akin to electrons flowing in a conventional current loop, which will have a magnetic moment. The direction of this moment is dictated by m_l.

s, the spin quantum number, only has a single allowed value of +½. It measures the spin angular momentum which the electron possesses whether it is present in an atom or in free space. An extremely important distinction is that *s* only specifies the magnitude of spin. Once a reference direction has been established by applying a magnetic field, the angular momentum vector can only point in a direction so that its components along the reference direction are half-integral multiples of $\hbar$, as illustrated in Figure 14. The reference direction in this figure is taken to be vertical, which by convention is utilized to define the z-axis. The component of $\boldsymbol{s}$ in this direction can be defined as $\boldsymbol{s_z}$, which is written as half-integral multiples of $\hbar$:

$$\mathbf{S}_z = s_z\ \hbar \tag{2.9}$$

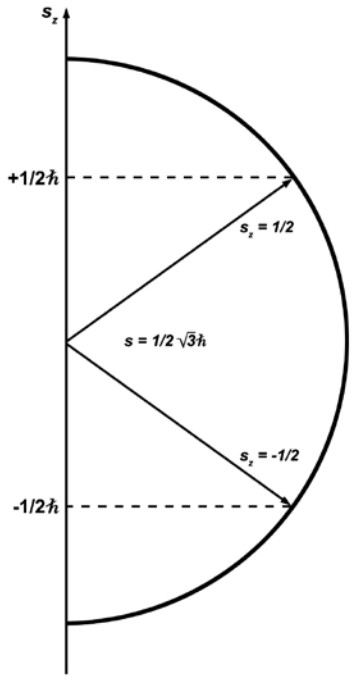

Figure 14 : Allowed spin angular momentum vector directions for an electron.

2.2.2 Many Electron Atoms

The Schrödinger wave equation dictates that electrons in atoms has to occupy similar orbitals as the S, P, D, F, … orbitals for the hydrogen atom, which is a single electron atom. The manner in which electrons occupy orbitals in large atoms (ie. many electron atoms) is of more interest here as magneto-optic materials are governed by ions that deal with unfilled 3D and 4F shells. This is governed by three principles :

1) Principle of minimization of energy
   Electrons tend to occupy the lowest possible energy state.

2) Pauli exclusion principle
   No two electrons in an atom can have a duplicate set of values for quantum numbers for n, l, m_l and s_z.

3) Hund's principle
   Electrons tend to occupy degenerate orbitals singly with their spins parallel. The most stable arrangement of electrons in orbitals / subshells is the one with the greatest number of parallel spins.

The Pauli exclusion principle effectively places a limit of two electrons in each orbital. For example, the 1S orbital and electron has $n = 1$, $l = 0$, $m_l = 0$. However, the electron is further characterized by its spin direction s_z. Therefore, two electrons ($s_z = +½$, $s_z = -½$) can occupy the 1S orbital. A third electron cannot exist in the same orbital without repeating a set of values. Thus the electron in question would have to "go" to another orbital and it would go to the next higher vacant or half-vacant orbital. The order of the energy levels are :

1S < 2S < 2P < 3S < 3P < 4S < 3D < 4P < 5S < 4D…

If the 1S orbital is full, an electron goes to the 2S orbital, and after this the 2P orbital, etc. Hund's principle dictates that when for instance, the $2P_x$ orbital already contains an electron, the next P electron will be in a different P orbital eg. $2P_y$. This maximizes the number of electrons with parallel spins.

$n = 2, \quad l = 1, \quad m_l = 1, \quad s_z = \pm ½$

$n = 2, \quad l = 1, \quad m_l = 0, \quad s_z = \pm ½$

$n = 2, \quad l = 1, \quad m_l = -1, \quad s_z = \pm ½$

The additional electrons in many-electron atoms contribute to the total angular momentum of the atom. This can be done via the Russell-Saunders coupling, and this has been shown to provide results inline with the spectra of small and medium-sized atoms. According to this method, the orbital and spin contributions are first summed separately, finally adding the total orbital and total spin contributions to get the total angular momentum of the atom :

$$\sum i_i = L \tag{2.10}$$

$$\sum s_i = S \tag{2.11}$$

$$L + S = J \tag{2.12}$$

Adding L and S gives the total angular momentum J. Unlike the total angular momentum j for a single electron atom, J can be either integral or half-integral, depending on S. If S is half-integral, J is half-integral and vice-versa. The expression for J is thus :

$$J = \sqrt{J(J+1)}\,\hbar \tag{2.13}$$

2.2.3 Atomic Model

The energy levels in atoms and molecules are quantized, ie. there are only discrete, allowed energy states where an electron can reside. Contributing to the energy of a particular energy state are the energy of position, arising by virtue of electron-nucleus and electron-electron interaction in the same atom, as well as the energy of motion, arising from the summed orbital and spin momenta of the electrons in the atom. Positional energy can be described in terms of the *n* and *l* quantum numbers, whereas that of motion depends on the m_l and s_z values of each electron and the way in which these are coupled.

Angular momentum can be considered as arising from a physical movement of electrons about the nucleus and, since electrons are charged, such motion constitutes a circulating electric current and hence a magnetic field. Its field can be represented by a vector μ - the magnetic dipole of the atom. μ is directly proportional to the angular momentum *J* and has the same direction. The electron is not treated as a point charge in quantum mechanics. The expression for μ is thus :

$$\mu = -\frac{ge}{2m} J = -\frac{ge}{2m} \sqrt{J(J+1)}\, \hbar \quad \text{(Joules/Tesla)} \tag{2.14}$$

where *g* is a “fiddle” factor - the Landé splitting factor. This factor depends on the state of the electrons in the atom and is given by :

$$g = \frac{3}{2} + \frac{S(S+1) - L(L+1)}{2J(J+1)} \tag{2.15}$$

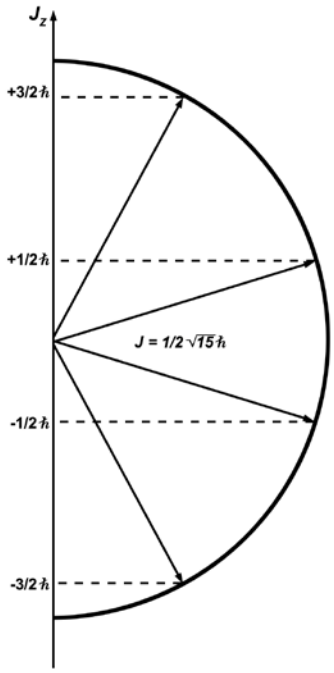

Figure 15 : The *2J+1* = 4 components of *J* are shown. In this case, *J* is half-integral (*J* = 3/2).

J can have either integral or half-integral components J_z along a reference direction, depending upon whether the quantum number *J* is integral or half-integral. This is shown in Figure 15 for a state with *J* = *3/2*, with 2*J*+1 number of components given by :

$J_z = J, J-1, \ldots, ½$ or $0, \ldots, -J$

The corresponding magnetic moment of each component is shown in Figure 16. Since it is known that *J* has components in the z-direction, and μ is proportional to *J*, μ will also have components in the z-direction given by :

$$m_z = -\frac{ge}{2m}\hbar J_z \qquad (2.16)$$

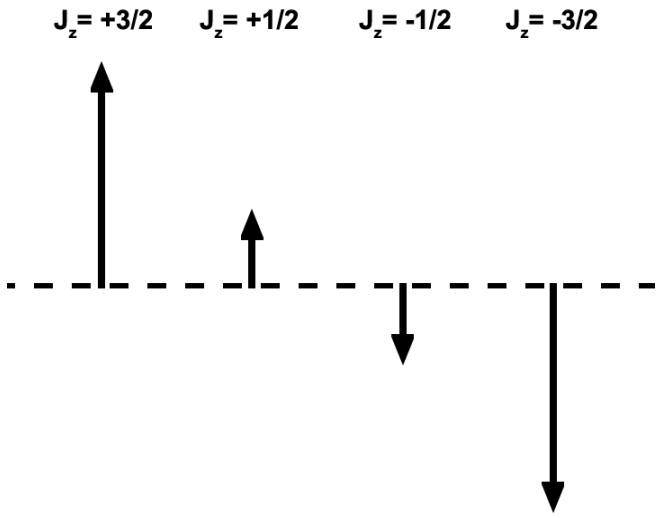

Figure 16 : The magnetic moment corresponding to each value of J_z.

If an external magnetic field is applied to the atom, thus actually establishing a z-direction, the z-component atomic dipole μ will interact with the applied field. Thus, if magnitude of the applied field is B_z, the interaction is simply just $\mu_z B_z$:

$$\Delta E = \mu_z B_z = -\frac{ge}{2m}\hbar B_z \tag{2.17}$$

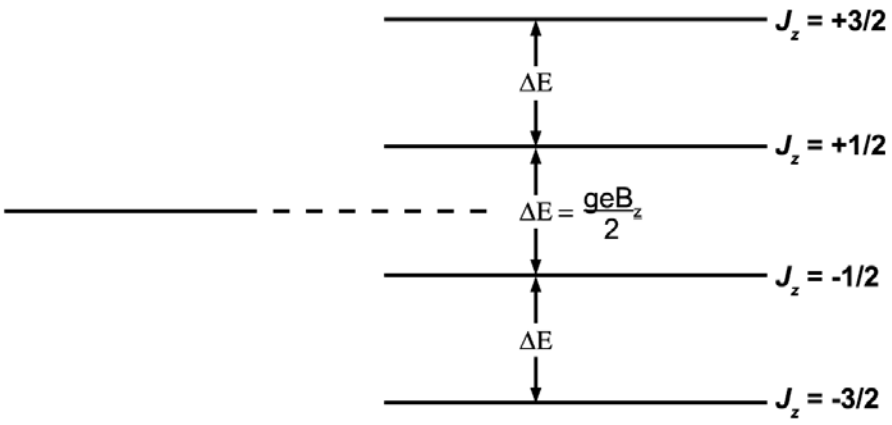

Figure 17 : The applied external field lifts the degeneracy of the quantum numbers, resulting in multiple discrete energy states/levels.

The interaction of the atomic dipole with the applied field can be represented with ΔE, since this splits the originally degenerate energy levels corresponding to the $2J+1$ values of J_z, into $2J+1$ different energy levels, lifting the degeneracy of J. This is illustrated in Figure 17, again for $J = 3/2$.

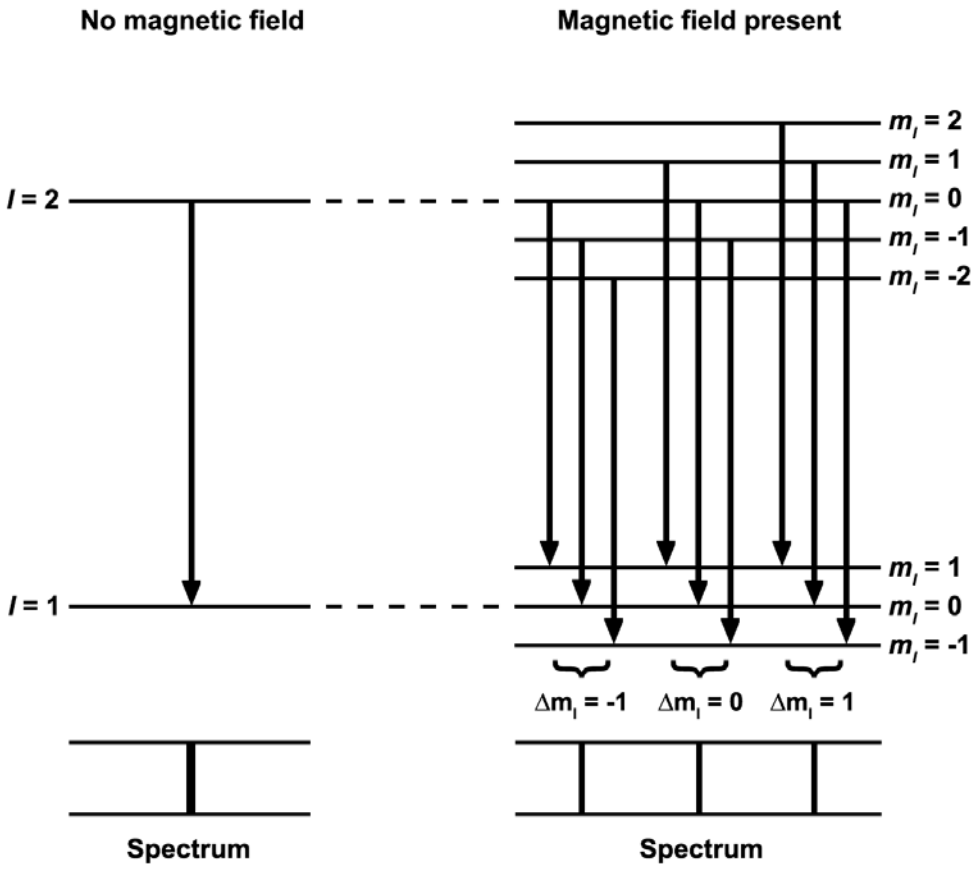

Figure 18 : Energy state transition diagram for the normal Zeeman effect.

This energy level splitting, or lifting of quantum number degeneracy on the application of an external magnetic field is the Zeeman effect and is illustrated in Figure 18. The Faraday effect is a corollary of this since the angular momentum and its z-axis projection for left and right circularly polarized photons are as follows :

RCP $j = 1$, m = +1

LCP $j = 1$, m = –1

These polarized photons will induce transitions of the ions in the magneto-optic material to the following states and result in different dispersion values for the left and right circularly polarized light, which is the operational basis of the Faraday effect.

RCP $\Delta J = \pm 1, 0$, $\Delta M = +1$

LCP $\Delta J = \pm 1, 0$, $\Delta M = -1$

2.3 Material

The material primarily considered for switch design is bismuth-substituted rare earth iron garnets. The unique properties of garnets that find use in engineering applications originate from their constituent elements and the interactions of these elements in the unit cell (Paoletti 1978). The general formula for garnets is denoted as $X_3Y_2Z_3O_{12}$, where X, Y and Z represent ions on a dodecahedral, octahedral and tetrahedral sublattice respectively as shown in Figure 19. Each oxygen ion is surrounded by either X, Y or Z sites and the unit cell is cubic, surrounded by 160 atoms – 96 O, 24 X, 16 Y and 24 Z sites. Naturally occurring garnets are always solid solutions of several different ions in each sublattice. Synthetic garnets can be made in an almost stoichiometrically pure form with only one ion species at X, Y or Z respectively and the number of possible constituents is large. A typical rare earth garnet contains iron and rare earth metal ions generally having the chemical formula $RE_3^{3+}Fe_2^{3+}Fe_3^{3+}O_{12}$, although other elements are introduced as dilutants to fine tune its properties. The rare earth ions are located at the dodecahedral sites and iron in the other two sublattices.

In the garnet structure the magnetic properties are directly affected by the kinds of ions which occupy a certain sublattice. The lattices couple with each other anti-ferromagnetically with the strongest interaction between the octahedral and tetrahedral sites and the weakest between the octahedral and dodecahedral sites. Thus the total magnetic moment of the garnet is the moment contributed by one iron ion minus that from the rare earth ions.

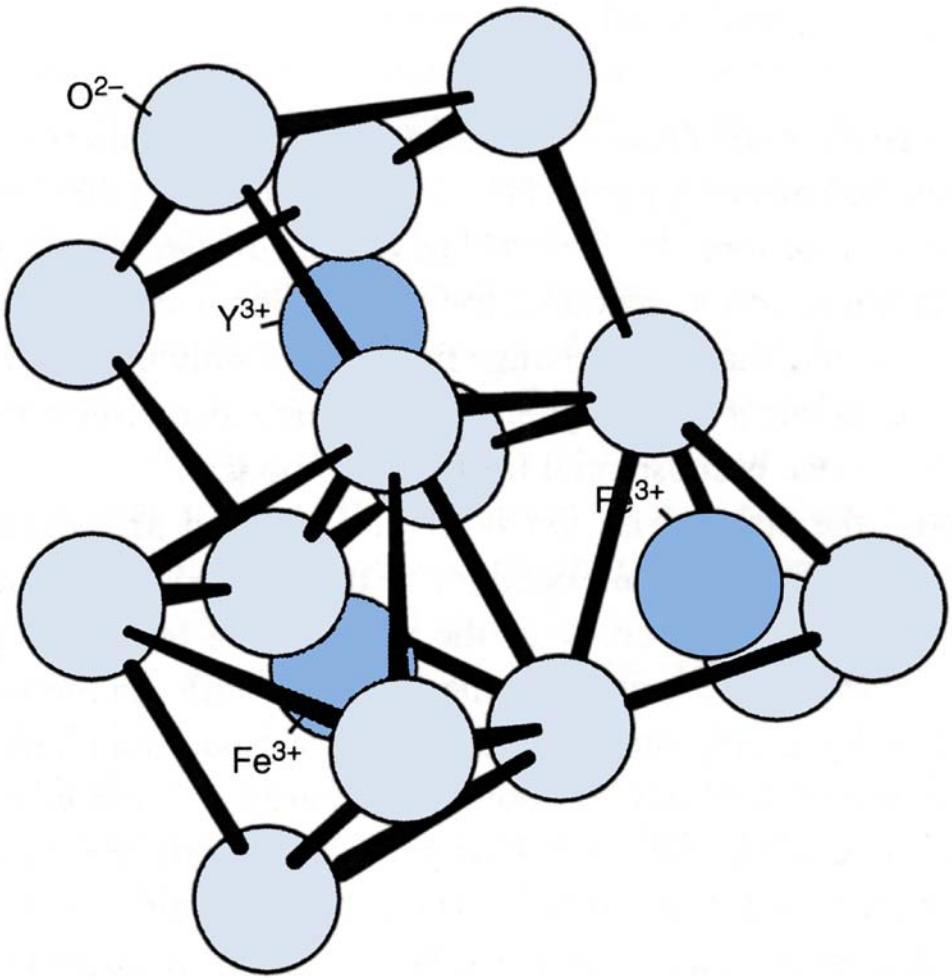

Figure 19 : Structure of a yttrium iron garnet ($Y_3Fe_5O_{12}$) unit cell.

Additionally, garnets have several easy magnetization axes due to their cubic structure. However engineering applications call for uniaxial anisotropy perpendicular to a surface of interest. This is achieved by growth anisotropy, which comes about from the phenomenon that rare earths prefer some lattice positions over others depending on material growth direction. The magnetic moments of these rare earths add up and effectively create anisotropy (Eschenfelder 1980).

In principle, the creation of a suitable material for magneto-optic applications merely involves choosing the proper species and amount of ions to occupy the different sublattices. As alluded to by the derivations in the previous section, magneto-optic applications require a high magneto-optic figure of merit, which is a measure of efficiency of a Faraday rotator defined as :

$$MOFM = \frac{Rotation\ /\ Length}{Absorption\ /\ Length} = \frac{\theta_F}{\alpha} \tag{2.18}$$

This encapsulates the need for a strong specific Faraday rotation at the application wavelength range coupled with low absorption. Early work indicated that the rotation found in garnets is enhanced by the introduction of bismuth and that this does not negatively affect its absorption characteristics for wavelengths longer than 600nm (Aichele et al. 2003; Takeuchi, Shinagawa & Taniguchi 1973). Thus the addition of bismuth is a way of increasing the magneto-optic figure of merit and this is usually done for the commonly used yttrium iron garnets (YIGs), where yttrium is mainly diluted by bismuth to achieve higher rotations; the more bismuth, the stronger the rotation.

This material synthesis strategy is not straightforward to implement and it was first believed that more than two bismuth ions per formula unit of YIG was out of the question

due to the large ionic radius of bismuth. This causes the lattice parameter of Bi:YIG to increase with increasing bismuth content and form a non-thermodynamically stable configuration. What makes this strategy possible is the use of synthesis methods that do not require thermodynamic equilibrium as well as substrates with higher lattice parameters. High Faraday rotations ($20^{o}/\mu m$) and even completely bismuth-substituted iron garnets using these methods have been reported in the literature (Boudiara et al. 2004; Okuda et. al. 1990). However, the non-equilibrium nature of bismuth-substituted iron garnets engenders difficulties in scaling up its production to an industrial scale.

Bismuth-substituted garnet Faraday rotators are industrially manufactured by at least three firms; Garnetec Ltd. in Russia, GranOpt Co. Ltd. in Japan (GranOpt Co. Ltd. 2012) and Integrated Photonics Inc. in the United States (Integrated Photonics Inc. 2012). Rotators from all three firms are comparable in terms of design wavelengths (1300-1600nm), external field magnitudes (0-56kA/m) and isolation ratios (35dB). Models either requiring external bias fields or built-in magnetization are available and absorptive losses are on the order of 0.1dB.

Bulk Faraday rotators from Integrated Photonics Inc. were used in this work. Compared to orthoferrites (Didosyan & Barash 1995) such as that used in a free-space switch implementation in (Didosyan, Hauser & Reider 2002) (to be subsequently expounded), bismuth-substituted garnets exhibit negligible birefringence and a higher magneto-optic figure of merit. The rotators have a specific composition of $(Bi_{1.1}Tb_{1.9})(Fe_{4.25}Ga_{0.75})O_{12}$. Introducing terbium compensates for the large temperature dependence of the Faraday rotation contributed by bismuth, albeit at the expense of increasing the required thickness of the material to achieve a specific rotation since there is less bismuth present. Fratello (who is with Integrated Photonics Inc.) reports the $Bi_{1.1}Tb_{1.9}$

compromise that achieves a 20% temperature coefficient reduction of the Faraday rotation while maintaining a high magneto-optic figure of merit (Fratello, Licht & Brandle 1996; Fratello, Licht, Brandle & O'Connor 1997; Fratello, Licht & Brandle 1999). The rotators used in this work were grown by liquid phase epitaxy, which tends to produce higher quality material compared to RF-magnetron sputtering and pulsed laser deposition. They have a thickness of 470μm, absorptive loss of 0.1dB and provide 45^{o} of rotation at a saturation field of 21.33kA/m. The domain size of the rotators is measured via magnetic force microscopy (using a Digital Instruments Nanoscope III SPM) to be approximately 20μm as shown in Figure 20. A vibrating sample magnetometry measurement (using a Lakeshore Model 4500 VSM) produces the hysteresis curve in Figure 21 for the rotators.

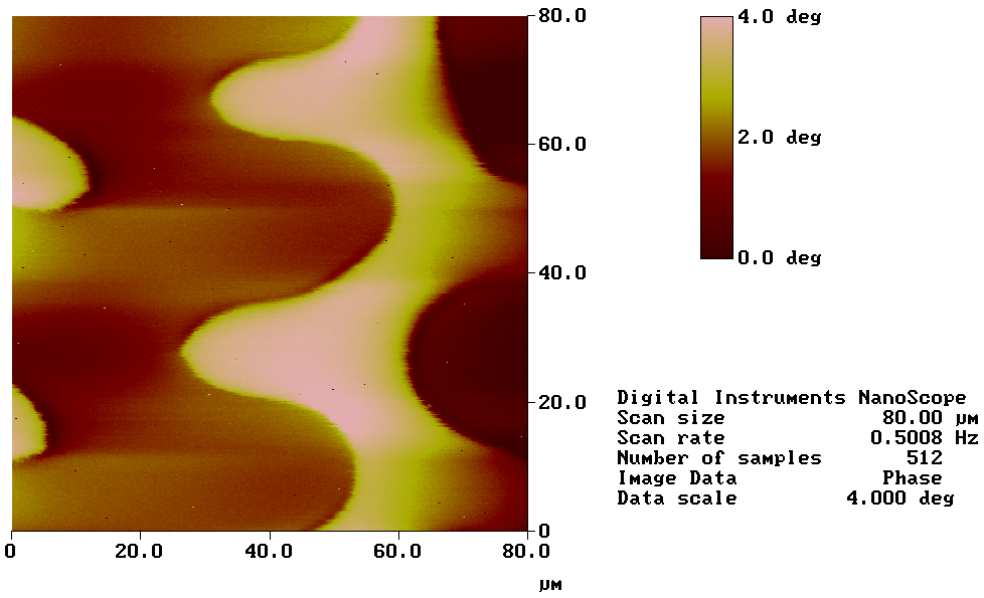

Figure 20 : Magnetic force microscope image of the bismuth-substituted iron garnet domain structure.

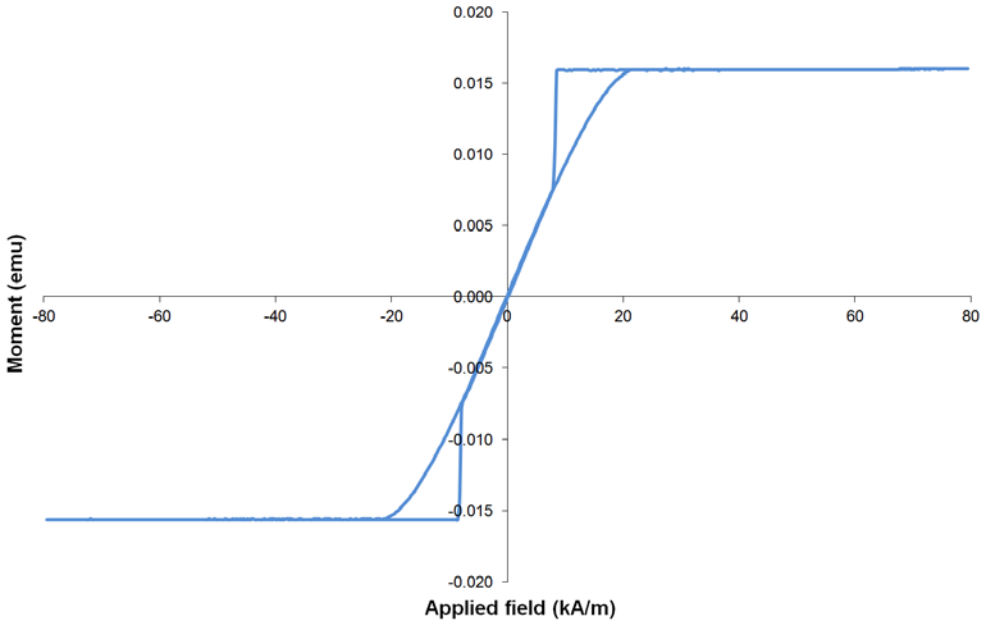

Figure 21 : Hysteresis curve of the bismuth-substituted iron garnet measured via vibrating sample magnetometry.

CHAPTER 3. MAGNETO-OPTIC SWITCHES

Although magneto-optic materials have been successfully utilized in optical devices such as isolators and circulators, their use in optical switches has not been widely investigated. A 2x2 magneto-optic switch for single-mode fibers was reported in (Didosyan, Hauser & Reider 2002) and is shown schematically in Figure 22. Yttrium iron garnet was utilized as a 45^o Faraday rotator at a saturation field of 7.96kA/m. The input light was split by a prism into two perpendicularly polarized components and these are rotated by the Faraday rotator and half-wave plate. Depending on the direction of magnetization the total rotation is either 0^o or 90^o and the output is taken either at 3 or 4. A switching time of 300μs was achieved.

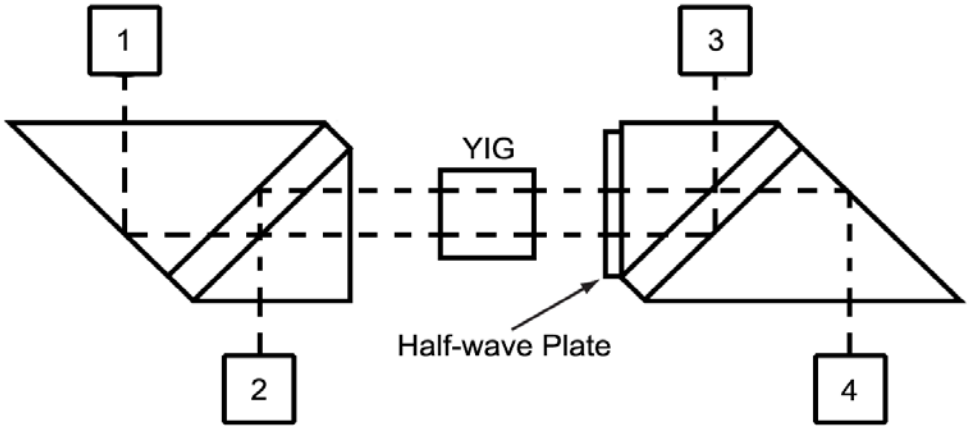

Figure 22 : Scheme of the 2x2 magneto-optic switch in (Didosyan, Hauser & Reider 2002).

More recently, a 1x2 magneto-optic switch based on the domain wall motion in orthoferrites was reported in (Shirasaki et al. 1984) and is shown schematically in Figure 23. It consists of a polarizer inserted such that its main plane forms an angle of 45^o with the vertical. The 1.2mm thick orthoferrite crystal is mounted behind the polarizer and this is

followed by a prism, which acts as a polarization beam splitter. A single domain state is maintained by the orthoferrite and it rotates the plane of polarization by ±45^{o}, contingent upon the sign of the domain magnetization. The polarization of the light incident on the prism is either horizontal or vertical depending on the sign of the driving magnetic field pulse and light is deflected to output 1 or 2 respectively. A switching time of 100ns was achieved.

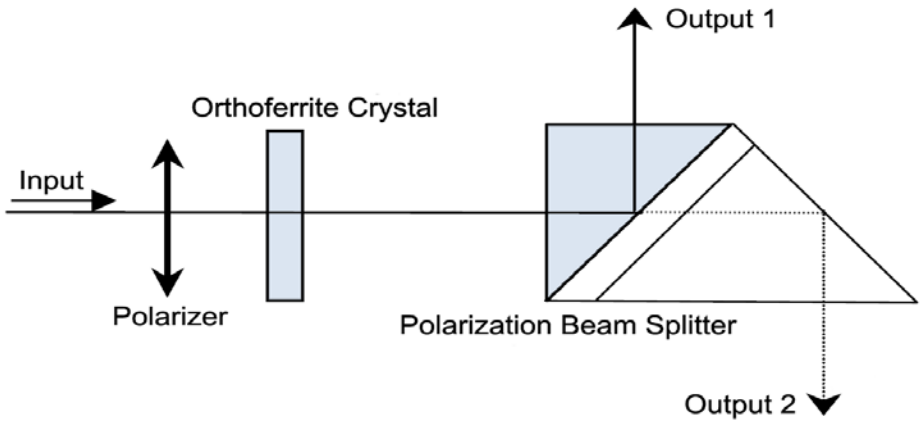

Figure 23 : Scheme of the 1x2 magneto-optic switch in (Shirasaki et al. 1984).

The switches reported above have some commonalities. They are both free-space in nature, drive their Faraday rotator elements at saturation and have a large beam diameter incident on the rotator material (300μm for the switch in (Shirasaki et al. 1984)). This imposes some important limitations for commercial network deployment. Free-space switches have a larger insertion loss as they require proper beam collimation and alignment of the free-space components. As fiber optic cables are the primary transmission medium for most commercial optical communications systems, the large beam size raises concerns since significant loss can result due to the large mode mismatch. Finally there is the issue of scalability since commercial networks often require large switch fabrics.

To address the limitations of the free-space switches, two magneto-optic switches were proposed. The Mach-Zehnder and Sagnac interferometer configurations were utilized

to convert the modulation of the relative phase between the orthogonal components of propagating light by Faraday rotators to an amplitude modulation. While adjustable and continuous levels of amplitude are desired for optical modulators, here an essentially binary amplitude (ON and OFF) is the objective. A good switch should maximize the difference between the two amplitude levels (extinction ratio) while toggling rapidly between them (switching speed).

3.1 Coupler

Couplers are a central component of interferometers and formed when two waveguides are brought into close proximity, transferring power from one to the other as illustrated in Figure 24.

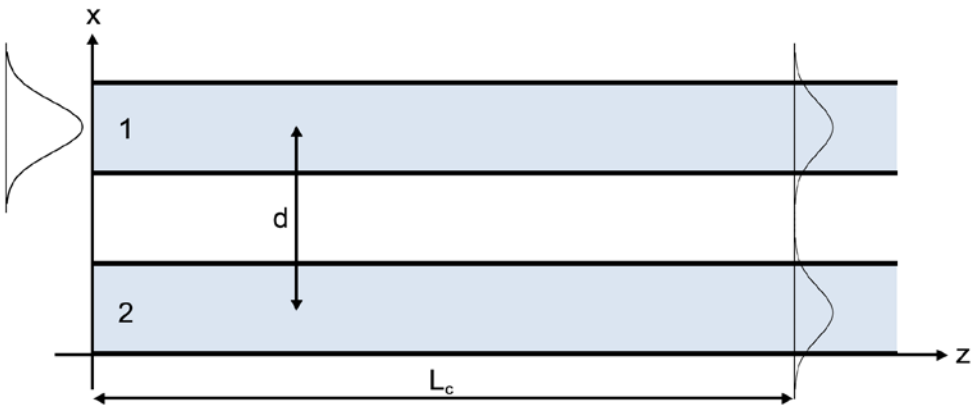

Figure 24 : Coupler consisting of two parallel waveguides.

The most rigorous method of analyzing these waveguides is solving for the anti-symmetric and symmetric modes of the coupled guides in a manner akin to solving for the modes of a single, isolated waveguide (Jackson 1998). However, this method can engender computational difficulties due to its reliance on the dissimilarity in propagation constants between the two modes, which decreases as a function of waveguide separation. Thus, this

method is fundamentally limited by machine precision. Moreover, all computations have to be repeated when changes are made to the waveguide separation, which hampers design space exploration. The precept of coupled mode theory is instead utilized to analyze coupler structures in this discourse. Its genesis can be traced back to the 1950s with several pioneering works (Gould 1955; Louisell 1954; Miller 1954; Pierce 1954) and it was later applied to optical waveguides in the 1970s (Kogelnik 1969; Marcuse 1971; Snyder 1972; Yariv 1973; Yariv & Taylor 1981).

The propagation of waves along an arbitrary waveguide can be described by $e^{-(\alpha+j\beta)z}$. The assumption of a lossless waveguide is made (ie. $\alpha = 0$), which is justified for the case of relatively low-loss waveguides and short coupling section lengths. Suppose there is a function $W(z)$ representing the wave propagation and amplitude that is a product of some amplitude constant, $e^{-j\beta z}$ as well as the transverse field distribution. The first-order differential of such a function can be expressed as :

$$\frac{dW}{dz} + j\beta W = 0 \tag{3.1}$$

Without any loss of generality, the amplitude constant and transverse field distribution are set such that the power in the waveguide is $|W(z)|^2$. For the case of the two parallel waveguides as depicted in Figure 24, the first-order differentials governing the two modes is given by :

$$\left.\frac{dW_1}{dz} + j\beta_1 W_1 = 0\right|_{d=\infty} \tag{3.2}$$

$$\left.\frac{dW_2}{dz} + j\beta_2 W_2 = 0\right|_{d=\infty} \tag{3.3}$$

As the waveguides approach each other, the propagation of waves in one is perturbed by the presence of the other and vice versa. A coupling constant κ is introduced to account for this interaction, which forms the coupled mode equations.

$$\frac{dW_1}{dz} + j\beta_1 W_1 = j\kappa W_2 \tag{3.4}$$

$$\frac{dW_2}{dz} + j\beta_2 W_2 = j\kappa W_1 \tag{3.5}$$

Solving for W_1 and W_2 using this set of equations is somewhat involved due to the two unknowns. The process is expedited by computing a second-order differential with a single unknown. Since β_1 and β_2 are independent of z (and likewise κ for the case of parallel waveguides), only W_1 and W_2 are differentiated.

$$\frac{d^2W_1}{dz^2} + j(\beta_1 + \beta_2)\frac{dW_1}{dz} + (\kappa^2 - \beta_1\beta_2)W_1 = 0 \tag{3.6}$$

$$\frac{d^2W_2}{dz^2} + j(\beta_1 + \beta_2)\frac{dW_2}{dz} + (\kappa^2 - \beta_1\beta_2)W_2 = 0 \tag{3.7}$$

The solution for this set of second-order differentials can be expressed as :

$$W_1(z) = \left[W_1(0)\left(\cos(\gamma z) - j\left(\frac{\Delta\beta}{2\gamma}\right)\sin(\gamma z)\right) + W_2(0)\left(j\left(\frac{\kappa}{\gamma}\right)\sin(\gamma z)\right)\right] e^{-j\left(\frac{\beta_1+\beta_2}{2}\right)z} \tag{3.8}$$

$$W_2(z) = \left[W_2(0)\left(\cos(\gamma z) + j\left(\frac{\Delta\beta}{2\gamma}\right)\sin(\gamma z)\right) + W_1(0)\left(j\left(\frac{\kappa}{\gamma}\right)\sin(\gamma z)\right)\right] e^{-j\left(\frac{\beta_1+\beta_2}{2}\right)z} \tag{3.9}$$

where $\Delta\beta$ and γ are defined as :

$$\Delta\beta = \beta_1 - \beta_2 \tag{3.10}$$

$$\gamma = \sqrt{\kappa^2 + \left(\Delta\beta/2\right)^2} \tag{3.11}$$

Assuming the boundary conditions of $W_1(0) = 1$ and $W_2(0) = 0$, Equations 3.8 and 3.9 reduce to :

$$W_1(z) = \left[\cos(\gamma z) - j\left(\frac{\Delta\beta}{2\gamma}\right)\sin(\gamma z)\right] e^{-j\left(\frac{\beta_1+\beta_2}{2}\right)z} \tag{3.12}$$

$$W_2(z) = \left[j\left(\frac{\kappa}{\gamma}\right)\sin(\gamma z)\right] e^{-j\left(\frac{\beta_1+\beta_2}{2}\right)z} \tag{3.13}$$

Thus the power in each waveguide is :

$$P_1(z) = |W_1(z)|^2 = 1 - \left(\frac{\kappa^2}{\gamma^2}\right)\sin^2(\gamma z) \tag{3.14}$$

$$P_2(z) = |W_2(z)|^2 = \left(\frac{\kappa^2}{\gamma^2}\right)\sin^2(\gamma z) \tag{3.15}$$

For the interferometer configurations of interest, an equal power splitting ratio is desired. Furthermore, the capability of complete power transfer into one waveguide or the other is desired to maximize the extinction ratio of the switches that use these interferometer configurations. This second criteria is met by satisfying the phase match condition, ie. using two waveguides with identical propagation constants ($\Delta\beta = 0$). The coupling constant in this case can be computed as :

$$\kappa = \frac{k}{4P}\sqrt{\frac{\varepsilon_0}{\mu_0}}\left(n_{core}^2 - n_{clad}^2\right)\iint E_1 . E_2^* \, dA \tag{3.16}$$

where the integration is performed over the core region of waveguide 1. Equations 3.14 and 3.15 are simplified to the following expressions, which are plotted in Figure 25.

$$P_1(z) = \left|W_1(z)\right|^2 = \cos^2(\kappa z) \tag{3.17}$$

$$P_2(z) = \left|W_2(z)\right|^2 = \sin^2(\kappa z) \tag{3.18}$$

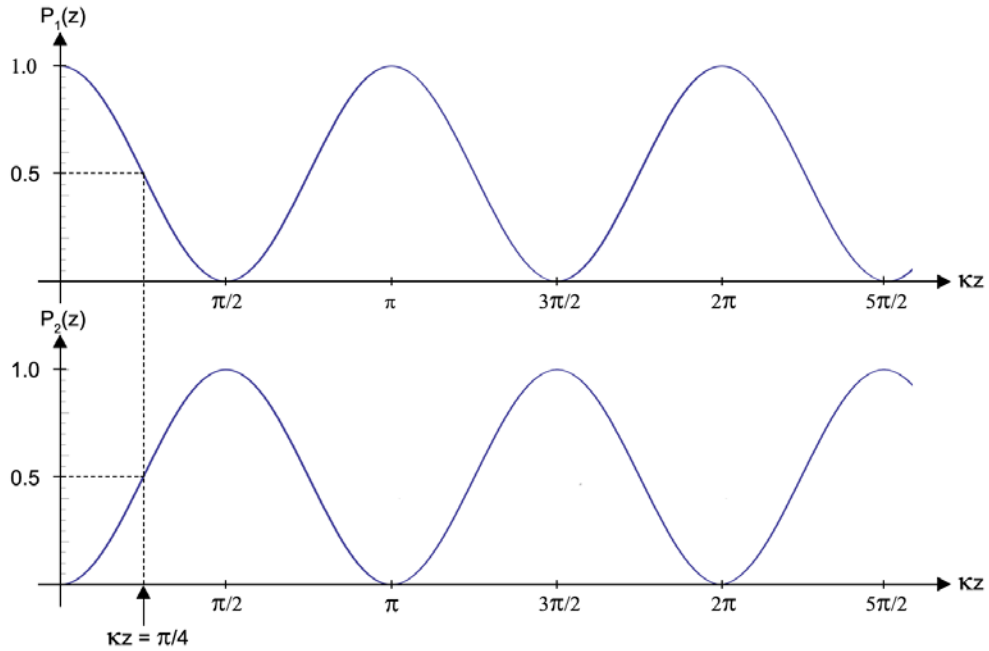

Figure 25 : Power in each waveguide as a function of distance. All power is launched into waveguide 1 at z = 0.

It is clear from Figure 25 that the first coupler criteria is satisfied if the interaction length of the coupler (L_c) and coupling strength (κ) are chosen such that their product is an odd multiple of $\pi/4$. In practice, κL_c is chosen to be $\pi/4$ to minimize device dimensions.

The solutions above are commonly expressed in the form of transfer matrices (Kurokawa 1965). In principle, scattering matrices (Matthews 1955) could also be utilized. However, they cannot be cascaded to analyze complex structures consisting of multiple subsections as they relate the light emerging from a structure to the light impinging on it. Transfer matrices do not suffer from this limitation since they describe the mode amplitudes at z > 0 in terms of the mode amplitudes at z = 0.

The standard convention calls for a 2x2 transfer matrix, which only captures forward-propagating mode amplitudes. However it must be recognized that if a directional coupler is operated in the reverse direction, it also provides coupling between the two backward-travelling modes and a more complete solution is the 4x4 transfer matrix. This expansion of the standard transfer matrix is necessary if one desires to account for both transmission and reflection, eg. to model unintentional waveguide imperfections due to fabrication errors or in the case of Bragg gratings, intentional and periodic waveguide geometry perturbations.

The complete transfer matrix of a symmetric directional coupler is given by :

$$T_c = \begin{bmatrix} G & 0 \\ 0 & G^* \end{bmatrix} \tag{3.19}$$

where the submatrix G is a simple 2x2 matrix described by :

$$G = \begin{bmatrix} \cos(\kappa L_c) & j\sin(\kappa L_c) \\ j\sin(\kappa L_c) & \cos(\kappa L_c) \end{bmatrix} \tag{3.20}$$

κ is the coupling constant and L_c is the interaction length of this coupling action for the structure. Since κL_c is $\pi/4$ for the 3dB couplers considered here, the submatrix G becomes :

$$G = \frac{1}{\sqrt{2}} \begin{bmatrix} 1 & j \\ j & 1 \end{bmatrix} \tag{3.21}$$

3.2 Mach-Zehnder Interferometer

A Mach-Zehnder interferometer (Mach 1892; Zehnder 1891) is a 2x2 device consisting of three stages as shown in Figure 26; an input section in which a 3dB coupler splits the input signal, a central section where one of the waveguides is longer by ΔL to

induce a phase shift $\Delta\theta$ between the two interferometer arms and an output section where a second 3dB coupler recombines the signals.

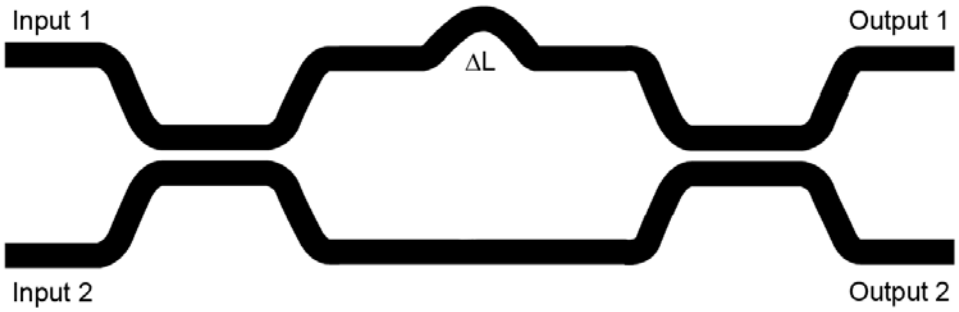

Figure 26 : Structure of a Mach-Zehnder interferometer.

The phase difference between the two interferometer arms due to the path difference ΔL can be expressed as :

$$\Delta\theta = \frac{2\pi n_1}{\lambda}(L + \Delta L) - \frac{2\pi n_2}{\lambda}L \tag{3.22}$$

where n_1 and n_2 are the effective refractive indices for the two interferometer arms. From Equation 3.22, it is seen that a phase shift can be induced by either lengthening one of the interferometer arms or changing the effective refractive indices of one of the arms.

For the designs considered in this work, the phase shift is induced via Faraday rotation and it is chosen to be equated to a physical path length difference. Therefore a common effective refractive index is assumed and Equation 3.22 simplifies to :

$$\Delta\theta = \frac{2\pi n_{eff}}{\lambda}\Delta L = \beta\Delta L \tag{3.23}$$

where β is the propagation constant in a waveguide. This phase imbalance can be modeled with the following transfer matrix :

$$T_{\Delta\theta} = \begin{bmatrix} M & 0 \\ 0 & M^* \end{bmatrix} \tag{3.24}$$

where the submatrix M is a simple 2x2 matrix described by :

$$M = \begin{bmatrix} e^{j(\Delta\theta/2)} & 0 \\ 0 & e^{-j(\Delta\theta/2)} \end{bmatrix} \tag{3.25}$$

The transfer matrix for the Mach-Zehnder interferometer is now the product of the three transfer matrices representing the input 3dB coupler, imbalanced interferometer arms and output 3dB coupler :

$$T_{MZI} = T_c T_{\Delta\theta} T_c = \begin{bmatrix} G & 0 \\ 0 & G^* \end{bmatrix} \begin{bmatrix} M & 0 \\ 0 & M^* \end{bmatrix} \begin{bmatrix} G & 0 \\ 0 & G^* \end{bmatrix} \tag{3.26}$$

which simplifies to :

$$T_{MZI} = \begin{bmatrix} (GMG) & 0 \\ 0 & (GMG)^* \end{bmatrix} = j \begin{bmatrix} \sin(\Delta\theta/2) & \cos(\Delta\theta/2) & 0 & 0 \\ \cos(\Delta\theta/2) & -\sin(\Delta\theta/2) & 0 & 0 \\ 0 & 0 & -\sin(\Delta\theta/2) & \cos(\Delta\theta/2) \\ 0 & 0 & \cos(\Delta\theta/2) & \sin(\Delta\theta/2) \end{bmatrix} \tag{3.27}$$

Thus the input fields E_{in1} and E_{in2} at inputs 1 and 2 respectively are transformed by the Mach-Zehnder interferometer into output fields E_{out1} and E_{out2} at outputs 1 and 2 respectively as :

$$\begin{bmatrix} E_{out1}^{+} \\ E_{out2}^{+} \\ E_{out1}^{-} \\ E_{out2}^{-} \end{bmatrix} = j \begin{bmatrix} \sin(\Delta\theta/2) & \cos(\Delta\theta/2) & 0 & 0 \\ \cos(\Delta\theta/2) & -\sin(\Delta\theta/2) & 0 & 0 \\ 0 & 0 & -\sin(\Delta\theta/2) & \cos(\Delta\theta/2) \\ 0 & 0 & \cos(\Delta\theta/2) & \sin(\Delta\theta/2) \end{bmatrix} \begin{bmatrix} E_{in1}^{+} \\ E_{in2}^{+} \\ E_{in1}^{-} \\ E_{in2}^{-} \end{bmatrix} \quad (3.28)$$

where + and – denote the forward and backward-travelling modes respectively. For an ideal device, there is no interaction between these modes. Looking only in the forward direction, the optical power at the Mach-Zehnder interferometer outputs can be expressed as :

$$P_{out1} = E_{out1}E_{out1}^{*} = P_{in1}\sin^2(\Delta\theta/2) + P_{in2}\cos^2(\Delta\theta/2) \quad (3.29)$$

$$P_{out2} = E_{out2}E_{out2}^{*} = P_{in1}\cos^2(\Delta\theta/2) + P_{in2}\sin^2(\Delta\theta/2) \quad (3.30)$$

Thus for phase matched Mach-Zehnder interferometer arms ($\Delta\theta = 0^{o}$), $P_{out1} = P_{in2}$ and $P_{out2} = P_{in1}$. For arms mismatched by an integral number of half-wavelengths ($\Delta\theta = n180^{o}$), $P_{out1} = P_{in1}$ and $P_{out2} = P_{in2}$.

3.3 Sagnac Interferometer

A Sagnac interferometer (Sagnac 1913a; Sagnac 1913b) is a device consisting of two stages as shown in Figure 27; a closed loop and an input/output section in which a 3dB coupler splits the input signal and recombines the signal components that traverse the closed loop.

The operation of the Sagnac interferometer can be understood by unfolding it as illustrated in Figure 28, where + and – denote the forward and backward-travelling modes respectively.

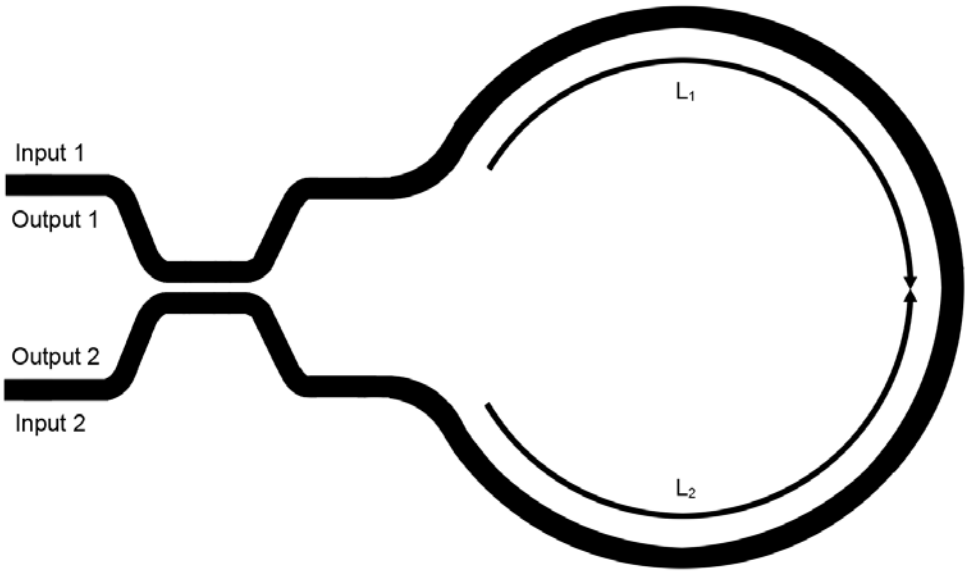

Figure 27 : Structure of a Sagnac interferometer.

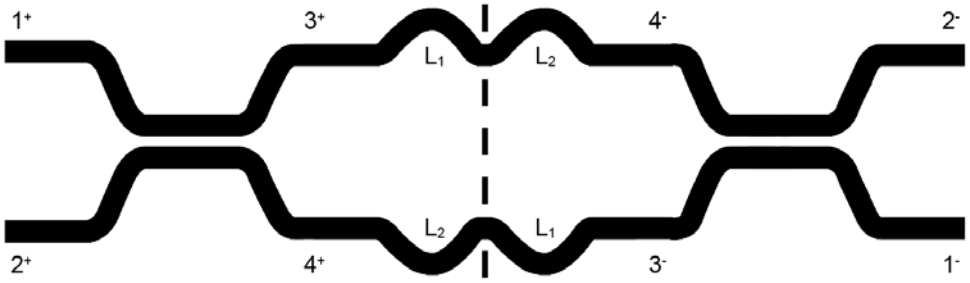

Figure 28 : Unfolded Sagnac interferometer.

Recall that the propagation of waves along an arbitrary lossless waveguide is described by $e^{-j\beta z}$. The transfer matrix for the Sagnac interferometer is now the product of the various transfer matrices representing the propagation through the input 3dB coupler, loop and output 3dB coupler :

$$T_{Sagnac} = [G][F_1][F_2][G]$$
$$= \frac{1}{\sqrt{2}}\begin{bmatrix} 1 & j \\ j & 1 \end{bmatrix}\begin{bmatrix} e^{-j\beta L_1} & 0 \\ 0 & e^{-j\beta L_2} \end{bmatrix}\begin{bmatrix} e^{-j\beta L_2} & 0 \\ 0 & e^{-j\beta L_1} \end{bmatrix}\frac{1}{\sqrt{2}}\begin{bmatrix} 1 & j \\ j & 1 \end{bmatrix} \quad (3.31)$$

which simplifies to :

$$T_{Sagnac} = j\begin{bmatrix} 0 & e^{-j\beta(L_1+L_2)} \\ e^{-j\beta(L_1+L_2)} & 0 \end{bmatrix} \tag{3.32}$$

The input fields E_{in1} and E_{in2} at inputs 1 and 2 respectively are transformed by the Sagnac interferometer into output fields E_{out1} and E_{out2} at outputs 1 and 2 respectively as :

$$\begin{bmatrix} E^+_{out1} \\ E^+_{out2} \end{bmatrix} = \begin{bmatrix} E^-_{in2} \\ E^-_{in1} \end{bmatrix} = j\begin{bmatrix} 0 & e^{-j\beta(L_1+L_2)} \\ e^{-j\beta(L_1+L_2)} & 0 \end{bmatrix}\begin{bmatrix} E^+_{in1} \\ E^+_{in2} \end{bmatrix} \tag{3.33}$$

The input signals are returned to their original ports with a $\pi/2$ phase shift imparted by the coupler as well as a $\beta(L_1 + L_2)$ phase shift imparted by the loop, which is the reason the Sagnac interferometer is also termed a loop mirror.

When a non-reciprocal element is introduced into the loop, an additional submatrix T_{NR} has to be inserted into Equation 3.31 to account for the dissimilar transmissivities experienced by the counter-propagating waves.

$$\begin{aligned} T_{Sagnac} &= [G][F_1][T_{NR}][F_2][G] \\ &= \frac{1}{\sqrt{2}}\begin{bmatrix} 1 & j \\ j & 1 \end{bmatrix}\begin{bmatrix} e^{-j\beta L_1} & 0 \\ 0 & e^{-j\beta L_2} \end{bmatrix}\begin{bmatrix} T_{CW} & 0 \\ 0 & T_{CCW} \end{bmatrix}\begin{bmatrix} e^{-j\beta L_2} & 0 \\ 0 & e^{-j\beta L_1} \end{bmatrix}\frac{1}{\sqrt{2}}\begin{bmatrix} 1 & j \\ j & 1 \end{bmatrix} \end{aligned} \tag{3.34}$$

For the designs considered in this work, a Faraday rotator is utilized as the non-reciprocal element, which induces a phase shift between the counter-propagating waves as in the Mach-Zehnder interferometer configuration. Conceptually, this can be represented by replacing T_{NR} with the submatrix M from Equation 3.25, which results in the expression :

$$T_{Sagnac} = \frac{1}{2}\begin{bmatrix} A & B \\ B & -A \end{bmatrix} \tag{3.35}$$

where A and B are defined as :

$$A = e^{j\left(\frac{\Delta\theta}{2} - \beta(L_1+L_2)\right)} - e^{-j\left(\frac{\Delta\theta}{2} + \beta(L_1+L_2)\right)} \tag{3.36}$$

$$B = je^{j\left(\frac{\Delta\theta}{2} - \beta(L_1+L_2)\right)} + e^{-j\left(\frac{\Delta\theta}{2} + \beta(L_1+L_2)\right)} \tag{3.37}$$

3.4 Mach-Zehnder Magneto-optic Switch

The proposed Mach-Zehnder magneto-optic switch is shown schematically in Figure 29. It utilizes two Faraday rotators to both affect a 180^o of phase mismatch between the two interferometer arms as well as equalize the amplitudes in the two arms to a first order. For light exiting the first 3dB coupler and impinging normally on the Faraday rotator, its polarization is decomposed into left and right circularly polarized states by use of the conversion operator :

$$C = \frac{1}{2}\begin{bmatrix} 1 & j \\ 1 & -j \end{bmatrix} \tag{3.38}$$

The left and right circularly polarized states are the propagation eigenmodes in the Faraday rotator, each with different effective refractive indices (eigenvalues). Thus the two components propagate with different velocities in the material and this is captured by the propagation operator :

$$D = e^{-j\varphi}\begin{bmatrix} e^{j\theta_F(t)} & 0 \\ 0 & e^{-j\theta_F(t)} \end{bmatrix} \tag{3.39}$$

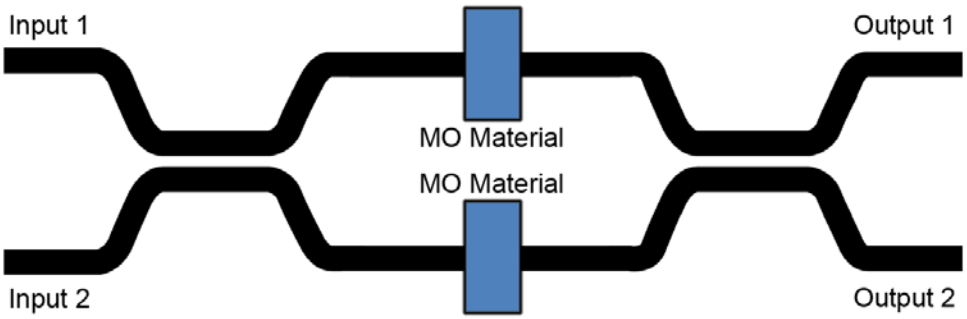

Figure 29 : Structure of the proposed magneto-optic switch based on the Mach-Zehnder interferometer configuration.

where the Faraday rotation (θ_F) is as defined in Equation 2.8 (restated here for convenience) and the common phase φ is defined as :

$$\theta_F = \mathrm{Re}\left(\frac{\pi t(n_+ - n_-)}{\lambda}\right) = \mathrm{Re}\left(\frac{\pi t \varepsilon_{xy}}{\lambda\sqrt{\varepsilon_{xx}}}\right) \tag{3.40}$$

$$\varphi = \mathrm{Re}\left(\frac{\pi t(n_+ + n_-)}{\lambda}\right) \tag{3.41}$$

Finally the two light components are recombined by use of the inverse conversion operator C^{-1}. These operations can be combined to be expressed as a Jones transfer matrix for the Faraday rotator :

$$J_{FR} = C^{-1}DC = \begin{bmatrix} \cos(\theta_F) & -\sin(\theta_F) \\ \sin(\theta_F) & \cos(\theta_F) \end{bmatrix} \tag{3.42}$$

The polarization of the light exiting the Faraday rotator is thus rotated by $-\theta_F$ with respect to that of the impinging light. Implicit in the formulation of Equation 3.42 is that the Faraday rotator is sufficiently transparent to be approximated as being lossless and hence not incur any ellipticity.

Considering only the forward-travelling modes, the outputs of the first 3dB coupler can be expressed as follows using the forward transfer submatrix G from Equation 3.21 :

$$E'_{in1} = \frac{1}{\sqrt{2}}\left(E_{in1} + jE_{in2}\right) \tag{3.43}$$

$$E'_{in2} = \frac{1}{\sqrt{2}}\left(E_{in2} + jE_{in1}\right) \tag{3.44}$$

Linearly polarized light at the switch input can be expressed as follows (restated here from Equation 2.1 with $\phi = 0^o$ for convenience) :

$$\vec{E} = \vec{a}_x E_{0x} \cos(\omega t - \beta z) + \vec{a}_y E_{0y} \cos(\omega t - \beta z) \tag{3.45}$$

The first 3dB coupler inputs are taken as the reference point (z = 0). The light at input 1 can be assumed to be horizontally polarized ($E_{0y} = 0$) and incident at t = 0 without loss of generality. Additionally, since the structure is intended to be operated as a 1x1 switch, it is assumed that input 2 is not excited ($E_{in2} = 0$). With these conditions, the outputs of the first 3dB coupler can be written as :

$$E'_{in1} = \vec{a}_x \frac{E_{0x}}{\sqrt{2}} \tag{3.46}$$

$$E'_{in2} = \vec{a}_x j \frac{E_{0x}}{\sqrt{2}} \tag{3.47}$$

The light exiting the Faraday rotator in interferometer arm 1 can be determined using the Jones transfer matrix from Equation 3.42. A similar derivation can be performed for arm 2 as well.

$$\begin{bmatrix} E''_{in1-x} \\ E''_{in1-y} \end{bmatrix} = \begin{bmatrix} \cos(\theta_{F1}) & -\sin(\theta_{F1}) \\ \sin(\theta_{F1}) & \cos(\theta_{F1}) \end{bmatrix} \begin{bmatrix} E'_{in1-x} \\ E'_{in1-y} \end{bmatrix} \tag{3.48}$$

$$E''_{in1} = \vec{a}_x \frac{E_{0x}}{\sqrt{2}} \cos(\theta_{F1}) + \vec{a}_y \frac{E_{0x}}{\sqrt{2}} \sin(\theta_{F1}) \tag{3.49}$$

$$E''_{in2} = \vec{a}_x \left(-\frac{E_{0x}}{\sqrt{2}} \right) \sin(\theta_{F2}) + \vec{a}_y \frac{E_{0x}}{\sqrt{2}} \cos(\theta_{F2}) \tag{3.50}$$

where θ_{F1} and θ_{F2} are the Faraday rotation angles of the rotators in interferometer arms 1 and 2 respectively.

Finally, using the forward transfer submatrix for the second 3dB coupler gives the actual switch outputs :

$$E_{out1} = \vec{a}_x \left[\frac{E_{0x}}{2} \left(\cos(\theta_{F1}) - \cos(\theta_{F2}) \right) \right] + \vec{a}_y \left[\frac{E_{0x}}{2} \left(\sin(\theta_{F1}) - \sin(\theta_{F2}) \right) \right] \tag{3.51}$$

$$E_{out2} = \vec{a}_x \left[j \frac{E_{0x}}{2} \left(\cos(\theta_{F1}) + \cos(\theta_{F2}) \right) \right] + \vec{a}_y \left[j \frac{E_{0x}}{2} \left(\sin(\theta_{F1}) + \sin(\theta_{F2}) \right) \right] \tag{3.52}$$

The outputs fields and power for different Faraday rotations are tabulated below :

Table 3 : Mach-Zehnder magneto-optic switch states.

	ON		**OFF**	
	θ_{F1}	**θ_{F2}**	**θ_{F1}**	**θ_{F2}**
	0°	0°	90°	–90°
E_{out1}	0		**a_y** E_{0x}	
E_{out2}	**a_x** jE_{0x}		0	
P_{out1}	0		E_{0x}^2	
P_{out2}	E_{0x}^2		0	

Input 1 and output 2 are chosen as the functional switch ports since the polarization of the input light is maintained, albeit with a 90^o phase shift as denoted above. The designated ON and OFF states correspond to this choice of ports. It can be clearly seen that the proposed switch operates in a fashion similar to the Mach-Zehnder interferometer examined earlier.

3.5 Sagnac Magneto-optic Switch

The proposed Sagnac magneto-optic switch is shown schematically in Figure 30. It utilizes a Faraday rotator placed in the middle of the Sagnac loop to affect a 180^o of phase mismatch between the two counter-propagating waves.

The light exiting the 3dB coupler and impinging normally on the Faraday rotator can again be decomposed into left and right circularly polarized states by use of the conversion operator in Equation 3.38. They propagate with dissimilar velocities in the magneto-optic material (as in Equation 3.39) and are finally recombined as expressed by the inverse conversion operator, with the repeated assumption that the Faraday rotator is sufficiently lossless to avoid incurring any ellipticity.

A critical difference between the two proposed switches is that there is common direction of propagation in the Mach-Zehnder configuration whereas there are two directions of propagation in the Sagnac configuration. The clockwise direction (ie. port S_1 to S_2) is taken to be positive while the counter-clockwise direction (ie. port S_2 to S_1) is taken negative. Bearing this in mind, the Jones transfer matrices for the Faraday rotator is expressed as :

$$J_{FR-CW} = \begin{bmatrix} \cos(\theta_F) & -\sin(\theta_F) \\ \sin(\theta_F) & \cos(\theta_F) \end{bmatrix} \tag{3.53}$$

$$J_{FR-CCW} = \begin{bmatrix} \cos(\theta_F) & \sin(\theta_F) \\ -\sin(\theta_F) & \cos(\theta_F) \end{bmatrix} \tag{3.54}$$

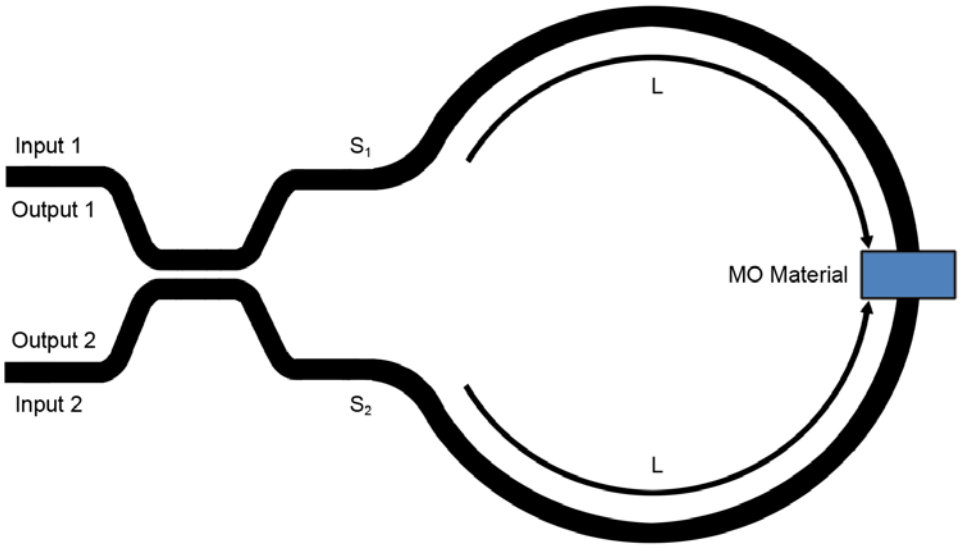

Figure 30 : Structure of the proposed magneto-optic switch based on the Sagnac interferometer configuration.

The Sagnac switch is unfolded for analysis purposes and is illustrated in Figure 31, where + and – denote forward and backward-travelling modes respectively.

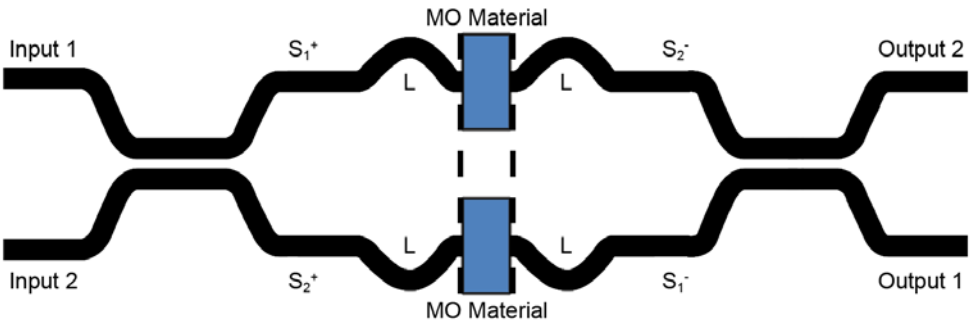

Figure 31 : Unfolded Sagnac magneto-optic switch.

Considering the forward-travelling modes, the outputs of the first 3dB coupler after traversing half of the Sagnac loop can be expressed as follows using the forward transfer submatrix G from Equation 3.21 :

$$E_{S_1}^{'} = \frac{e^{-j\beta L}}{\sqrt{2}}\left(E_{in1} + jE_{in2}\right) \tag{3.55}$$

$$E_{S_2}^{'} = \frac{e^{-j\beta L}}{\sqrt{2}}\left(E_{in2} + jE_{in1}\right) \tag{3.56}$$

The 3dB coupler inputs are taken as the reference point (z = 0). The light at input 1 can be assumed to be horizontally polarized (E_{0y} = 0) and incident at t = 0 without loss of generality. Additionally, since the structure is intended to be operated as a 1x1 switch, it is assumed that input 2 is not excited (E_{in2} = 0). With these conditions, the light impinging on the Faraday rotator can be written as :

$$E_{S_1}^{'} = e^{-j\beta L}.\vec{a}_x \frac{E_{0x}}{\sqrt{2}} \tag{3.57}$$

$$E_{S_2}^{'} = e^{-j\beta L}.\vec{a}_x j\frac{E_{0x}}{\sqrt{2}} \tag{3.58}$$

The light exiting the Faraday rotator in both the clockwise and counter-clockwise directions can be determined using the Jones transfer matrices from Equations 3.53 and 3.54.

$$\begin{bmatrix} E_{S_1-x}^{''} \\ E_{S_1-y}^{''} \end{bmatrix} = \begin{bmatrix} \cos(\theta_F) & -\sin(\theta_F) \\ \sin(\theta_F) & \cos(\theta_F) \end{bmatrix} \begin{bmatrix} E_{S_1-x}^{'} \\ E_{S_1-y}^{'} \end{bmatrix} \tag{3.59}$$

$$\begin{bmatrix} E_{S_2-x}^{''} \\ E_{S_2-y}^{''} \end{bmatrix} = \begin{bmatrix} \cos(\theta_F) & \sin(\theta_F) \\ -\sin(\theta_F) & \cos(\theta_F) \end{bmatrix} \begin{bmatrix} E_{S_2-x}^{'} \\ E_{S_2-y}^{'} \end{bmatrix} \tag{3.60}$$

$$E''_{S_1} = e^{-j\beta L}.\vec{a}_x \frac{E_{0x}}{\sqrt{2}}\cos(\theta_F) + e^{-j\beta L}.\vec{a}_y \frac{E_{0x}}{\sqrt{2}}\sin(\theta_F) \quad (3.61)$$

$$E''_{S_2} = je^{-j\beta L}.\vec{a}_x \frac{E_{0x}}{\sqrt{2}}\cos(\theta_F) - je^{-j\beta L}.\vec{a}_y \frac{E_{0x}}{\sqrt{2}}\sin(\theta_F) \quad (3.62)$$

Finally, using the forward transfer submatrix for the 3dB coupler gives the actual switch outputs :

$$E_{out1} = \vec{a}_x\left[je^{-j\beta 2L}E_{0x}\cos(\theta_F)\right] \quad (3.63)$$

$$E_{out2} = \vec{a}_y\left[e^{-j\beta 2L}E_{0x}\sin(\theta_F)\right] \quad (3.64)$$

The outputs fields and power for different Faraday rotations are tabulated below :

Table 4 : Sagnac magneto-optic switch states.

	ON	**OFF**
	θ_F	
	0°	90°
E_{out1}	$\mathbf{a_x}\, je^{-j\beta 2L}E_{0x}$	0
E_{out2}	0	$\mathbf{a_y}\, e^{-j\beta 2L}E_{0x}$
P_{out1}	E_{0x}^2	0
P_{out2}	0	E_{0x}^2

Input 1 and output 1 are chosen as the functional switch ports since the polarization of the input light is maintained, albeit with a phase shift from traversing the loop as denoted above. The designated ON and OFF states correspond to this choice of ports. It can be clearly seen that the proposed switch operates in a fashion similar to the Sagnac interferometer.

CHAPTER 4. SWITCH PERFORMANCE

4.1 Mach-Zehnder Magneto-optic Switch

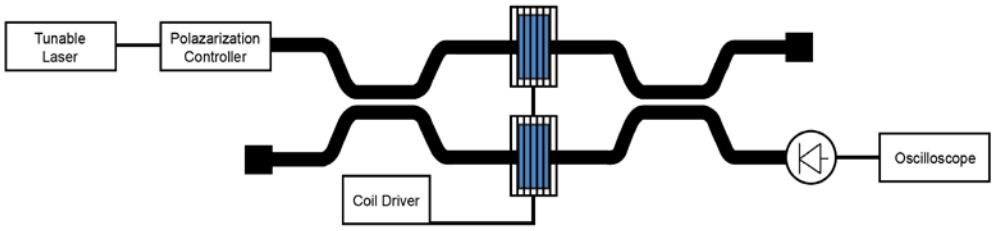

Figure 32 : Laboratory setup for characterizing the Mach-Zehnder magneto-optic switch.

The laboratory setup for the experimental evaluation of the fiber-based implementation of the proposed Mach-Zehnder magneto-optic switch is shown in Figure 32. A 1550nm laser in an Agilent 8164A Lightwave system was linearly polarized via an Agilent 8169A polarization controller and used as the switch input signal. Since this was a proof-of-concept prototype, the Faraday rotator in the second interferometer arm was kept inactive and a General Photonics FPS-001-01 fiber phase shifter was utilized to exert better control on the phase imbalance. The Faraday rotator in the first arm was actuated with the H-bridge circuit shown in Figure 33. It utilizes four Motorola MC33886s in parallel and is capable of controlling load currents of up to 20A at a modulation rate of 10kHz. The output optical power was sensed using a Thorlabs DET410C photodetector in tandem with a transimpedance amplifier built around a Burr-Brown OPA128 operational amplifier (shown in Figure 34).

A switching field of 15.91kA/m was required and an extinction ratio of approximately 10.5dB was achieved as shown in Figure 35. The rise and fall times measured for the current driving the Faraday rotator was measured to be 1.9μs as shown in Figure 36.

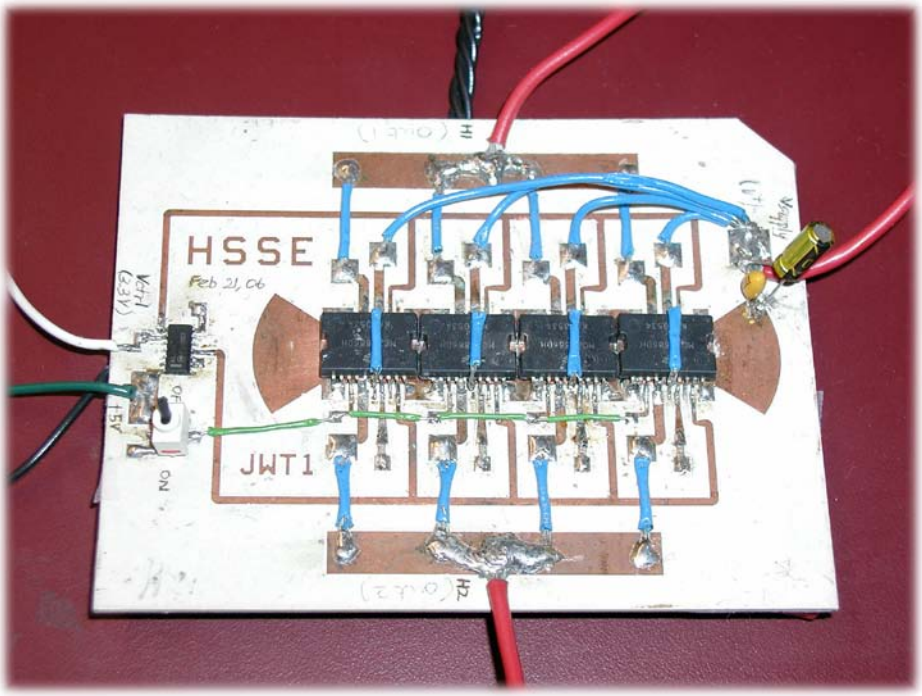

Figure 33 : H-bridge bi-directional Faraday rotator actuation circuit.

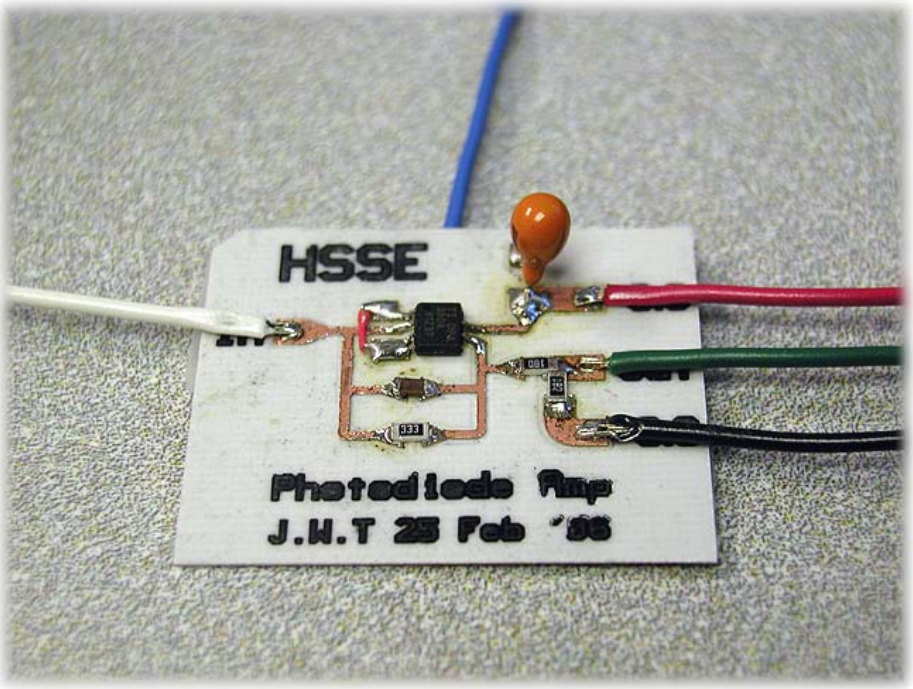

Figure 34 : Transimpedance amplifier circuit to convert the photodiode current to a measurable voltage.

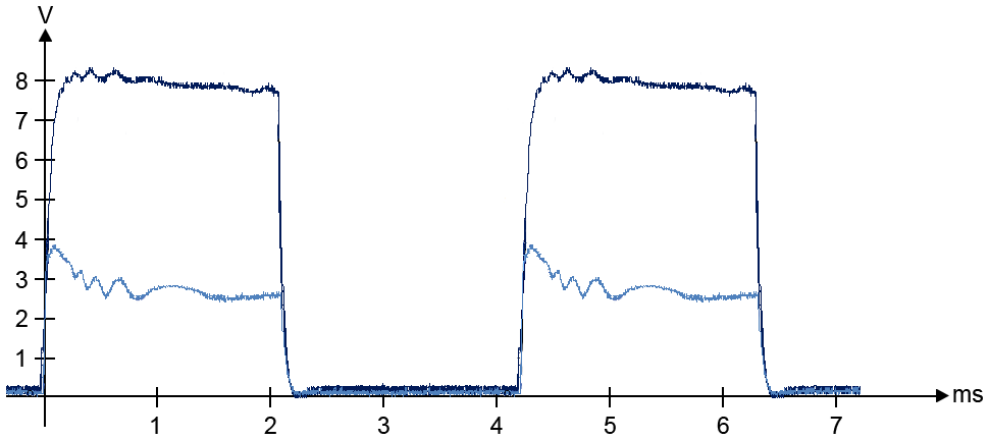

Figure 35 : Single-mode fiber Mach-Zehnder magneto-optic switch extinction ratio and switching field measurements.

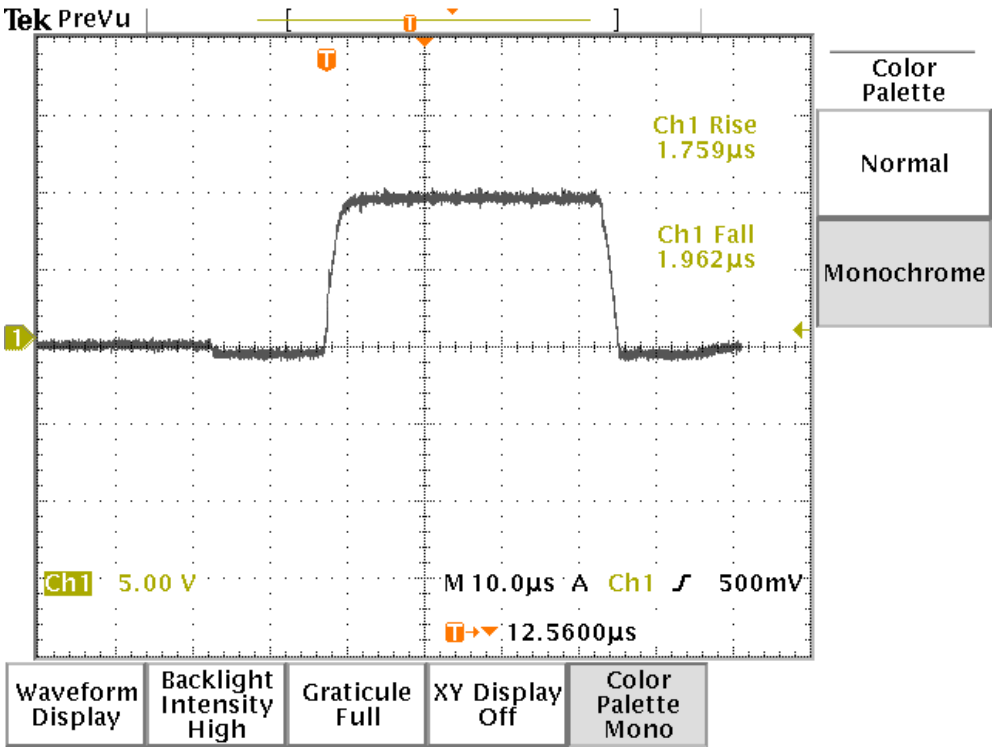

Figure 36 : Single-mode fiber Mach-Zehnder magneto-optic switch switching speed measurement.

4.2 Sagnac Magneto-optic Switch

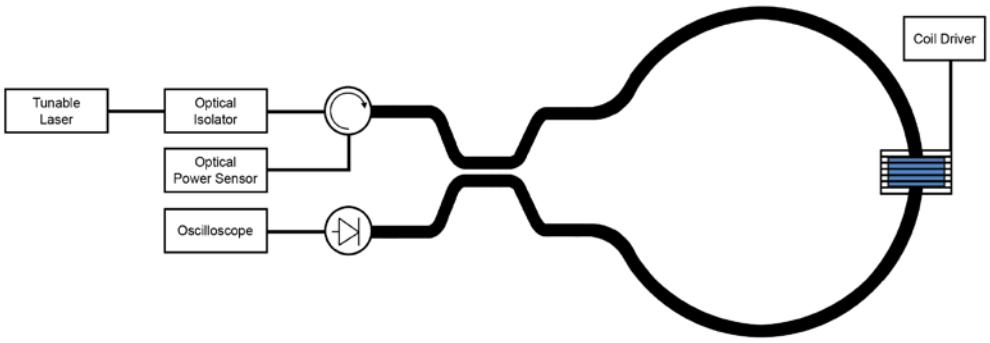

Figure 37 : Laboratory setup for characterizing the Sagnac magneto-optic switch.

The laboratory setup for the experimental evaluation of the fiber-based implementation of the proposed Sagnac magneto-optic switch is shown in Figure 37. A 1550nm laser in an Agilent 8164A Lightwave system is fed into Thorlabs IO-H-1550 optical isolator and subsequently a Thorlands 6015-3 optical circulator before being used as the switch input signal. The isolator prevents the occurrence of back reflections into the laser source, which cause power and wavelength fluctuations. Since the 3dB coupler inputs also act as outputs in the Sagnac configuration, an optical circulator is required on the excited input to enable the measurement of any signal reflected to input 1 / output 1 of the 3dB coupler.

The Faraday rotator is sandwiched between two equal lengths of Corning SMF-28 fiber that comprise the Sagnac loop and was actuated with a dual MOSFET circuit shown in Figure 38 that briefly pre-pulses the field beyond the material saturation limit before settling to a quiescent value. The output optical power was sensed using a Thorlabs DET410C photodetector in tandem with a transimpedance amplifier built around a PN2222 BJT (shown in Figure 39).

A switching field of approximately 13.92kA/m (27.85kA/m pre-pulsed) was required. This produced an extinction ratio of approximately 15dB, a rise time of 0.2μs and a fall time of 0.5μs as shown in Figure 40 (Kemmet, Mina & Weber 2011).

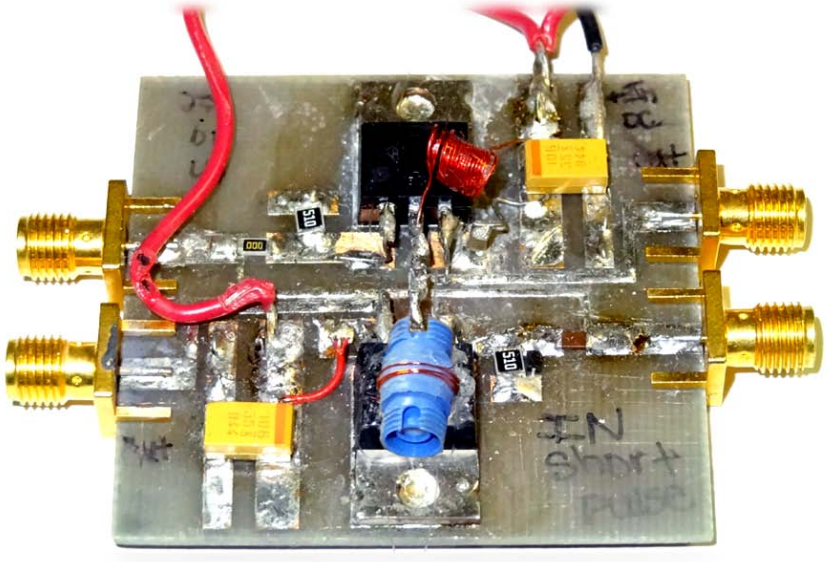

Figure 38 : Dual MOSFET Faraday rotator actuation circuit.

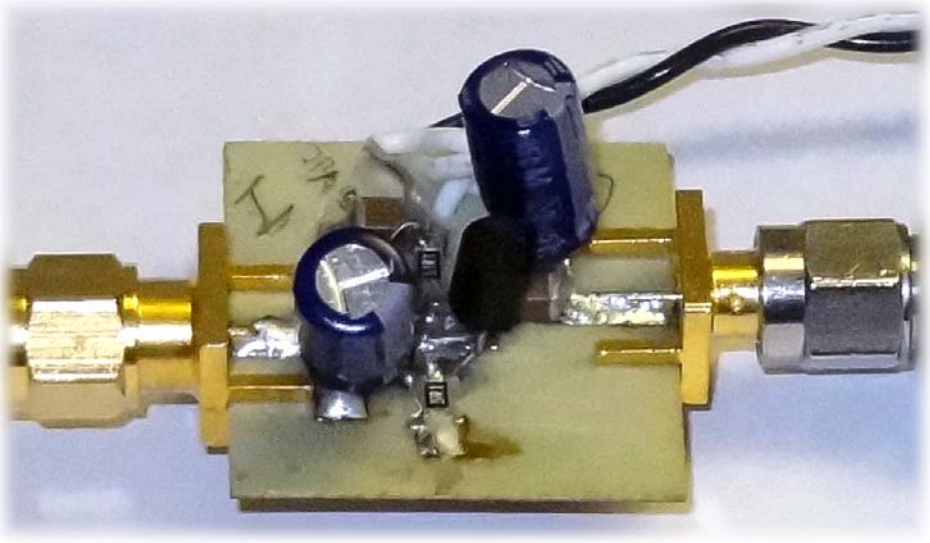

Figure 39 : Transimpedance amplifier circuit to convert the photodiode current to a measurable voltage.

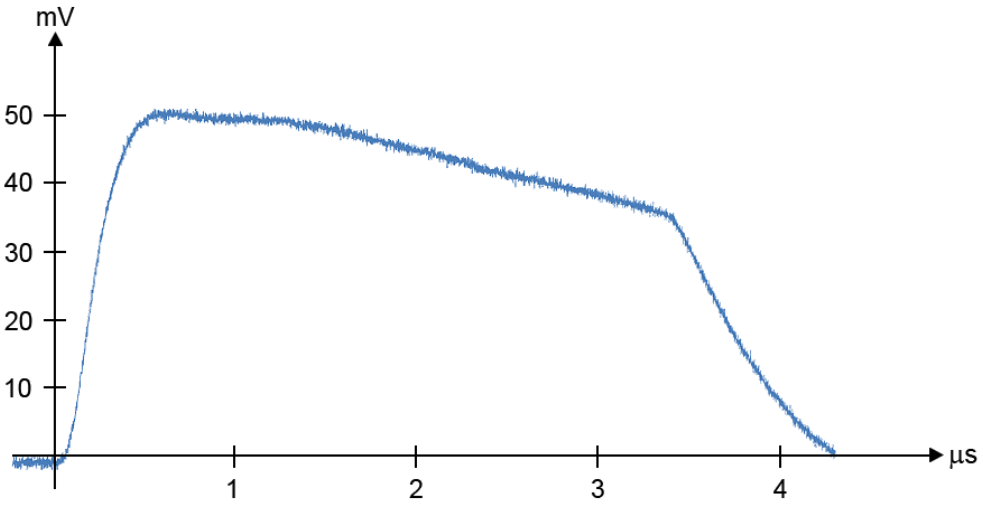

Figure 40 : Single-mode fiber Sagnac magneto-optic switch extinction ratio and switching field measurements.

4.3 Issues and Limitations

While showing promising performance and compatibility with contemporary optical network components, some of the performance metrics of both the Mach-Zehnder and Sagnac magneto-optic switches could certainly be improved.

Commercial optical switches typically have insertion losses on the order of 0.8 – 1dB. The relatively high insertion losses of the fiber-based switches (4.2dB for the Mach-Zehnder, 5dB for the Sagnac) could be lessened by the applying a refractive index matching gel to discontinuities in the switch such as the connectors and fiber-Faraday rotator interface. Doing this would also improve both the repeatability and stability of the measured extinction ratio since the small air gaps in the discontinuities lead to undesirable Fabry-Perot effects. Small changes in the gap size, even a fraction of the optical wavelength would cause large component coupling efficiency changes and hence measured power variations. More seriously in the case of the Mach-Zehnder configuration, this unbalances the optical intensities in the two interferometer arms, degrading the achievable extinction ratio.

In principle, the speed of the polarization plane rotation depends on the velocity of the domain walls. This has been measured to be on the order of 10km/s (Tsang 1978), resulting in a switching time on the order of 100ns (Didosyan, Hauser & Reider 2002). In the Mach-Zehnder switch, this is overshadowed by the large time constant associated with the multi-layer field generating coils due to the high inductance (1.2mH) of such a configuration. The Sagnac switch comes much closer to the theoretical switching limit due to use of a smaller, single-layer field generating coil and improved coil driver circuit topology.

Another concern is the size of the fiber-based switches. Commercial networks often require large switch fabrics; those currently deployed in networks that involve OEO conversion can be as large as 512x512. Since the current switches consist of large, bulky discrete components, they cannot be scaled up to meet network requirements in their current form.

Finally, extinction ratios on the order of 20dB are typically desired in switches, leaving some room for improvement for both the Mach-Zehnder and Sagnac switches. In the fiber-based implementation of the Mach-Zehnder switch, there is an unavoidable difference of approximately 3cm in the interferometer arm lengths due to the use of commercial fiber patchcords. This imbalance severely impairs the interferometric mechanism that is relied on to achieve high extinction ratios due to the imperfection of practical light sources.

The optical fields from laser sources have some random fluctuations associated with them due to factors such as temperature variations and spontaneous emission. Thus only quasi-monochromatic light is achievable in practice, where the effective bandwidth of the light (Δf) is much smaller than its mean frequency. The amplitude and phase of such light is now time dependant and can be shown to vary slowly over a time interval Δt which is short compared to its reciprocal bandwidth ($1/\Delta f$).

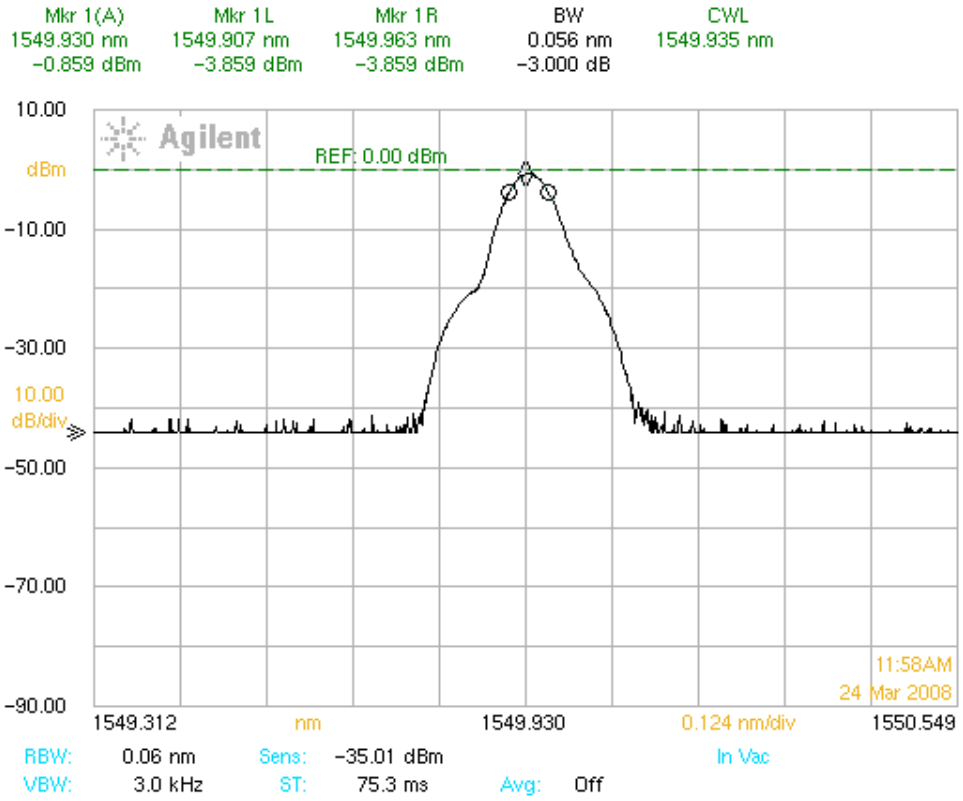

Figure 41 : Agilent 8164A tunable DFB laser spectrum.

For quasi-monochromatic light split into two beams in the Mach-Zehnder interferometer, if Δt is sufficiently small, strong interference fringes are formed. It is empirically known that interference fringes will be observed only as long as $\Delta t \leq 1/\Delta f$. This can be understood by considering the interference patterns formed by each spectral component of the quasi-monochromatic light. After a certain time delay, termed the coherence time of the light, the individual intensity patterns fall out of step and eventually cancel out. This can be converted to a path delay through the medium under consideration :

$$\Delta L = \frac{\overline{\lambda}^2}{n\Delta\lambda} \tag{4.1}$$

where $\bar{\lambda}$ is the mean wavelength, $\Delta\lambda$ is the effective wavelength range and n is the refractive index of the material being considered. The tunable distributed feedback laser in the Agilent 8164A Lightwave system used to characterize the switch has the spectrum shown in Figure 41 as measured with an Agilent 86140B optical spectrum analyzer, giving a coherence length of 2.98cm. Thus the constructive and destructive interference effects in the Mach-Zehnder switch are not as strong as they ideally should be and the switch extinction ratio suffers as a result.

4.4 Field Generating Coil Impedance Modelling

Detailed modeling and measurement of the coil impedance parameters have to be performed in the process of investigating improved driver and coil configurations to increase the speed of the fiber-based magneto-optic switches. New, tractable methods for the calculation of the inductance and shunt capacitance of field generating coils have been proposed and are described below.

4.4.1 Capacitance

Attempts to realize field-generating elements inevitably results in at least two residual parameters - series resistance and shunt capacitance. Although the existence of this capacity is recognized, it is usually determined a posteriori, with design efforts concentrated on the inductance and loss parameters (Bartoli, Reatti & Kazimierczuk 1994; Dowell 1966; Flanagan 1986; Grossner 1983; Jutty, Swaminathan & Kazimierczuk 1993). To date, modeling efforts have been based on either the empirical (Grandi, Casedei & Reggiani 1997; Maurice & Minns 1947; Medhurst 1947) or numerical electrostatic field equation results (Anicin et al. 1997) of a particular winding. While providing notable physical insights,

these results do not necessarily apply to other arbitrary winding configurations. The effect of air gaps between adjacent winding turns is also neglected due to the difficulty of evaluating the electric field paths in the region.

An improved and tractable method for modeling the stray capacitance of field generating coils was proposed that draws upon the work of Massarini and Kazimierczuk (Massarini & Kazimierczuk 1996). The advantage of this approach (as compared to full numerical solutions of the electrostatic field equations) lies in the model simplicity, which affords simple and fast computations of the capacitance.

Under assumed quasi-static conditions, the conductors are considered as equi-potential surfaces with normal electric fields. Thus for a unit surface on the conductor :

$$dC = \varepsilon_r \varepsilon_0 \frac{dA}{x} \tag{4.2}$$

where *dC* is the capacitance corresponding to a unit surface on the conductor (*dA*), $\varepsilon_r\varepsilon_0$ is permittivity of the medium and *x* is the path length of the electric field connecting the unit surfaces on two conductors. The path length is not constant and is a function of the location the unit surfaces. In the case of a circular conductor, this can be described by an angular coordinate as illustrated in Figure 42.

The capacitance of the insulation layer is readily obtainable by assuming a radial field in the insulating material. The combined capacitance per unit angle of both insulation layers is thus given by :

$$dC_{insu} = \frac{\varepsilon_r \varepsilon_0 L}{2\ln\left(1+t/r_c\right)} d\theta \tag{4.3}$$

where t is the thickness of the insulation layer, r_c is the conductor radius and L is the winding turn length. Since the path length of the electric field in air is angle dependent, the capacitance per unit angle for the space between the windings can be written as :

$$dC_{air} = \frac{\varepsilon_0 L (r_c + t)}{2(r_c + t)(1 - \cos\theta) + s} d\theta \tag{4.4}$$

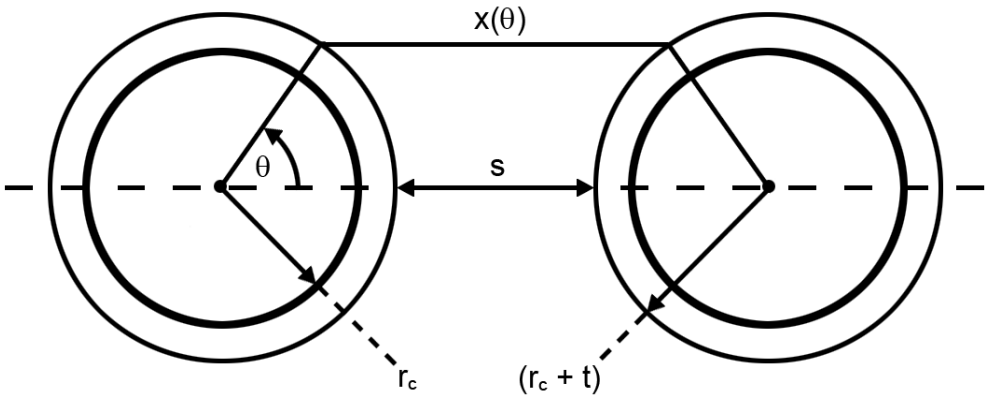

Figure 42 : Capacitance model coordinate system definition.

The elementary turn-to-turn capacitance can then be obtained from the series combination of capacitances given in Equations 4.3 and 4.4. This expression can be modified to give the turn-to-turn capacitance to any neighboring turn k, where $|k| = 1$ is an adjacent turn. The total turn-to-turn capacitance is obtained by integrating the modified expression :

$$\begin{aligned} C_{tt_k} &= 2\int_0^{\pi/2} \frac{\varepsilon_r \varepsilon_0 L (r_c + t)}{2(r_c + t)\left[\ln(1 + t/r_c) + \varepsilon_r (1 - \cos\theta)\right] + \varepsilon_r \left[|k| s + 2(|k| - 1)(r_c + t)\right]} d\theta \\ &= \frac{4\varepsilon_r \varepsilon_0 L (r_c + t)}{\sqrt{B^2 - (2\varepsilon_r (r_c + t))^2}} \tan^{-1}\left(\sqrt{\frac{B + 2\varepsilon_r (r_c + t)}{B - 2\varepsilon_r (r_c + t)}}\right) \end{aligned} \tag{4.5}$$

where B is defined as :

$$B = 2(r_c + t)\left[\ln\left(1 + t/r_c\right) + \varepsilon_r\right] + \varepsilon_r\left[|k|s + 2(|k| - 1)(r_c + t)\right] \tag{4.6}$$

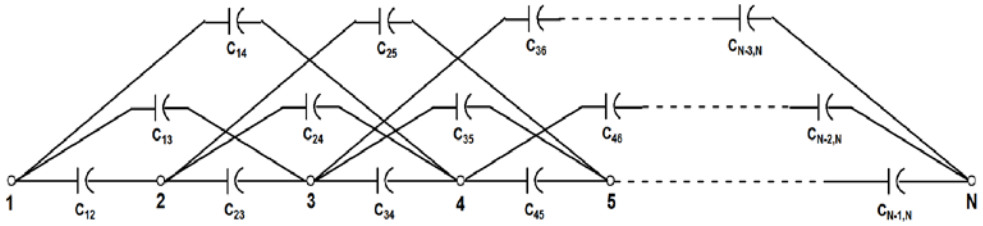

Figure 43 : Distributed capacitance network of a winding.

At high frequencies, a winding is better represented by the distributed capacitance network in Figure 43, where each node represents one turn. The network in can be represented by an *NxN* admittance matrix as in Equation 4.7. Here I_i, Y_{ij} and V_j is a current, admittance and voltage respectively, where i = 1…N and j = 1…N. For a turn m, only its coupling with turns *m-2*, *m-1*, *m+1*, and *m+2* are considered. Thus the admittance matrix entries corresponding to the unconsidered elements are simply set to zero. In this case Y_{mj} = 0 for j {*m-2*, *m-1*, *m*, *m+1*, *m+2*}.

$$\begin{bmatrix} I_1 \\ I_2 \\ \vdots \\ \vdots \\ I_N \end{bmatrix} = \begin{bmatrix} Y_{11} & Y_{12} & \cdots & \cdots & Y_{1N} \\ Y_{21} & Y_{22} & \cdots & \cdots & Y_{2N} \\ \vdots & \vdots & \cdots & \cdots & \vdots \\ \vdots & \vdots & \cdots & \cdots & \vdots \\ Y_{N1} & Y_{N2} & \cdots & \cdots & Y_{NN} \end{bmatrix} \begin{bmatrix} V_1 \\ V_2 \\ \vdots \\ \vdots \\ V_N \end{bmatrix} \tag{4.7}$$

The equivalent stray capacitance between the two winding terminals, the intermediate nodes have to be eliminated. This node reduction can be accomplished by recursive π-T transformations. Here Kron reduction (Kron 1939) is utilized with a modified primitive admittance matrix, where corresponding changes are made in the current and

voltage matrices. This matrix can be rewritten as follows, where *p* denotes a primitive admittance :

$$\begin{bmatrix} [I_a]_{2x1} \\ [I_b]_{N-2x1} \end{bmatrix} = \begin{bmatrix} [Yp_{aa}]_{2x2} & [Yp_{ab}]_{2xN-2} \\ [Yp_{ba}]_{N-2x2} & [Yp_{bb}]_{N-2xN-2} \end{bmatrix} \begin{bmatrix} [V_a]_{2x1} \\ [V_b]_{N-2x1} \end{bmatrix} \tag{4.8}$$

After some algebraic manipulation, Equation 4.9 is obtained. The internal nodes have thus been eliminated and the equivalent admittance between the two winding terminals is given by the non-diagonal terms in Y_{aa}. This is equivalent to $-j\omega C_{eq}$ and the field generating coil capacitance can thus be obtained.

$$[Y_{aa}]_{2x2} = [Yp_{aa}]_{2x2} - [Yp_{ab}]_{2xN-2} \cdot [Yp_{bb}]^{-1}_{N-2xN-2} \cdot [Yp_{ba}]_{N-2x2} \tag{4.9}$$

4.4.2 Inductance

Magnetic fields of controlled amplitude and uniformity are integral to a great many devices and applications. This is achieved by injecting known currents into suitable structures, including the quintessential coil. For the intents of this discourse the field generating coil size and power consumption of its driver circuit need to be minimized while maximizing field intensity and switching speed. Towards this end, a new inductance calculation procedure was proposed to more accurately predict the inductance of coil configurations a priori. The calculation of the mutual or self-inductances of coils or loops is of fundamental practical interest to electrical engineers and physicists. This may be solved using purely numerical methods such as the boundary-element and finite-element methods. However the cylindrical symmetry of the coils in the most commonly encountered cases strongly suggests that at least a semi-analytical solution is possible. The proposed approach

departs from the simplified uniform current distribution assumption, taking into account the influence of current crowding due to both the skin and proximity effects.

When alternating current flows in a conductor, its distribution is not uniform over the conductor cross-section. This arises from the generation of eddy currents, which are to be found in any conducting material that is subjected to a time-varying magnetic field due to the finite conductivity of the material. Although having the same root cause, the non-uniformity of the current distribution is termed either the skin or proximity effect. The skin effect occurs in a conductor carrying a time-varying current. This current generates a changing magnetic field that induces eddy currents in the conductor itself, forcing current to the outer surface thereby increasing effective resistance and decreasing internal inductance.

The proximity effect occurs when other nearby conductors that are also carrying time-varying currents generate magnetic flux. The flux penetrates one particular conductor and generates eddy currents, altering its cross-sectional current distribution. Current density is greatest in the portion of the conductor encircled by the smallest number of flux lines thus limiting the cross-sectional area over which current flows. A conductor's effective resistance is thereby increased and its internal inductance altered.

Previous approaches have included the assumption of a uniform current distribution across the entire conductor cross-section, use of a discretized volume distribution of circular current loops (ie. uniform current distribution within each interval) as well as the assumption of an arbitrary current distribution form (eg. K/r).

In the proposed approach, field generating coil helicity was ignored with the coil being approximated by series connected coaxial rings with finite circular cross-section. The method of successive approximations (Lammeraner & Stafl 1964) was used to estimate the actual cross-sectional current distribution by assuming that only directly adjacent turns play

a role. Turns at the end of the coil constituted a two conductor problem whereas turns in the middle constituted a three conductor problem.

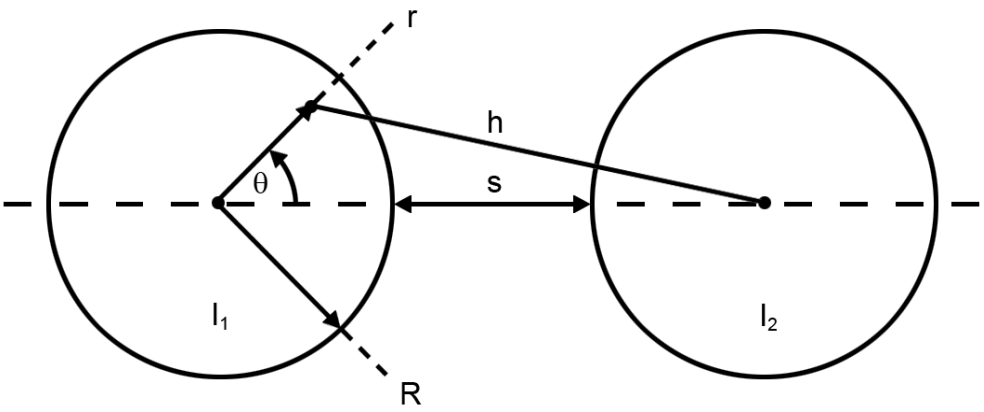

Figure 44 : Two conductor successive approximation geometry.

The method of successive approximations begins by assuming a uniform initial current distribution J^0 that generates a magnetic field H^0, which in turn induces the first order eddy current J^1. The time variation of this current generates a first order field H^1 and this process continues ad infinitum. The final cross-sectional current distribution is the sum of these successive approximations. For the two conductor problem shown in Figure 44 this can be expressed as in Equation 4.10. A similar expression can be obtained for three conductors.

$$J(r,\theta) = \frac{(j\omega\mu\sigma)^2}{4} J^0 \left[\left(r^2 - \frac{R^2}{2} \right) + R^2 \ln \left(1 - 2\frac{r}{(R+2s)} \cos(\theta) + \frac{r^2}{(R+2s)^2} \right) \right] \qquad (4.10)$$

Maxwell developed an expression for the mutual inductance of two coaxial circular current loops using complete elliptic integrals (Maxwell 1904) :

$$M_{21} = \mu_0 \frac{\sqrt{R_2 R_1}}{k}\left[\left(2-k^2\right)+K(k)-2E(k)\right] \tag{4.11}$$

where k is defined as :

$$k = \sqrt{\frac{4R_2R_1}{\left(R_2+R_1\right)^2+\left(z_2-z_1\right)}} \tag{4.12}$$

The proposed approach uses an alternative formulation involving the integral of Bessel functions :

$$M_{21} = \mu_0 \pi R_2 R_1 \int_0^\infty J_1\left(sR_2\right) J_2\left(sR_1\right) e^{-s|z_2-z_1|} ds \tag{4.13}$$

The radial and axial coordinates are separated rather than convolved as in the elliptic integral formulation. This permits analytical integration over the conductor cross-section to yield the total inductance and self inductance is obtained when the loops coincide in space. The expression can be numerically evaluated or transformed to elliptic or other angular integrals for more efficient evaluation. Combining the filamentary inductance and current distribution expressions and then integrating over the conductor cross-section, the various inductance parameters can then be found.

4.4.3 Inductance Minimization

The design of field generating coils consistent with stringent field specifications is of great importance in many scientific applications, e.g. non-destructive evaluation and magnetic resonance imaging. This is notionally a simple problem; specify a desired magnetic field in the coil interior and find the corresponding current density on the coil

surface. This direct approach engenders great difficulties since it requires solving a Fredholm integral equation of the first kind to determine a required current density, a non-trivial ill-posed problem (Hadamard 1902; Greene 1965; Laslett 1966; Merkel 1987) since the field is not a unique function of current density distribution and hence winding pattern. While this difficulty can be assuaged by the use of techniques such as Tikhonov regularization or ridge regression (Tikhonov & Arsenin 1977), the solution quality is potentially impacted due to artifacting since it depends in a discontinuous way on the desired field.

A well known approach to designing coils is the target-field method proposed by Turner, which is based on the cylindrical Fourier transform (Turner 1986). This sidesteps the ill-posed mathematical nature of the design problem, since Fourier transforms are well posed problems with unique inverses. While successful, its reliance upon the Fourier transform implies that there is no explicit constraint on coil dimensions, which can lead to overly large coils should the target field be improperly specified. Truncating the coil to more practicable dimensions requires careful evaluation of the current density decay rate to ensure convergence of the Fourier integral. This is typically addressed via apodization, ie. the use of smoothing functions to remove the higher spatial harmonics from the Fourier current distribution. Unfortunately, this negatively affects the obtained solution quality. Additionally, since a continuous current distribution is used during computations, a discretized approximation must be made using stream functions to obtain the final winding pattern, further degrading solution quality.

A new and flexible approach is described for the systematic design of coils to produce any desired field configuration while minimizing inductance. A coil is represented as a sequence of circular current carrying loops and stochastic minimization (with an

appropriate cost function) is utilized to determine the location and current for each loop. The approximation stage in sampling a continuous current density with a finite number of windings is no longer necessary. Direct constraints are easily incorporated on the final wire pattern, thereby enabling the design of coils with genuinely finite dimensions.

The stochastic optimization technique chosen in this work is simulated annealing, an algorithm first published by Metropolis et. al. (Metropolis et al. 1953) and improved by Kirkpatrick et. al. (Kirkpatrick, Gelatt & Vecchi 1983). It was inspired by the annealing process in thermodynamics, where a material system is slowly cooled in order to achieve its lowest energy state and mimics nature's own minimization algorithm based on the Boltzmann probability distribution. Unlike "greedy" linear search methods such as steepest descent (Fletcher 1980), simulated annealing allows a number of positive energy excursions and hence avoids being trapped in a local minimum of the solution state search space. Negative excursions are always accepted while positive excursions are accepted with a probability that decreases with the amount of increase in energy (ΔE) and is controlled by a temperature parameter (T) as expressed in Equation 4.14, where k is Boltzmann's constant. It is clear that higher values of T enable more of such excursions to be accepted.

$$p_{accept} = e^{-(E'-E)/kT} = e^{-(\Delta E)/kT} \tag{4.14}$$

During the initial stage of a simulated annealing run, T is set to a suitably high value to enable a rough mapping of the error surface of the system to be optimized. On subsequent iterations, T is reduced according to a cooling schedule so that energy increasing moves are less likely to be accepted. This schedule is typically of the form $T' = \alpha T$ (where α is typically around 0.95) or $T' = e^{-\beta T} T$ (where β is typically around 0.7). Finally, T reaches a very low value so that only excursions causing an energy reduction are

accepted and the algorithm converges to a low energy configuration. The system is then said to be frozen.

A good choice of values for the various parameters controlling the annealing process is crucial in ensuring that the algorithm produces good solutions for a wide variety of problem setups while using a minimum of computational resources. One critically important point is that the cooling schedule should not be overly aggressive as to cause the system to quench, thereby never reaching its minimum energy state. Provided this advisory is observed, the simulated annealing algorithm is guaranteed to converge to the global minimum (Mitra, Romeo & Sangiovanni-Vincentelli 1985; Van Laarhoven & Aarts 1987; White 1984).

Simulated annealing may be readily adapted to field generating coil design. The error function (*E*) to be minimized may be a combination of a number of coil properties, e.g. uniformity, inductance and loss as shown below :

$$E = W_1.\max\left(\frac{\left|B_z(r_a,z_i) - B_z(r_a,z_a)\right|}{B_z(r_a,z_a)}\right)_{i=1,\ldots N} + W_2.L + W_3.R \qquad (4.15)$$

where *N* is the number of sampling points in the volume of interest. $B_z(r_a,z_i)$ represents the calculated *B* field at equally spaced points on a line in the volume of interested that is either parallel to or coincident on the coil axis (depending on the value of *a*). *L* and *R* are the coil inductance and resistance respectively while W_1, W_2 and W_3 are arbitrarily adjustable weighting factors having units such that *E* evaluates to a dimensionless value. Field constraints must always be included or a trivial solution will be obtained, since the minimum inductance current density that is not constrained to produce any field is simply zero everywhere.

Suitable values for the simulated annealing parameters were chosen empirically by performing several tuning runs. An overly high starting temperature results in wasted computational resources, while one that is overly low does not permit sufficient entropy to reach the global rather than a local minimum. The step size controls the spatial increments of the individual circular current loops as they are randomly moved around during the simulated annealing process. As runtime was not an issue in the design of the field generating coil, safe and conservative values were chosen for the parameters above to ensure that a high solution quality is attained.

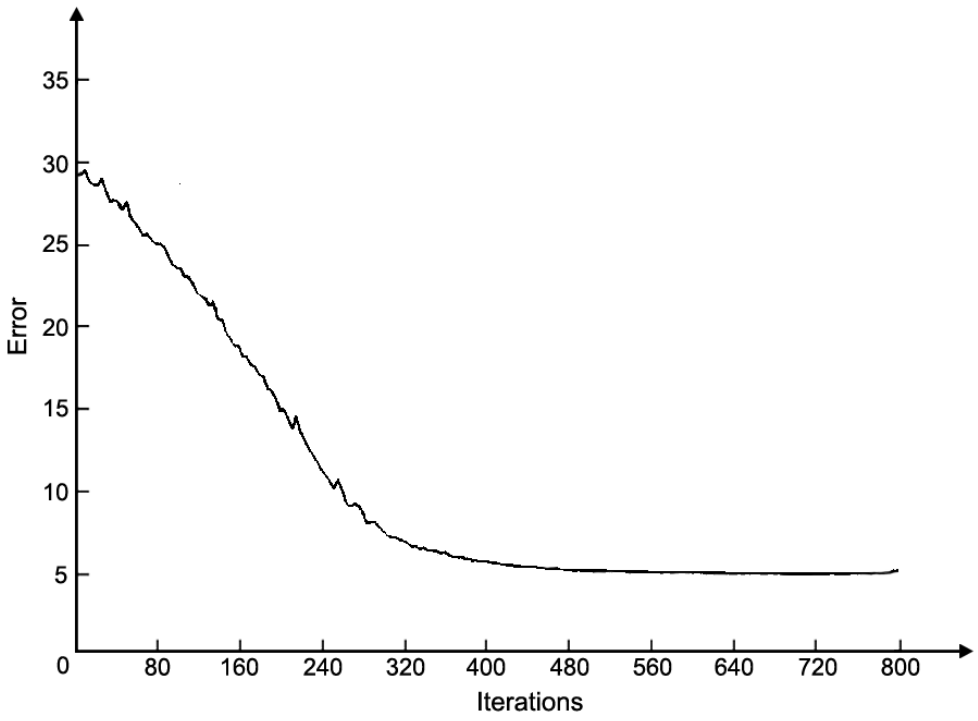

Figure 45 : Cost function variation during the simulated annealing process.

The simulated annealing algorithm was implemented in the C programming language and compiled using the gcc 4.1.2 compiler. Optimization runs were made on the Redhat Linux operating system running on a 3.6GHz Intel Core2 Duo (Conroe) processor. A step

size of 5% the length of the field generating coil and a starting temperature of 1 were utilized. The annealing parameters were set to empirical values : $\alpha = 0.85$, $T_{freeze} = 10^{-4}$.

Figure 45 illustrates the behavior of the algorithm during an optimization run. While the temperature remains high, a random sampling of the solution state space occurs. At lower temperatures the annealing begins and the curve decreases, showing a decrease in entropy and finally freezing at the global minimum. An example of a coil configuration that results in minimum inductance is shown in Figure 46.

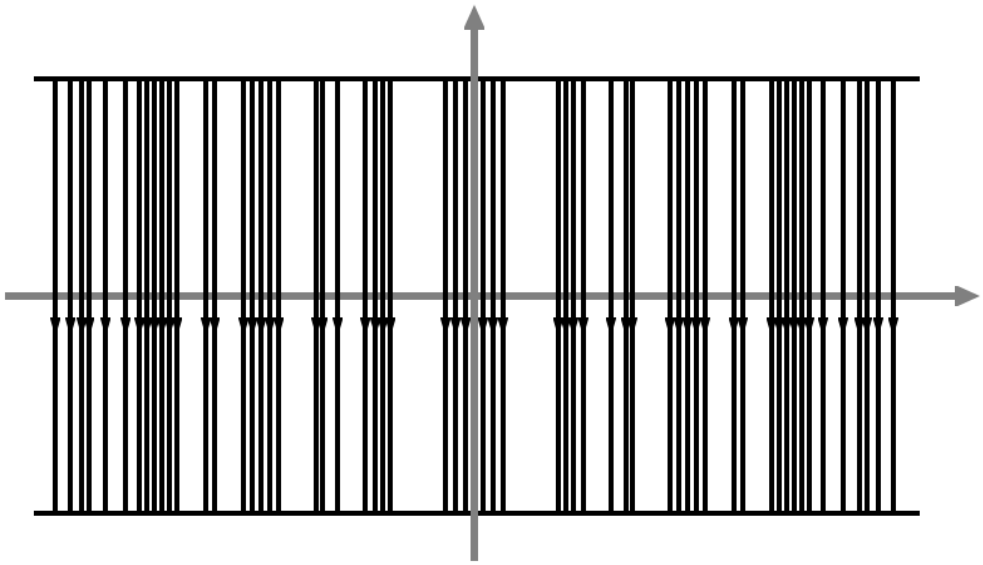

Figure 46 : Discrete current distribution for the minimum inductance field generating coil.

CHAPTER 5. INTEGRATED MAGNETO-OPTIC SWITCHES

Richard Feynman delivered a famous lecture at an American Physical Society meeting held at California Institute of Technology in 1959 entitled “There’s Plenty of Room at the Bottom” (Feynman 1960). He delivered an extraordinarily prescient view of the potential of what is now commonly termed nanotechnology, discussing the manipulation and control of things on a small scale. The microelectronics industry has certainly taken this to heart, where performance advances following Moore’s law depend on device miniaturization to allow for ever larger scale integration of complex electronic systems. Indeed, the atomic scale constitutes the fundamental limits of device miniaturization, which is about three orders of magnitude smaller than the scale of contemporary devices fabricated using optical lithography. Novel lithographic techniques, such as electron beam lithography, chemical or electro-chemical lateral structuring and scanning probe microscopy techniques result in structures of only a few nanometers in size and allow the manipulation of individual atoms.

It is no question that microelectronics has had a deep and widespread impact on modern civilization. Microphotonics has this same potential and there have been considerable efforts toward microphotonic integration over the course of the last decade to enable compact, manufacturable and low-cost components. The integrated circuit revolution of the 60s clearly demonstrated the tremendous potential afforded by planar lithographic techniques and these are the very techniques that are now being used to enable microphotonics. Planar integration mitigates alignment issues, reduces coupling losses between once discrete components and shrinks the size and fabrication cost of complex elements.

Due to the optical network overcapacity created by the Internet boom of the 90s, cost rather than performance is the key criteria for next generation optical network components. Integrated magneto-optic switches are a possible solution for constructing a high-performance, low-cost and scalable all-optical switch for next generation networks.

5.1 Material System

Stewart Miller first coined the term “integrated optics” in 1969 when comparing integrated electronic circuits and planar optical circuit technology (Miller 1969). The concept he proposed was optical circuits formed by the combination of various passive and active elements onto a single substrate where they would be interconnected via optical transmission lines. Integrated optical devices have been implemented in a number of material systems, each with distinct advantages and disadvantages. The fabrication techniques used are either borrowed or adapted from the semiconductor industry, especially in academic research where compatibility with semiconductor processing equipment retired from industrial facilities is paramount.

The basic requirements of a material system suitable for integrated optical devices are that it offers a sufficient effective index contrast between the core (high-index) and cladding (low-index) structures as well as low loss at the typical optical communications windows. Beyond this, the usefulness of a material system is also determined by the controllability of waveguide structure dimensions and integrability, ie. the ease of which waveguiding structures can be integrated with other optical or electronic components. Other desirable characteristics could include particular sensitivities (eg. acoustic or thermal) and native light emission and detection capabilities.

One of the most popular materials for integrated optical devices is lithium niobate ($LiNbO_3$) due to its piezo-electric, acousto-optic and electro-optic properties (Kissa et al. 2000), making it ideal for constructing devices such as phase modulators, switches and multiplexors. $LiNbO_3$ devices are fabricated by either Ti diffusion or annealed proton exchange, both of which tend to produce graded rather than step index profiles. The prospects of integrating $LiNbO_3$ with conventional silicon-based microelectronics are somewhat bleak as many of its valuable properties are lost when it is not grown in single crystal form.

Another popular class of materials is III-V compound semiconductors, usually GaAs and InP in the form of $Al_{1-x}Ga_xAs$ and $In_{1-x}Ga_xAs_{1-y}P_y$ (Volterra & Zimmerman 2000; Wakao, Soda & Kotaki 1999). The index of refraction is readily controlled by adjusting the dopant concentration during the deposition process, yielding indices ranging from 3.1 – 3.5. The importance of III-V compounds stems from the fact that they are readily integrated with active elements, namely lasers and detectors. However, waveguides made of these materials have relatively high losses (> 1dB/cm). III-V compounds are also difficult to grow epitaxially on silicon substrates and have a high propensity for contaminating silicon devices due to being shallow-level dopants in silicon, introducing threshold voltage shifts.

A combination of silicon nitride (Si_3N_4) and silicon oxynitride (SiON) was recently proposed as a suitable platform for integrated optical devices (Bona, Germann & Offrein 2003; Kobrinsky et al. 2004), offering a high refractive index contrast and hence very compact waveguides with tighter light confinement. However, Si_3N_4 contains residual N-H bonds that cause the material to be lossy at 1500nm. While this can be alleviated by high-temperature annealing, the temperatures involved are not compatible with standard electronic devices.

Applications requiring stronger electro-optic, thermo-optic and piezo-electric effects than in a $LiNbO_3$ material system turn to various polymers, such as polymethylmethacrylate (PMMA), polycarbonate, perfluorocyclobutyl, polyacrylates and polyimides (Cowin 2001; Halldorsson et al. 2010). Polymers are especially useful for chemical and biological sensors as the organic groups in the polymeric compounds can be tailored to react to different specific media. However, polymer waveguides tend to have higher losses than their dielectric counterparts. There is also the issue of integrability with conventional microelectronics as most standard lithographic techniques cannot be applied to polymeric layers due to the solvents present in photosensitive resists. Polymer waveguides are also limited in their use to the uppermost layers after electronic devices have been fabricated as they are unable to withstand the high temperatures used in many standard processing steps.

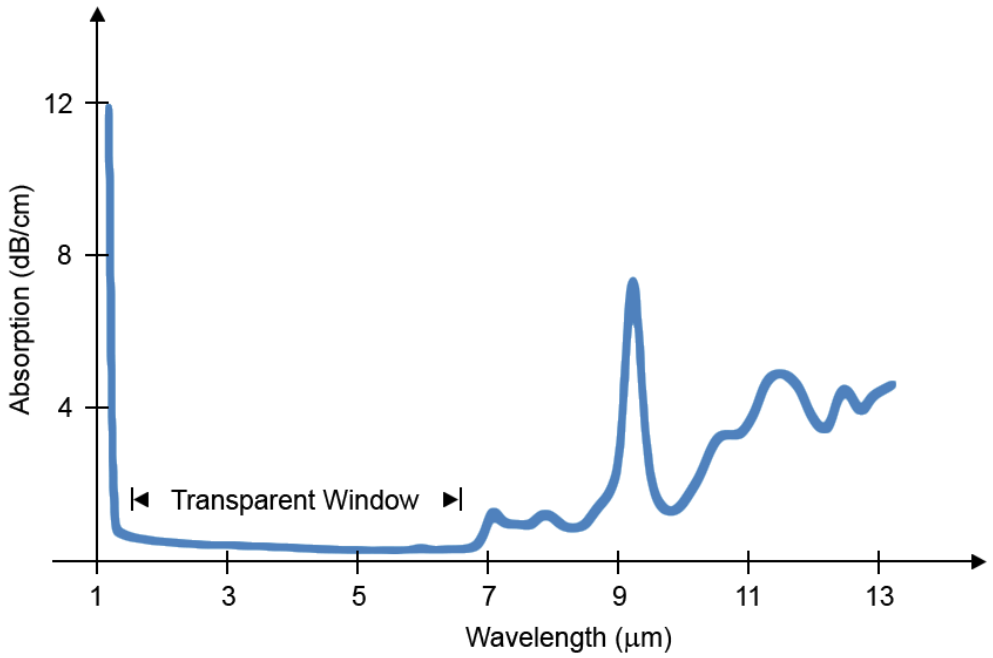

Figure 47 : Absorption of silicon as a function of wavelength.

Finally, another useful platform for integrated optics is silicon-on-insulator. Silicon has a bandgap of 1.12eV, placing its absorption band edge at 1.1μm and providing a transparent window from 1.2–6.5μm as shown in Figure 47. Utilizing silicon as a waveguiding material is clearly advantageous for the integration of photonic and electronic devices. Early efforts used doped silicon to provide the necessary index contrast (Brown et al. 1987; Foresi et al. 1996; Kawachi 1990; Soref & Lorenzo 1985). However, the achievable index contrast was low, resulting in weak optical confinement and necessitating large device dimensions. Furthermore, the introduction of impurities greatly increased waveguide losses. Silicon-on-insulator technology relies on a low-index cladding material being positioned between the core and substrate silicon layers for optical confinement. Fortunately, silicon has a high-quality native oxide that fulfills this role. With the recent advances in forming buried oxide layers (Celler & Cristoloveanu 2003; Cristoloveanu 2001) due to demands from the microelectronics industry (transistor leakage is greatly reduced with the introduction of an insulating layer), silicon-on-insulator is emerging as viable photonics platform. It offers a very high index contrast ($\Delta n = 2$), enabling extremely compact photonic devices due to tight optical confinement. Moreover, the core and substrate layers in a silicon-on-insulator material system have precisely the same thermal expansion coefficient, eliminating stress-induced birefringence (Milosevic et al. 2008). The most attractive advantage of silicon-on-insulator is its ability for seamless integration into current commercial CMOS process technology. Due to this and the aforementioned advantages, it is chosen as the implementation platform for the proposed integrated magneto-optic switches.

5.2 Design Methodology

Several critical challenges are immediately encountered when translating the proposed fiber-based magnet-optic switch designs to an integrated silicon-on-insulator waveguide based implementation. The first is that while advances have been made in the growth techniques of magneto-optic materials (Tkachuk et al. 2009; Tkachuk et al. 2008), the most popular and successful synthesis technologies are unsuitable for the growth of rare earth garnets on silicon substrates. Pulsed laser deposition requires high substrate temperatures and causes higher surface roughness. Standard magnetron sputtering only works for conductive substrates and is thus immediately ruled out. RF magnetron sputtering sidesteps this requirement by preventing charge build-up in the target but suffers from low deposition rates. Liquid phase epitaxy generally offers the highest quality garnets but requires the target substrate to be single-phase, lattice-matched and capable of withstanding high temperatures (Aichele et al. 2003; Krumme, Doorman & Eckart 1984).

Another challenge to integrating garnets is the substantial difference in lattice constant and thermal expansivity between garnets and silicon. This coupled with the high processing temperatures called for by liquid phase epitaxy and pulsed laser deposition leads to enormous stress at the garnet – silicon interface as the wafer is temperature cycled. Even if successfully integrated, the difference in lattice constants and thermal expansivities leads to stress-induced birefringence, which causes a phase mismatch between modes in the integrated waveguide. This effect is extremely undesirable since it disrupts the conversion efficiency between the modes (polarization rotation) and induces ellipticity.

With these hurdles in mind, a hybrid fabrication technique is proposed to implement the integrated magneto-optic switches where bulk Faraday rotators are slotted in between the waveguides as shown in Figures 48 – 49.

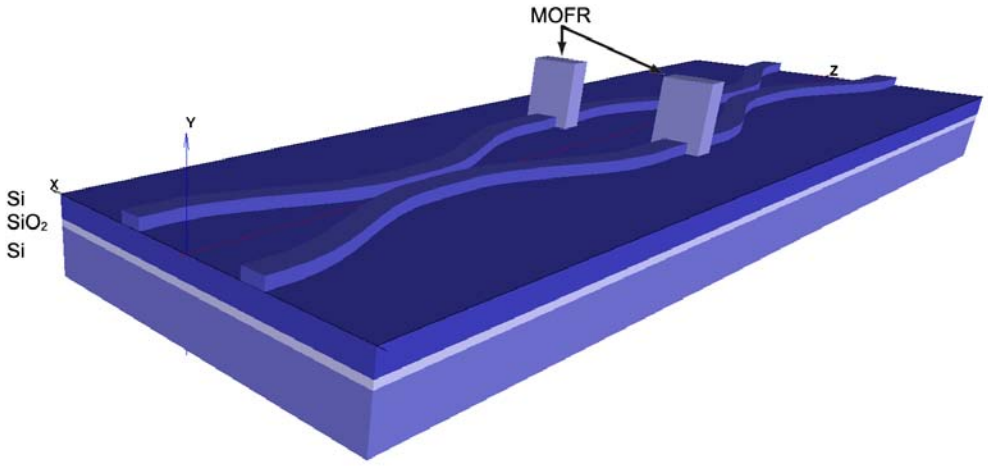

Figure 48 : Structure of proposed integrated Mach-Zehnder magneto-optic switch.

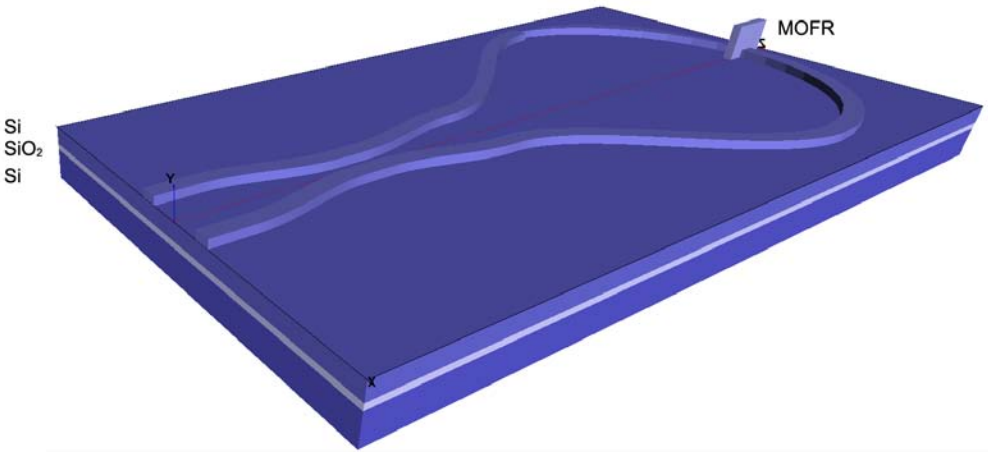

Figure 49 : Structure of proposed integrated Sagnac magneto-optic switch.

5.2.1 Waveguide Structure

The most ubiquitous optical waveguiding structure is the venerable optical fiber and the variety that is universally utilized in long-haul communications is single-mode fiber. It is designed to support a single bound optical mode for each polarization state, which greatly reduces signal dispersion during propagation as compared to its multi-mode counterpart. Optical fibers are weakly guiding, with the core having an index of refraction that is only marginally higher than the cladding (on the order of 0.3%). Due to circular symmetry, there is no preferred polarization axis. However, manufacturing non-idealities cause the polarization state to fluctuate randomly on a ms timescale after a propagation distance of several kilometers (Damask 2005).

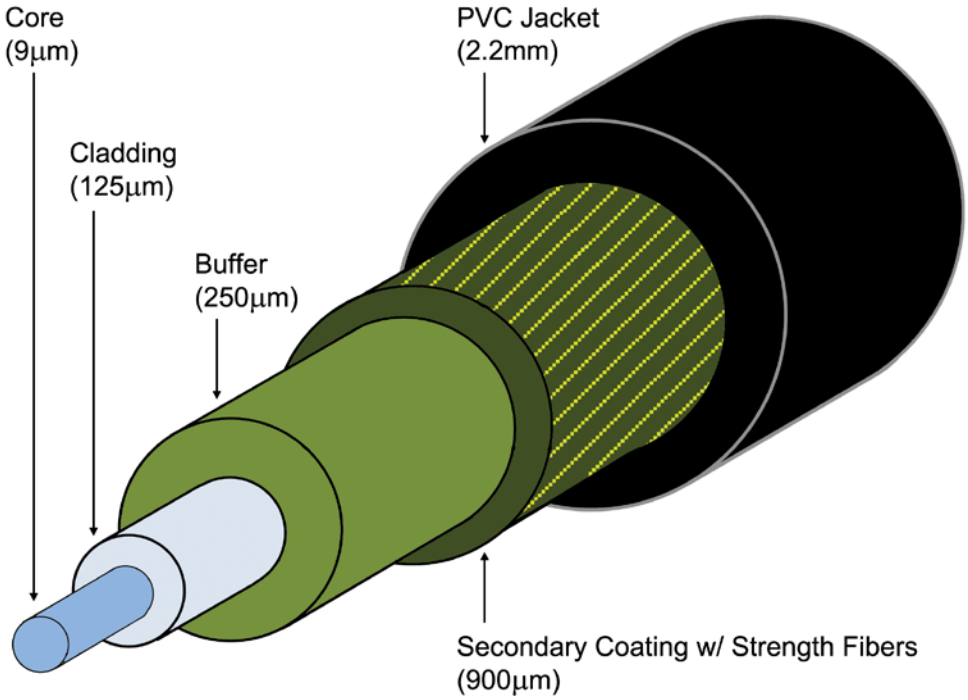

Figure 50 : Construction of single-mode indoor cable.

Single-mode fibers have core diameters of 4–10μm and cladding diameters of 50–125μm. They are available in a number of different cable structures depending on the particular application with a typical indoor cable illustrated in Figure 50. Since a substantial portion of the optical power in single-mode fibers propagates in the cladding, using the core diameter as a measure of the extent of the region carrying the optical signal is insufficient. Thus the concept of the mode-field diameter is introduced (see Figure 51), where the effective core diameter of the fiber is defined as the point where the power decays to 1/e of the peak. Single-mode fibers typically have a mode-field diameter of 10μm.

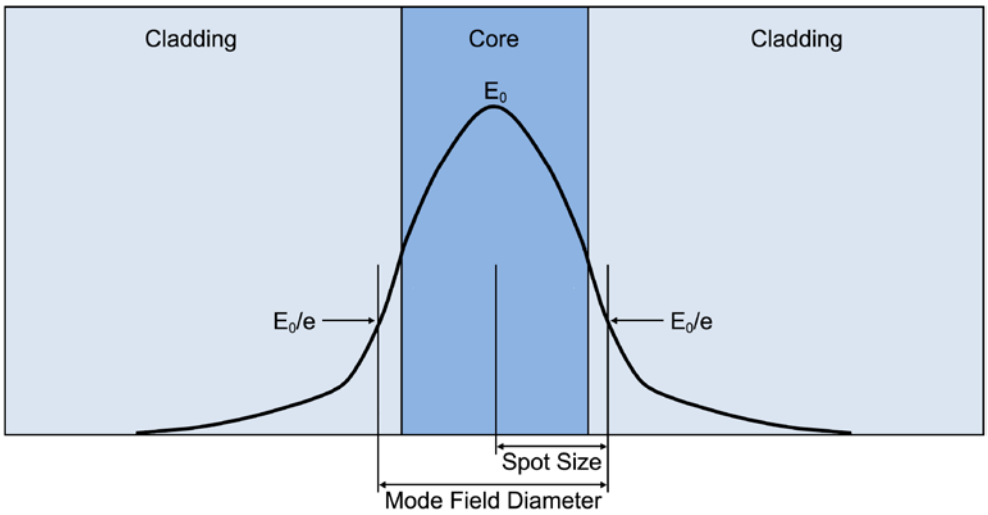

Figure 51 : Mode field diameter and spot size definition.

Integrated waveguides differ from optical fibers in that they are fabricated on planar substrate using some form of lithography and thus have rectilinear cross-sections. This offers a number of significant advantages, including integrability with electronic and other optical devices, increased scalability and more accurate control of waveguide dimensions. However, there are several drawbacks associated with integrated waveguides. The loss of circular symmetry potentially introduces birefringence, which has to be carefully managed

eg. by implementing a polarization diversity scheme. This shaped-induced birefringence is distinct from stress-induced birefringence and originates from the different boundary conditions for the perpendicular and transverse electric field components of the modes at the core-cladding interfaces. Its magnitude depends on the strength of the field components at these interfaces, which in turn is governed by both the waveguide core size and index contrast of a particular material system. This loss of symmetry also necessitates numerical tools and techniques for analyzing these waveguides as purely analytical solutions do not exist (with the exception of the slab waveguide) (Sudbo 1992). Furthermore, the propagation loss per unit length of integrated waveguides is still several orders of magnitude higher than that of optical fiber (dB/cm vs. dB/km).

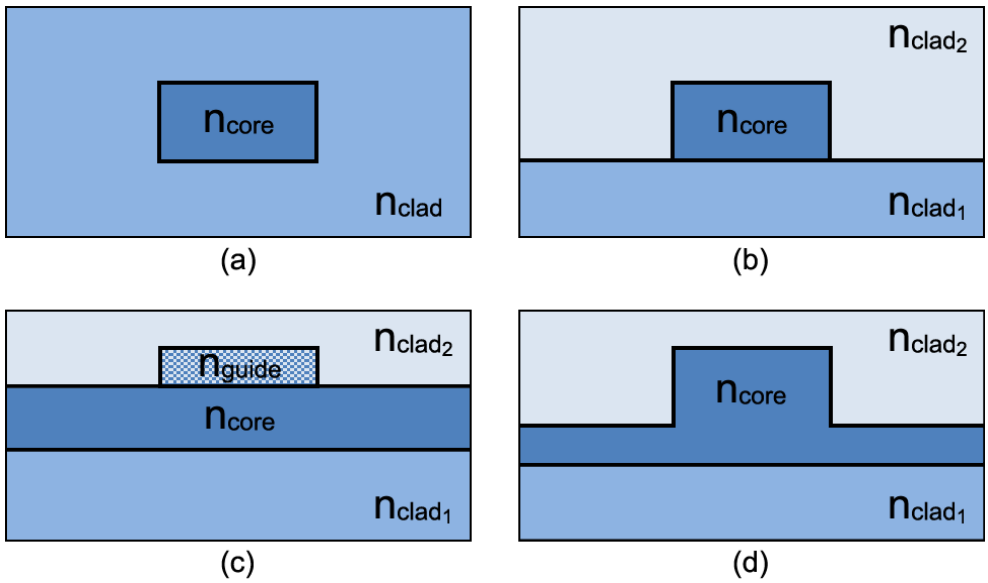

Figure 52 : Waveguide geometry cross-sections : (a) channel, (b) raised strip, (c) strip-loaded, (d) rib.

The most common geometries of integrated waveguides are illustrated in Figure 52. The channel waveguide has a rectangular core region on a lower index substrate and an

overcladding having the same index as the substrate. A variation of this is the raised strip waveguide in which the index of the overcladding is dissimilar to that of the substrate but is still lower than that of the core region. The strip-loaded waveguide is an improved slab waveguide with a loading strip that sits atop the core and has a slightly lower index. This provides two-dimensional confinement of light and mitigates the effect of strip edge roughness on propagation losses, although careful engineering of the strip dimensions is required. Finally, rib waveguides can be thought of as strip-loaded waveguides with the loading strip having the same index as the core layer.

Efficient coupling to optical fiber remains an important consideration when designing integrated waveguides as the present reality is that most integrated optical devices are single elements inserted between stretches of optical fiber rather than elements in a complex optical circuit. A common method of coupling light into integrated waveguides is cleaving the edges of the optical chip and abutting a flat polished fiber surface to the chip facet, a technique known as end-fire coupling that is used in this work and illustrated in Figure 53. This coupling configuration incurs a loss at the abrupt boundary between the two dissimilar waveguides and is a problem that has been treated by many authors (Brooke & Kharadly 1976; Hockham & Sharpe 1972; Ray & Mittra 1984; Rozzi 1978). Minimizing this loss requires a good spatial overlap of the mode profiles as well as a good match of the effective refractive indices in the two waveguides.

The quality of mode matching (η) can be approximately quantified by a simple overlap integral between the modes of the fiber and integrated waveguide as follows :

$$\eta = \frac{\left|\iint \psi_1(x,y)\psi_2(x,y)dxdy\right|}{\sqrt{\iint |\psi_1(x,y)|^2 dxdy \,.\, \iint |\psi_2(x,y)|^2 dxdy}} \tag{5.1}$$

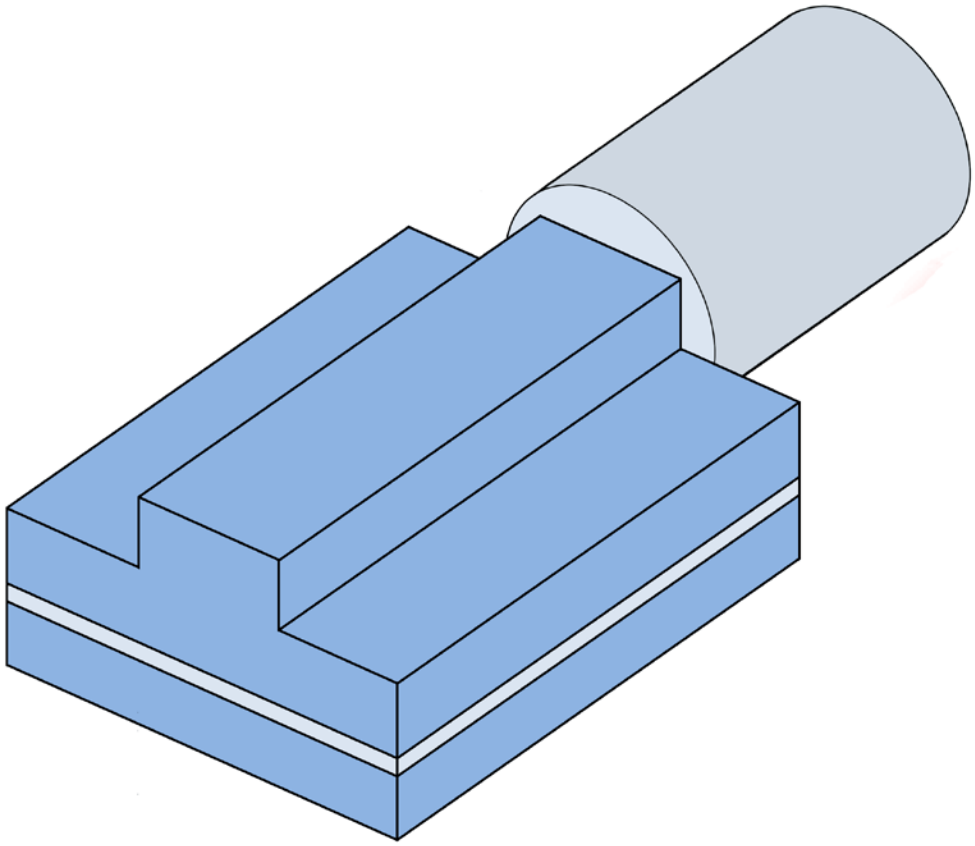

Figure 53 : End-fire coupling configuration involving an abrupt junction between dissimilar waveguides.

where ψ_1 and ψ_2 represent the mode of the optical fiber and integrated waveguide respectively. An additional factor is frequently introduced into Equation 5.1 to account for Fresnel reflection due to the effective index mismatch between the two structures.

The proposed waveguide structure for this work is illustrated in Figure 54. Light is confined in the silicon rib, which sits atop an oxide isolation layer that is sufficiently thick (5000Å in the case of the wafers used in this work) to prevent leakage of the optical mode into the substrate. The use of an air cladding avoids many of the challenging problems of material overgrowth while the rib geometry offers a higher degree of flexibility compared to the channel and raised strip geometries. Channel waveguides are typically restricted to sub-

μm cross-sectional dimensions to ensure that only one bound mode per polarization state is supported due to their larger effective index. In contrast, while single-mode sub-μm rib waveguides could certainly be implemented, relatively large optical modes (several μm) can also be confined without sacrificing single-mode operation (Soref, Schmidtchen & Peterman 1991). This is critical since the end-fire coupling configuration is used in this work and single-mode fibers have core diameters of 4–10μm.

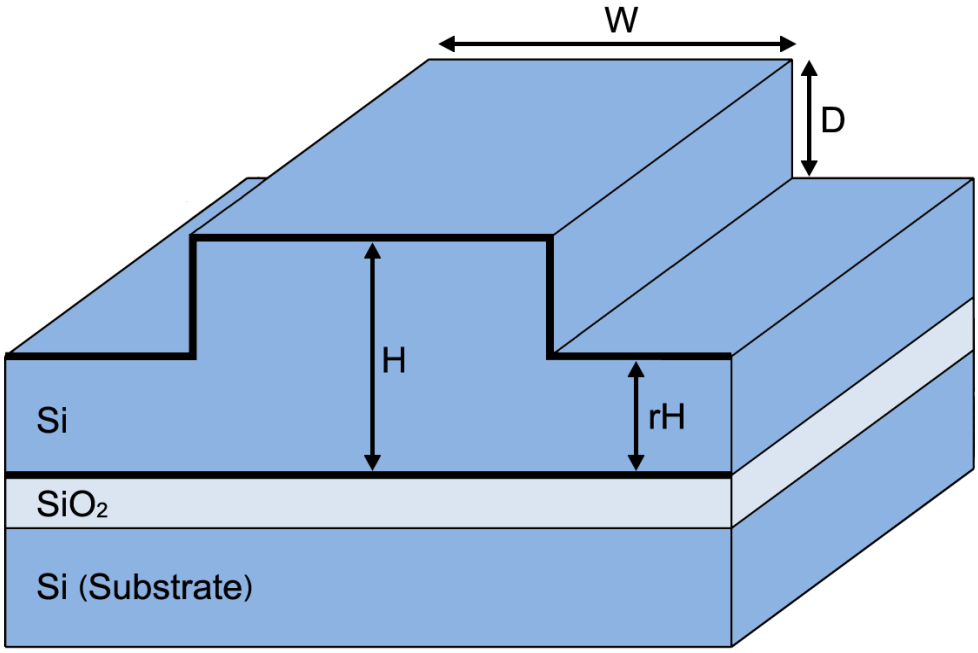

Figure 54 : Silicon-on-insulator rib waveguide geometry. Light is guided in the silicon rib and confined by the air overcladding as well as oxide layer below.

Due to the high index contrast in a silicon-on-insulator material system ($\Delta n \sim 2$ for Si/SiO_2 and $\Delta n \sim 2.5$ for Si/air), rib waveguides with cross-sectional dimensions of larger than several hundred nm support multiple modes. Nevertheless, it is possible to engineer larger rib waveguides such that they exhibit single-mode like behavior by carefully controlling the width (W) and etch depth (D) relative to the rib height (H). The results of a

mode-matching analysis from (Soref, Schmidtchen & Peterman 1991) is utilized to derive the following dimensional relationship for single-mode operation :

$$\frac{W}{H} \le \left(\frac{q + \frac{2\pi H}{\lambda}}{\frac{2\pi H}{\lambda}} \right) \left(\frac{1 + c\sqrt{\left(\frac{q + \frac{2\pi H}{\lambda}}{q + \frac{2\pi r H}{\lambda}} \right)^2 - 1}}{\sqrt{\left(\frac{q + \frac{2\pi H}{\lambda}}{q + \frac{2\pi r H}{\lambda}} \right)^2 - 1}} \right) \qquad (5.2)$$

$$r \ge 0.5$$

where λ is the freespace wavelength in μm, c = 0.3 and q is defined as :

$$q = \left(\frac{\gamma_0}{\sqrt{n_{Si}^2 - n_{air}^2}} \right) + \left(\frac{\gamma_2}{\sqrt{n_{Si}^2 - n_{SiO_2}^2}} \right) \qquad (5.3)$$

The constants γ_0 and γ_2 are defined for quasi TE and quasi TM modes as follows :

$$TE: \quad \gamma_0 = \gamma_2 = 1$$
$$TM: \quad \gamma_0 = \left(\frac{n_0}{n_1} \right)^2 \quad \gamma_2 = \left(\frac{n_2}{n_1} \right)^2 \qquad (5.4)$$

The imposed restriction of r ≥ 0.5 can be understood qualitatively by thinking of the higher order modes in the rib as becoming “leaky” and eventually dissipating after a sufficiently long propagation distance. This occurs due to the effective index of the fundamental vertical mode in the etched regions becoming larger than the effective index of all higher order vertical modes in the ridge. The investigation in (Soref, Schmidtchen &

Peterman 1991) utilized a propagation distance of 2mm to verify single-mode behavior with the beam propagation method.

Pogossian et al. suggested a value of c = -0.05 as a stricter condition for single-mode like waveguide behavior (Pogossian, Vescan & Vonsovici 1998) after an analysis using the effective index method. Figure 55 plots the critical aspect ratio versus rib height for a silicon-on-insulator rib waveguide at an operational wavelength of 1550nm. The region beneath each curve represents the combination of waveguide dimensions that ensures single-mode operation for a given polarization and r factor. It is clearly seen that for large rib heights the critical aspect ratio approaches an asymptote with r (and by extension the etch depth) becoming the dominant factor in determining which waveguide aspect ratios will enable single-mode operation.

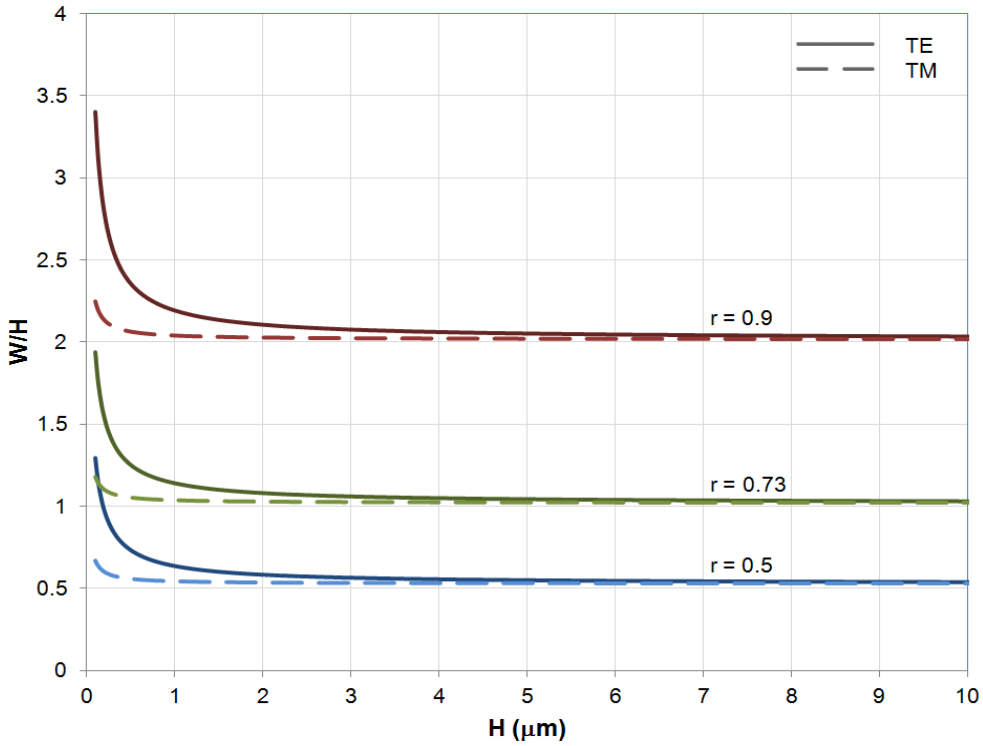

Figure 55 : Critical aspect ratio versus inner rib height for a silicon-on-insulator rib waveguide with air overcladding.

The Corning SMF-28 optical fiber used in this work has a nominal Gaussian mode field diameter of 10μm at a wavelength of 1.55μm (SMF-28e Optical Fiber Specification 2004). Keeping Equation 5.1 in mind, the central cross-section of the rib needs to be on the order of the optical fiber mode field diameter for efficient end-fire coupling without the use of tapered structures on either end (ie. lensed fibers or integrated tapers). Lensed fibers are avoided due to the size and fragility of the tip, which incurs additional expense for alignment, packaging and handling. Another consideration is the shape-induced birefringence discussed earlier. To a first order approximation, a symmetric waveguide cross-section results in the elimination of shape-induced birefringence by equalizing the TE and TM boundary conditions. Notable improvements have been reported by using this strategy (Pross, Tolksdorf & Dammann 1988; Sugimoto et al. 1996).

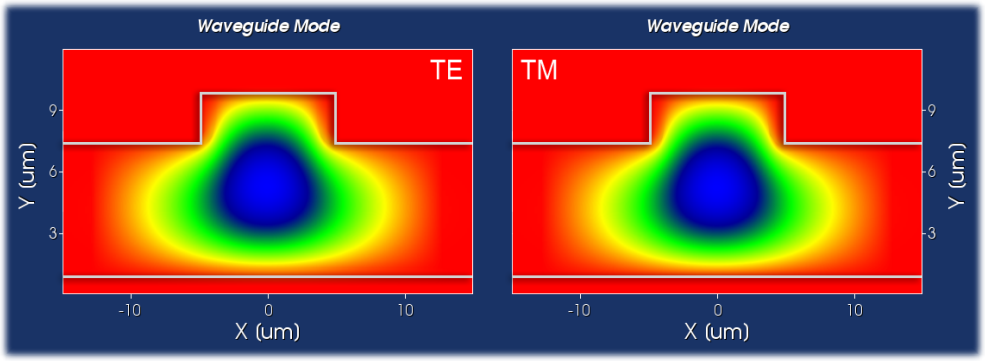

Figure 56 : Calculated fundamental mode profiles for designed silicon-on-insulator rib waveguide.

Values of H = 10μm and W/H = 1 were chosen. Using the dimensional relationship in Equation 5.2, single-mode operation is strictly guaranteed if r > 0.7241. Selecting r = 0.73 yields an etch depth of 2.7μm. The mode profiles (illustrated in Figure 56) were computed using FieldDesigner (Phoenix Software 2012), a commercial film mode matching (Sudbo

1993) solver. In addition to enabling more efficient coupling to SMF-28 fiber, selecting a large cross-section has the added benefit of greatly reducing shape-induced birefringence as shown in Figure 57 based on the calculated TE and TM modal indices.

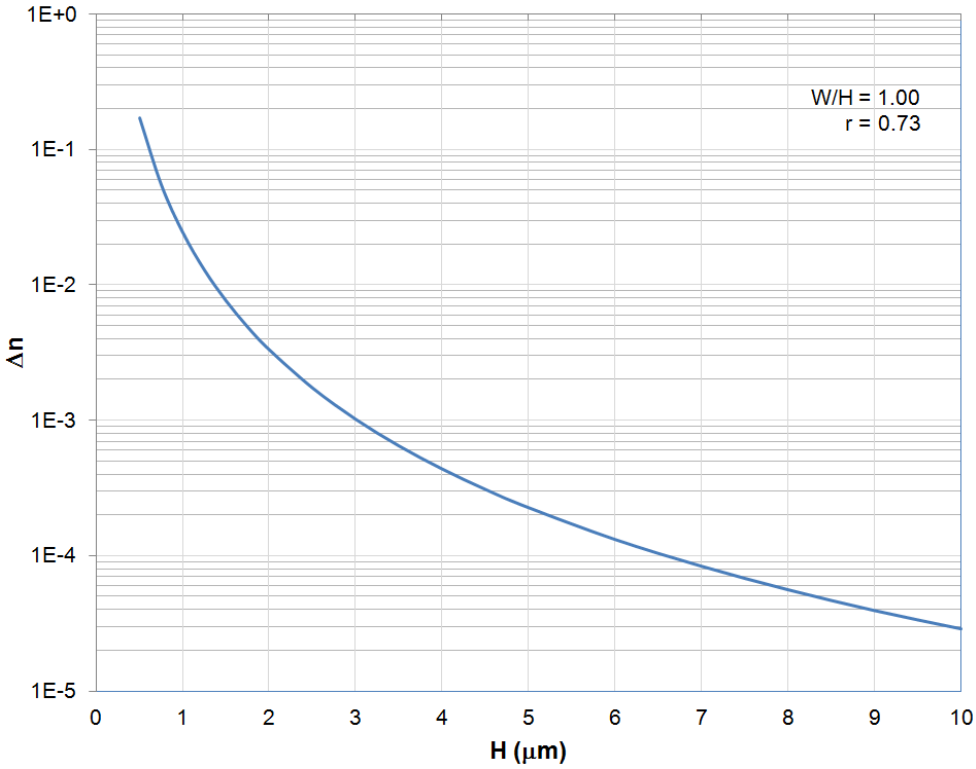

Figure 57 : Variation of the effective index birefringence with rib height for a silicon-on-insulator rib waveguide.

5.2.2 Coupler

With the waveguide structure now decided upon, attention is now turned to designing the 3dB couplers that are central components of the integrated Mach-Zehnder and Sagnac magneto-optic switches.

Section 3.1 provided the theoretical foundation for analyzing parallel waveguides. Recall that complete power transfer is achievable provided the phase match condition is met, which is the case here due to the use of identical waveguide cross-sections. This

nominally maximizes the achievable extinction ratio in the interferometers and ensures that they are not the limiting factors in the achievable switch extinction ratios.

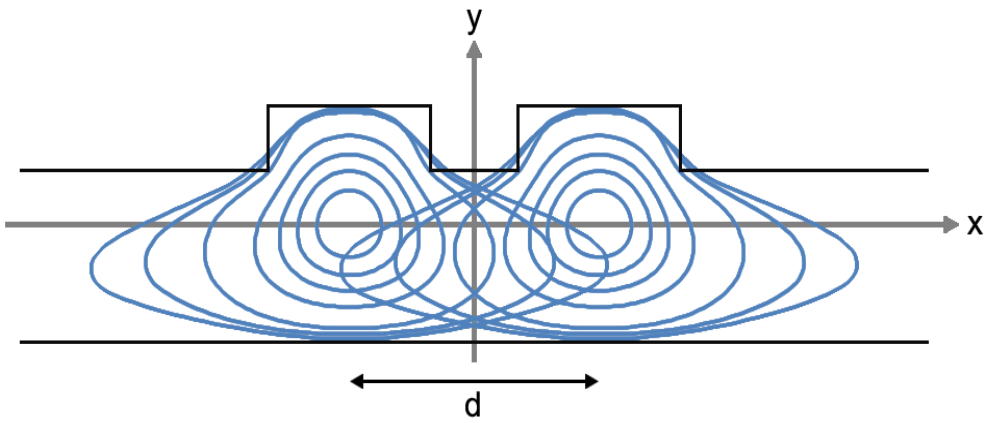

Figure 58 : Overlapped isolated mode contours of two parallel rib waveguides. The coupling between the waveguides is determined by calculating the overlap integral of the product of the mode profiles over the cross-section of either waveguide.

Since the propagation constants in both waveguides are identical, the coupling constant can be computed using Equation 3.16 and an overlap of the isolated rib waveguide mode profiles shown in Figure 58. While the integrals in Equation 3.16 can be evaluated analytically for some waveguide structures (eg. parallel slabs or optical fibers), the complicated geometry of rib waveguides necessitates a numerical solution. The mode contours were computed using a finite difference modesolver (Chiang, Chiou & Chang 2002). The overlap integral in Equation 3.16 was then numerically approximated with a summation to obtain the value of the coupling constant.

Figure 59 plots κ as a function of the center-to-center waveguide separation d. The linear slope of the curves is indicative of an exponentially decreasing relationship between κ and d. Furthermore the slopes of the TE and TM only differ slightly, which is expected from the reduced birefringence due to the relatively large waveguide cross-section dimensions.

A separation of 15μm was chosen to give a higher degree of fabrication tolerance while not severely impacting overall device length. This results in a π/4 coupling length of 3.5mm, which is subsequently verified using OptoDesigner (Phoenix Software 2012), a commercial paraxial beam propagation method solver as illustrated in Figure 60.

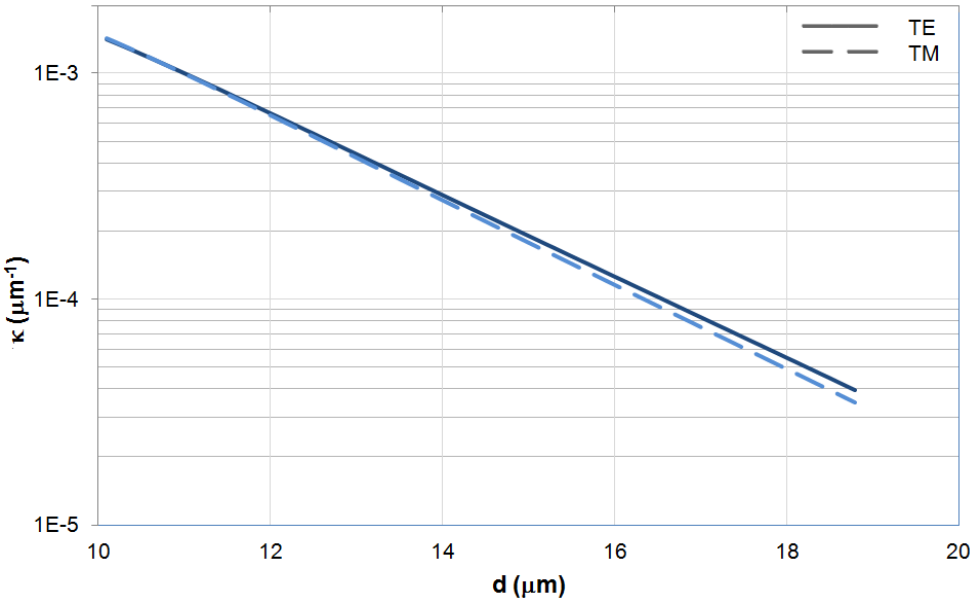

Figure 59 : Coupling constant κ as a function of center-to-center waveguide separation d for two parallel silicon-on-insulator rib waveguides.

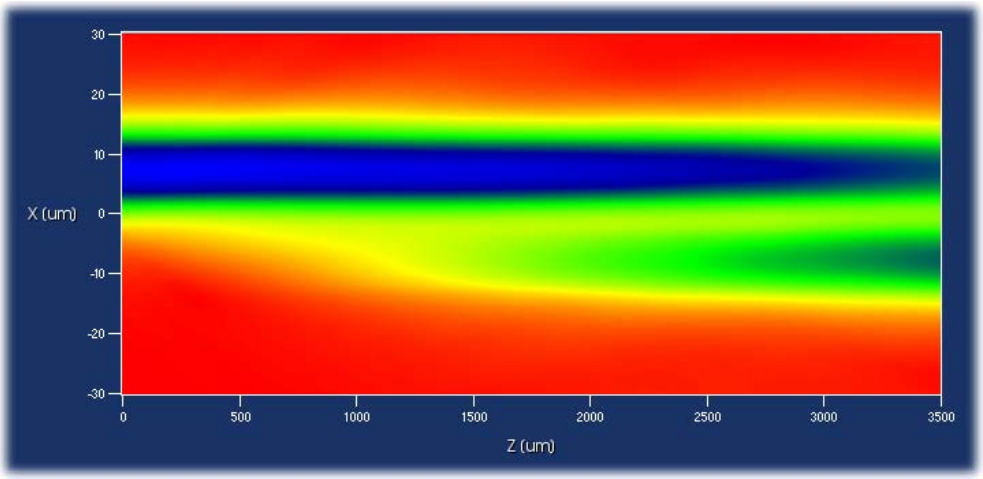

Figure 60 : Propagation profile for two parallel silicon-on-insulator rib waveguides.

5.2.3 Bends

The design of practical integrated optical devices requires that waveguides have differing separations at particular points (eg. to avoid unwanted coupling) and/or changes in direction of propagation. While this is usually facilitated using bends, most waveguides are not amenable to being bent at sharp angles without incurring a significant amount of loss due to the coupling of the guiding mode to radiation modes.

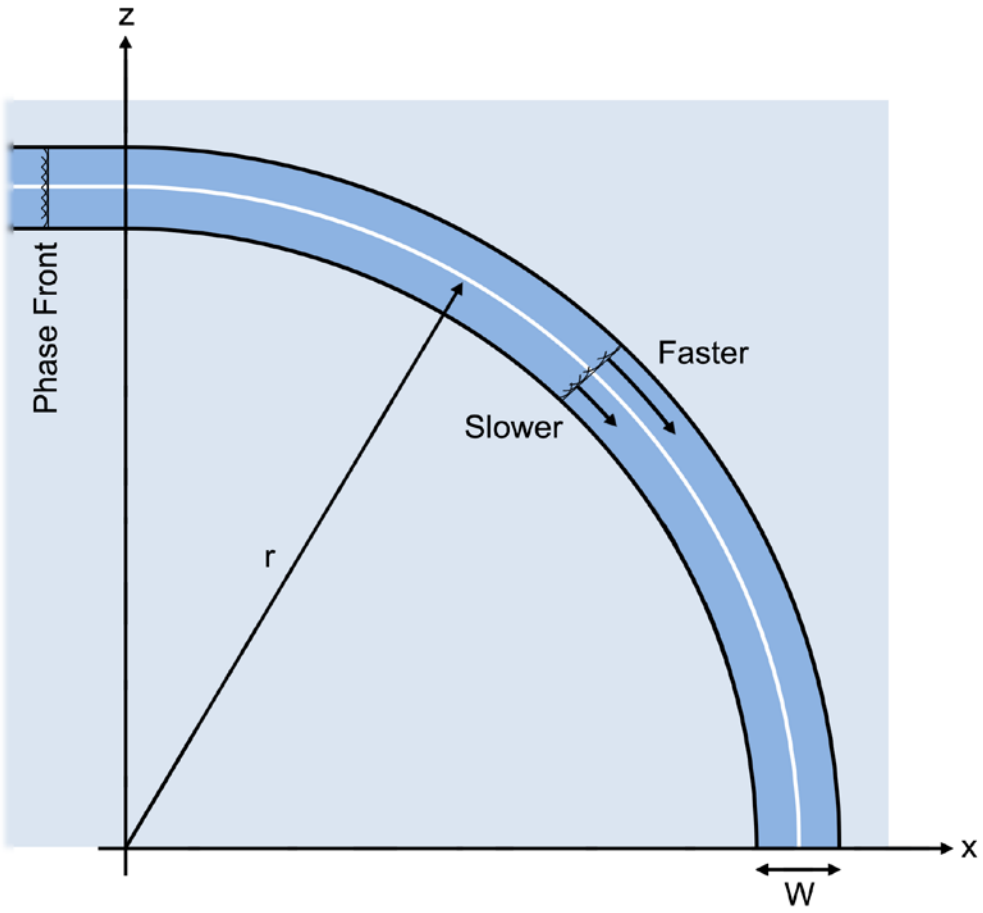

Figure 61 : Slab waveguide bent in the x-z plane that extends infinitely in the y direction.

The physical mechanism of coupling to radiation modes in bends can be understood by considering a curved waveguide section as shown in Figure 61. If a bend was sufficiently

gradual, it is fairly accurate to treat it as if it were a straight waveguide section. In the most extreme case however, when a waveguide is bent into a circular arc the wavefronts associated with the guiding mode are now pivoted about the center of curvature of the bend. As with the differential in an automobile, the phase front in the outer portion of the bend must travel slightly faster than the phase front in the inner portion to keep up with the propagating mode in the waveguide and maintain a constant phase relationship across the mode. At some critical radial distance, the phase velocity will exceed the local speed of light in the material. Since this is a physical impossibility, the field beyond this critical radius breaks away from the bound mode, entering a radiating mode and resulting in power loss (Marcuse 1972). The power loss is especially large for higher order modes and this is frequently utilized as an efficient method of filtering out unwanted modes in fibers. Some work has been reported (Luff et al. 2008) on integrated waveguides that use this effect to allow for deeper etch depths than predicted by Equation 5.2 for single-mode operation, increasing the effective index contrast and thereby reducing overall device size.

5.2.3.1 Radius of Curvature

The bent waveguide structure most amenable to analysis is the bent slab waveguide as illustrated in Figure 61, where the index of refraction is strictly a function of only x and z. The problem analysis involves solving the Helmholtz equation for the transverse electric field of the structure (Jackson 1998) :

$$\psi_{(x,z)}\left[\nabla_{xz}^2 + k^2 n_{(x,z)}^2\right] = 0 \tag{5.5}$$

The analysis is made more tractable by mapping the Cartesian variables x and z to a new pair of independent variables u and v by use of the conformal map :

$$u + iv = r \ln\left(\frac{x + iz}{r}\right) \tag{5.6}$$

Applying this conformal transformation (Heiblum & Harris 1975) transforms the curved waveguide into a straight waveguide with a continuously varying (rather than piecewise constant) refractive index profile as illustrated in Figure 62. This effectively reduces the two dimensional problem to a one dimensional problem since the index of refraction is only a function of u and independent of v as in Equation 5.7. The Helmholtz equation for the transverse electric field of the structure is now altered to the form in Equation 5.8.

$$n_{(u)} = n_{(x,z)} e^{\frac{u}{r}} \tag{5.7}$$

$$\psi_{(u)}\left[\frac{d^2}{du^2} + k^2 n_{(u)}^2 - \beta\right] = 0 \tag{5.8}$$

Since n(u) is an exponential function, it increases without bound to the right of the waveguide core region. This implies that the solutions to Equation 5.8 are oscillatory beyond a critical radial distance where n(u) > β/k (regions b and d in Figure 62) and decaying elsewhere (regions a and c in Figure 62). The solutions are described by a spectrum of eigenmodes since any value of β allows for a valid solution of ψ(u). However, there will be a value of β which produces a resonance spectrum with a Lorentzian profile. This is akin to a Fabry-Perot cavity with imperfect reflective facets where the resonance peaks have non-zero widths (Deck, Mirkov & Bagley 1998) as shown in Figure 63. The linewidths are related to the radius of curvature and describe the attenuation rate of the waveguide bend.

The mode spectrum method utilized in this work (Goyal, Gallawa & Ghatak 1987) approximates the transformed index profile n(u) as a series of piecewise linear functions as shown in Figure 64, resulting in solutions to the transformed Helmholtz equation that is described by Airy functions (Abramowitz & Stegun 1965).

The analysis of silicon-on-insulator rib waveguides first requires the application of the effective index method (Chiang 1994). As illustrated in Figure 65, the method first decomposes the rib waveguide cross-section into core and rib regions. Each region is then individually treated as an asymmetric slab waveguide to find its effective refractive index. The resulting effective indices (n_{eff1} and n_{eff2}) are in turn used to construct an equivalent three-layer slab waveguide, making the rib waveguide structure amenable to the preceding bending loss analysis.

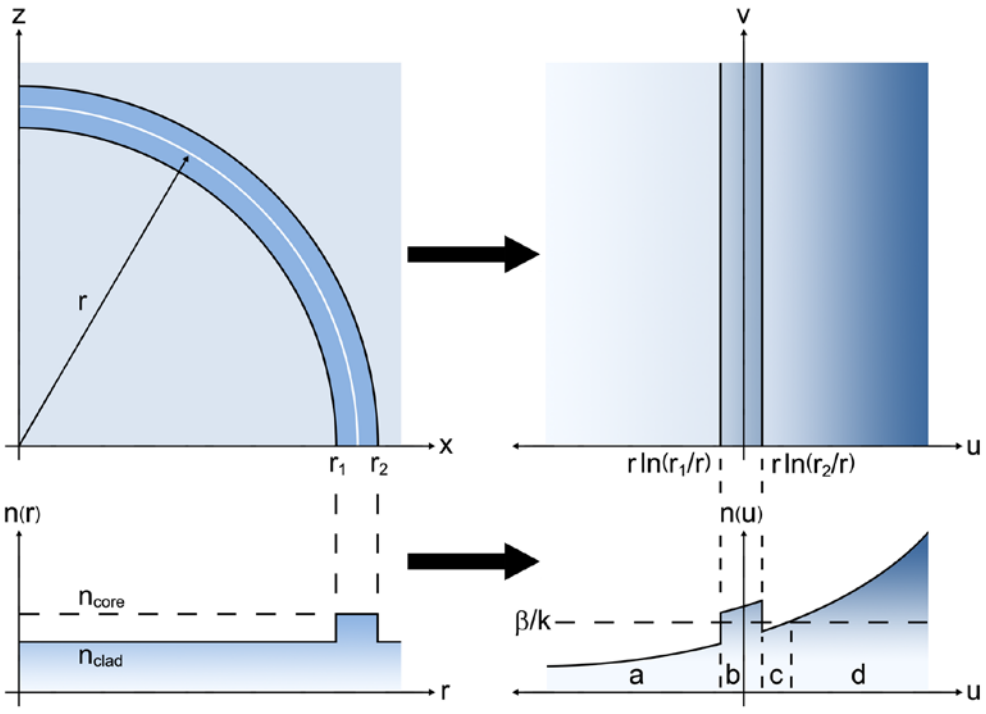

Figure 62 : Conformal mapping transformation of slab waveguide bent in the x-z plane to a straight waveguide in the u-v plane.

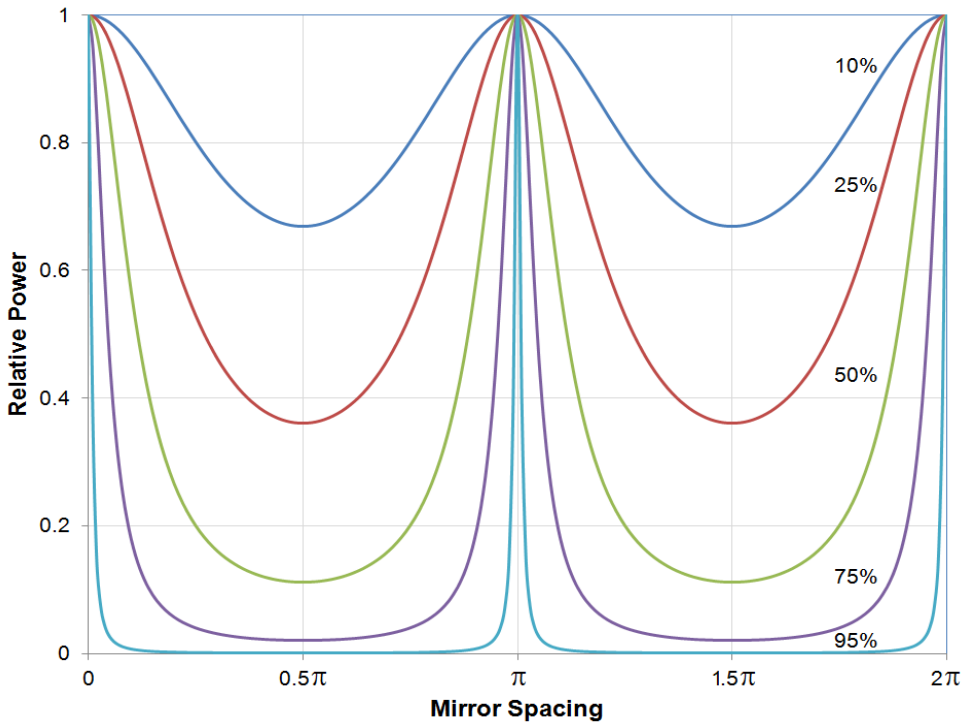

Figure 63 : Resonance spectra of an imperfect Fabry-Perot cavity for different mirror reflectivities.

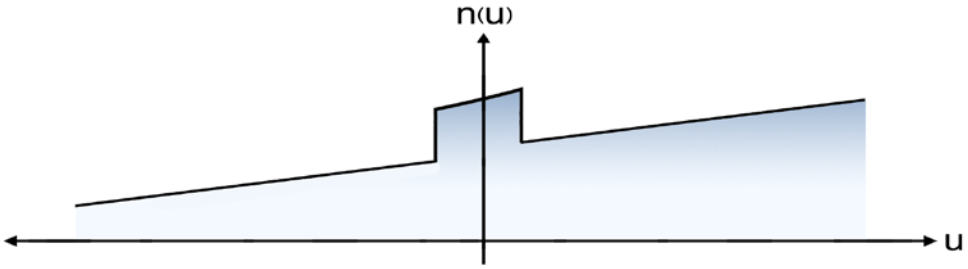

Figure 64 : Approximation of transformed index profile with three piecewise linear functions.

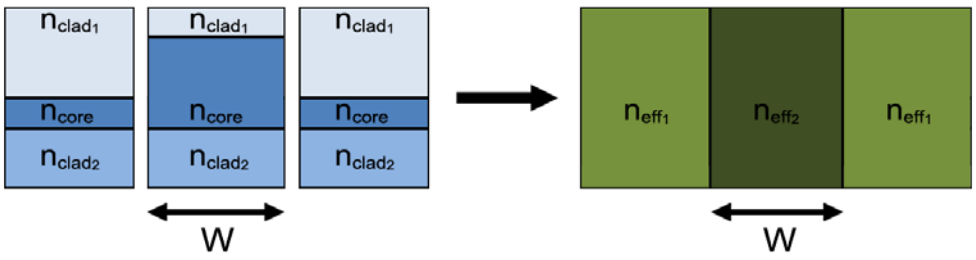

Figure 65 : Effective index method applied to a rib waveguide.

Figure 66 plots the bending loss as a function of the radius of curvature for the silicon-on-insulator rib waveguide geometry that is used in this work. The TE and TM loss curves are similar as expected and exhibit a characteristic elbow at which the loss rapidly decreases beyond a critical radius of curvature. A common radius of curvature of 223mm was selected that incurs a minimal bending loss of 0.25dB per 90° turn.

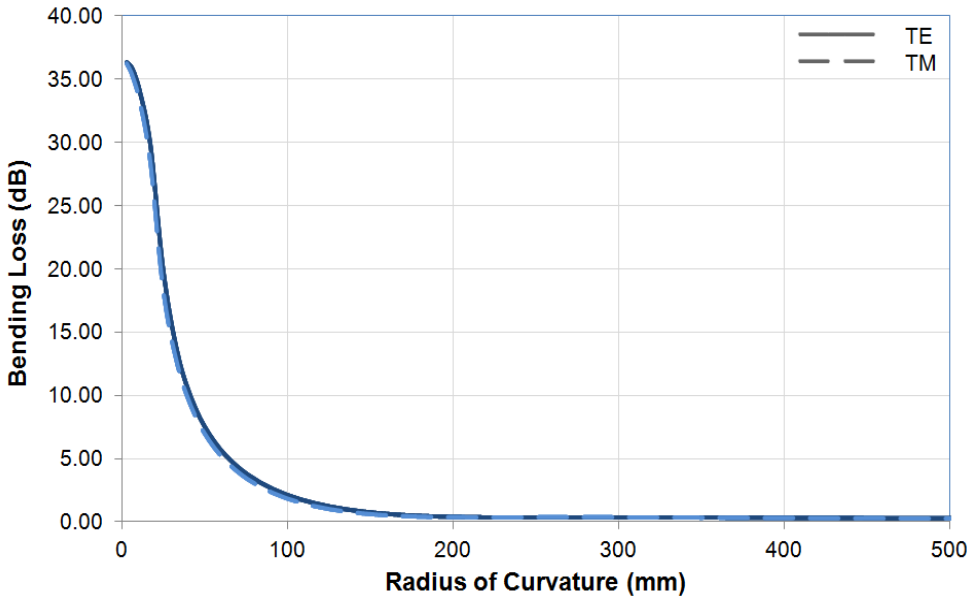

Figure 66 : Bending loss for a silicon-on-insulator rib waveguide as a function of the radius of curvature.

5.2.3.2 S-Bends

Thus far, the coupler has been designed without considering the gradual approach and separation of the waveguides at the coupler ports. Moreover, the integrated magneto-optic switches and test structures need to be interfaced to SMF-28 fibers. Recall from Figure 50 that although SMF-28 has a core size of only 9μm, the diameter of its cladding is 125μm. For this reason, commercially available V-groove fiber arrays have a nominal center-to-center separation of 250μm. This imposes the design constraint that the planar waveguides have to reach a separation of 250μm at the edges of the chip for the device to be compatible

with commercially available fiber mounts. An 8-channel array that is utilized for the measurements in Chapter 7 is illustrated in Figure 67.

S-bend transitions are utilized as they offer much lower losses compared to simple linear transitions. Figure 68 depicts a generalized waveguide S-bend. It is parameterized by a vertical separation Δd, bend radius r and bend angle θ.

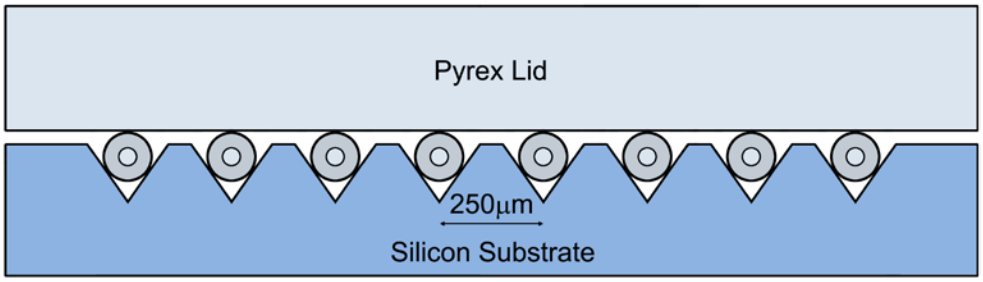

Figure 67 : Construction of an 8-channel silicon V-groove fiber array.

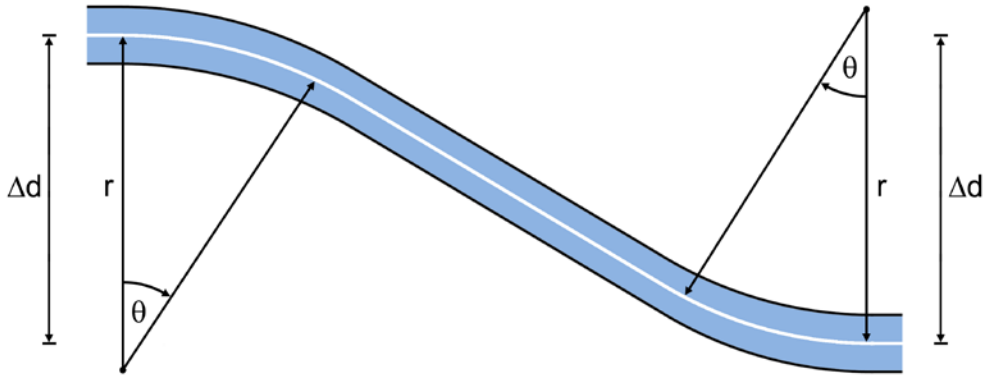

Figure 68 : S-bend waveguide segment characterized by a bend angle θ, radius of curvature r and total vertical displacement Δd.

For the designs in this work, r is fixed at 223mm to minimize bending losses. The coupler port separations are fixed at 60μm since the coupling constant κ is sufficiently low at this distance and enough space must be allowed for the bulk Faraday rotators to be inserted. This also minimizes the device length of the Mach-Zehnder magneto-optic switch

as two couplers need to be connected back to back. The 60μm separation and 223mm radius of curvature translates into a Δd of 22.5μm, θ of 1.8° and an S-bend length of 4.5mm. An additional S-bend is required to achieve the 250μm of separation at the chip edges. The remaining 190μm of separation coupled with the same 223mm radius of curvature translates into a Δd of 95μm, θ of 1.18° and an S-bend length of 9.2mm.

5.3 Design Implementation

The waveguide straights, bends and coupling sections are combined to form the 3dB couplers and subsequently the integrated Mach-Zehnder and Sagnac magneto-optic switches. As waveguide separate, coupling does not abruptly cease but slowly diminishes as the coupling constant κ decreases. The coupling section is thus foreshortened (Milton & Burns 1979) to account for the additional power transfer occurring in the curved S-bend regions. Figure 69 shows the simulated propagation profile of the 3dB coupler.

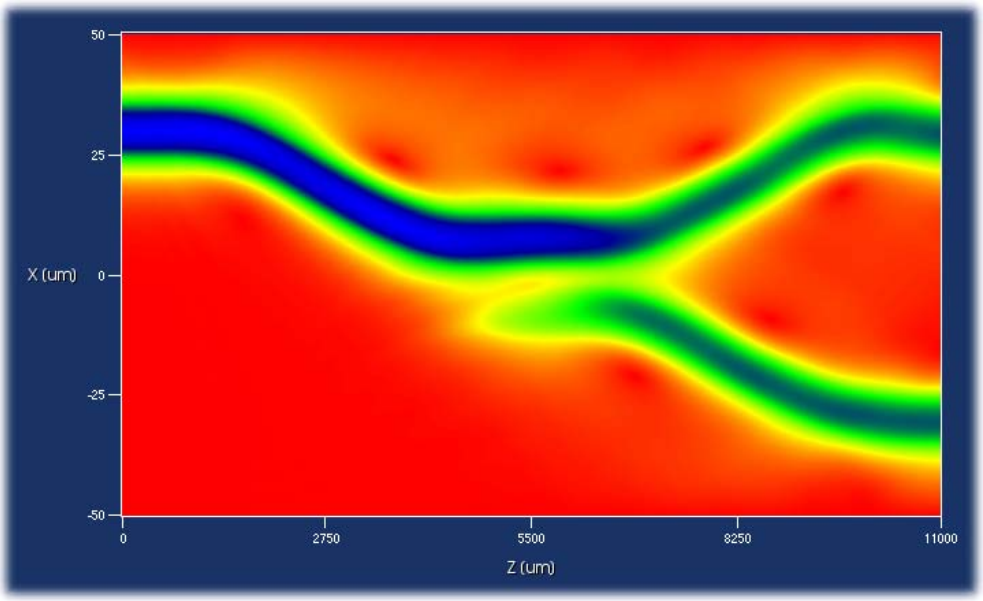

Figure 69 : Propagation profile for a silicon-on-insulator rib waveguide 3dB coupler.

Connecting two 3dB couplers in sequence forms the Mach-Zehnder interferometer core as shown in Figure 70. Finally, the addition of the outer S-bends to achieve the 250μm separation at the chip edges results in the complete integrated Mach-Zehnder magneto-optic switch. The simulated propagation profile and finalized dimensions are shown in Figure 71 and Figure 72 respectively.

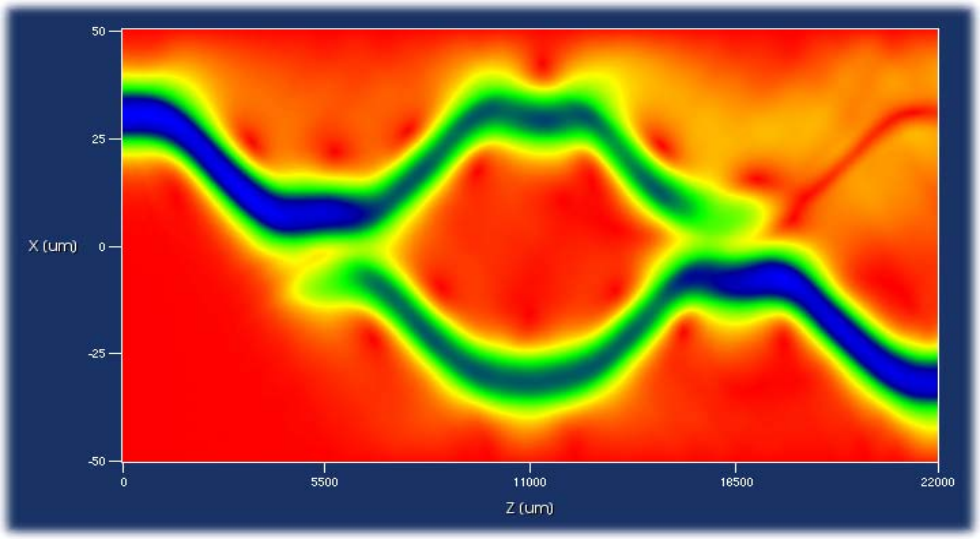

Figure 70 : Propagation profile for a silicon-on-insulator rib waveguide Mach-Zehnder interferometer.

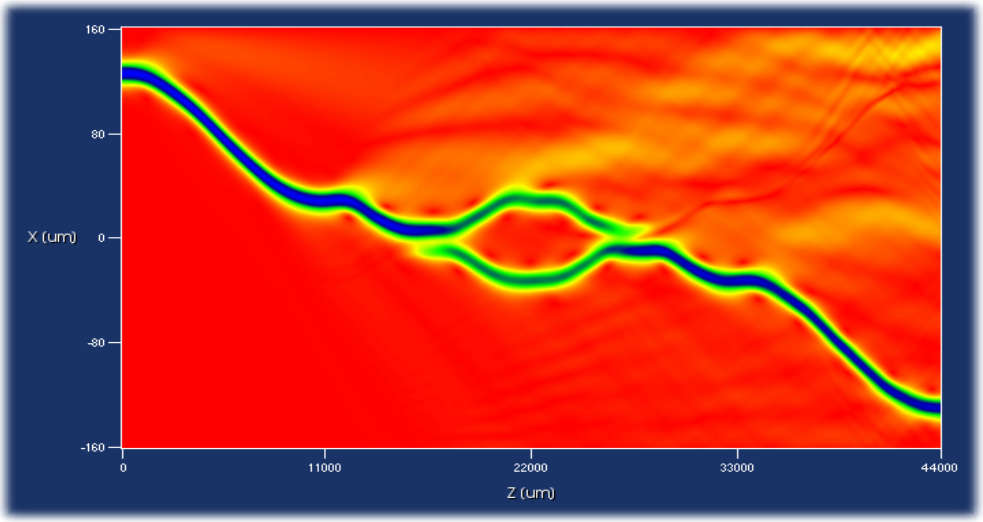

Figure 71 : Propagation profile for the integrated Mach-Zehnder magneto-optic switch.

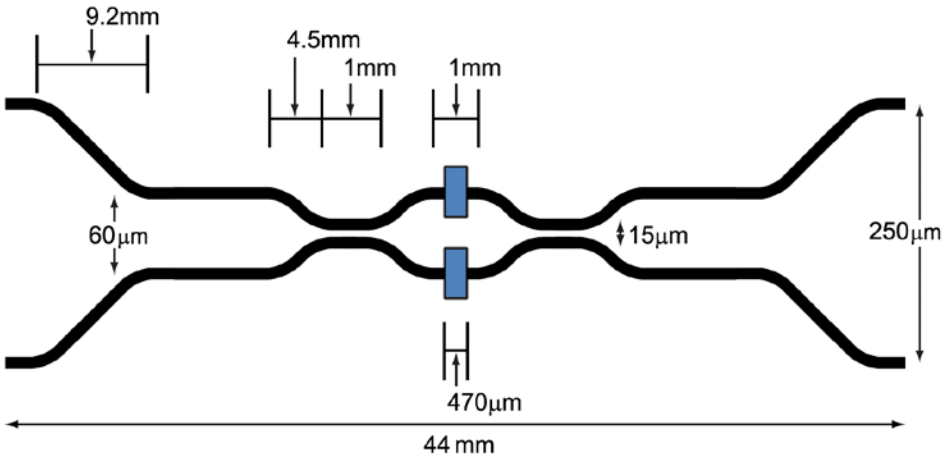

Figure 72 : Dimensions of the integrated Mach-Zehnder magneto-optic switch.

The commercial PhoeniX software suite (Phoenix Software 2012) used over the course of this work is unable to simulate the integrated Sagnac magneto-optic switch in its entirety. The OptoDesigner optical propagation simulator uses the beam propagation method (Feit & Fleck 1978), arguably the most widespread wave propagation technique capable of handling large (mm and cm scale) optical devices. It is a paraxial technique that only functions in cases where an optical axis is defined. This paraxiality limitation arises from the slowly varying envelope approximation made in computing the solution of the Helmholtz equation, which greatly increases algorithmic efficiency. An additional simplification (the removal of the second-order derivative in the Helmholtz equation with respect to z) eliminates the possibility of backward travelling wave solutions and thus looped structures such as the Sagnac interferometer cannot be simulated. The reader is referred to the appendices for the salient details regarding the beam propagation method.

An identical 3dB coupler and chip-edge transition S-bends are utilized for the integrated Sagnac magneto-optic switch. The overall chip size is constrained to be identical to that of the integrated Mach-Zehnder magneto-optic switch for ease of testing and

characterization. This leads to a loop S-bend transition with a 13.3mm radius of curvature and a 5mm Sagnac loop radius as shown in Figure 73.

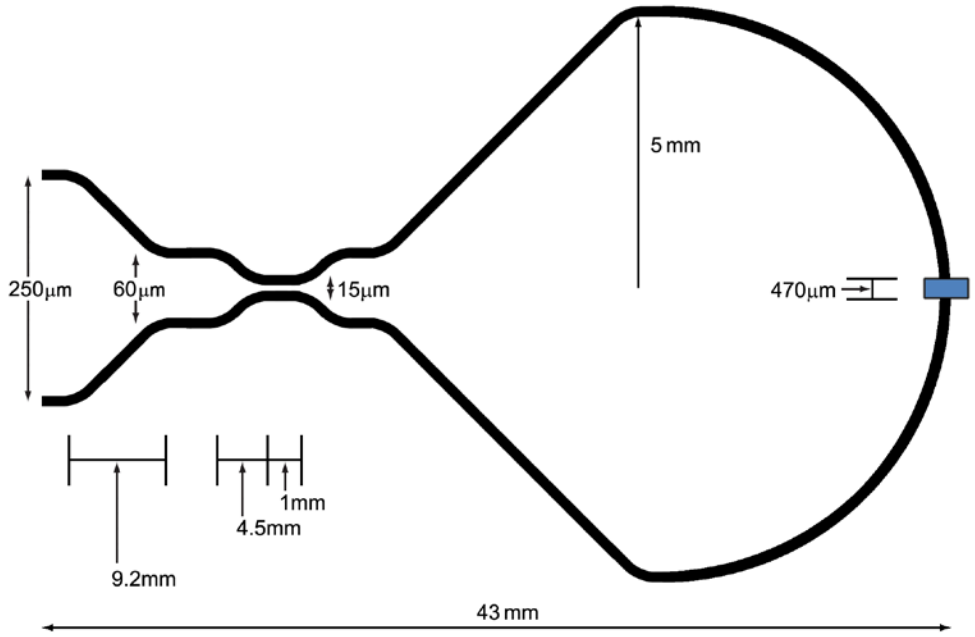

Figure 73 : Dimensions of the integrated Sagnac magneto-optic switch.

5.3.1 Fabrication Tolerance

The exact aspect ratio of the rib waveguide cross-section cannot be legislated due to inevitable imperfections in the fabrication process. The selection of a relatively large waveguide cross-section and separation in the coupling region aids in mitigating the effect of process defects. Figure 74 plots the computed coupling ratio achieved for waveguides that are uniformly wider or narrower, simulating the effect of unintentional feature size bias in the fabrication process. Note that the center-to-center waveguide separation was held constant while the waveguide widths were varied. For even the most extreme anticipated cases of feature bias (±1μm), the coupling ratio only changes by 2-3%.

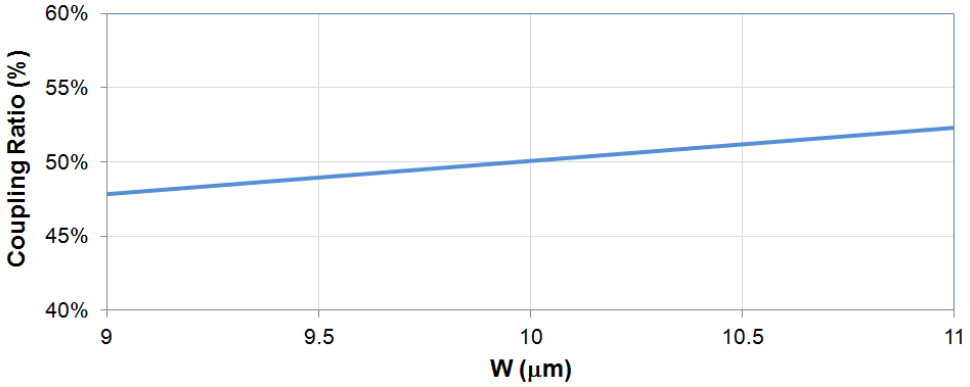

Figure 74 : Performance of the designed silicon-on-insulator rib waveguide 3dB coupler when the waveguide width is biased above and below its nominal value of 10μm.

5.3.2 Test Structures

In addition to the actual integrated magneto-optic switches, several test structures are included in the optical chips for characterization purposes. Their simulated propagation profiles are shown below.

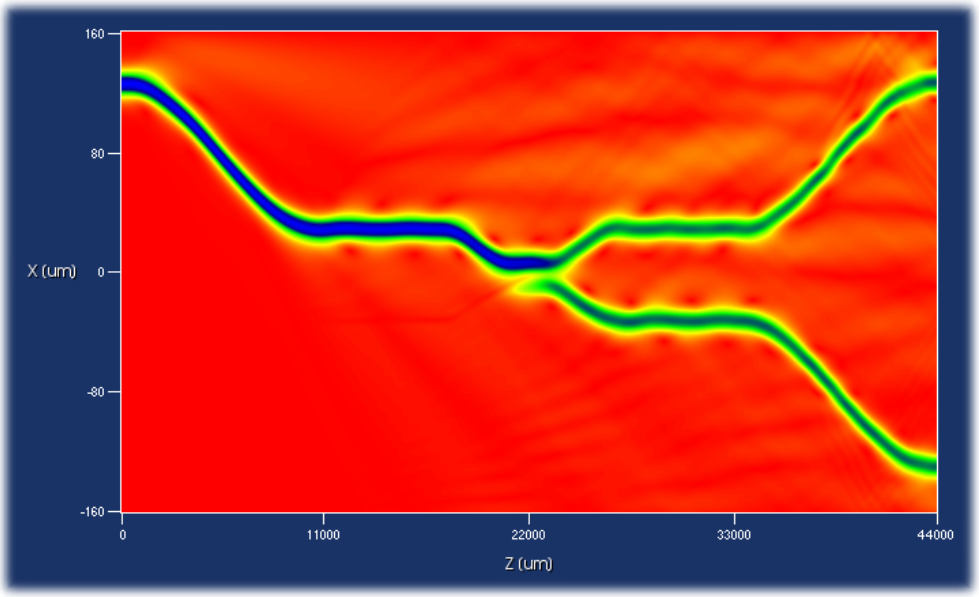

Figure 75 : Propagation profile of 3dB coupler test structure.

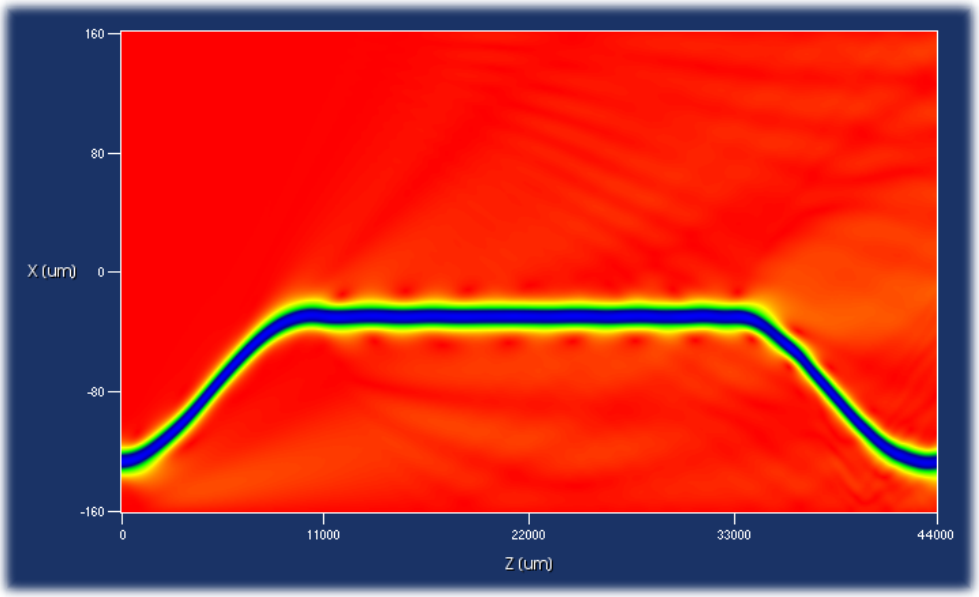

Figure 76 : Propagation profile of S-bend test structure.

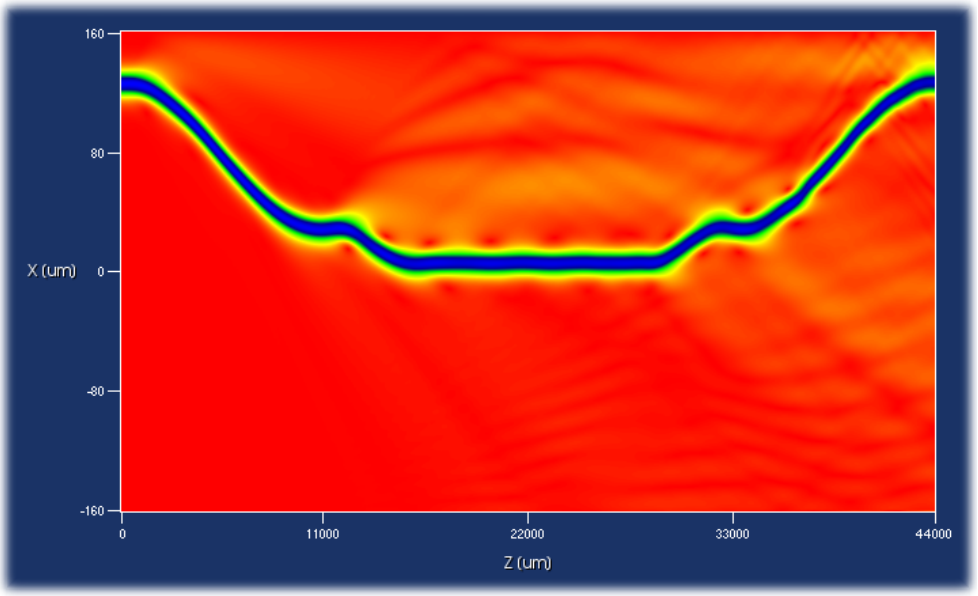

Figure 77 : Propagation profile of double S-bend test structure.

5.4 Nanophotonic Switches

As alluded to earlier, the high refractive index contrast in a silicon-on-insulator material system enables the tight confinement of light in a core region with sub-μm dimensions. Waveguides with such a core are classified as nanophotonic structures and they allow for a dramatic reduction in footprint, in turn enabling larger-scale integration of photonic components. However, birefringence becomes a severe problem in nanophotonic waveguides due to the higher effective index contrasts achieved with smaller dimensions as illustrated in Figure 57 for silicon-on-insulator rib waveguides. This can be addressed by either using a polarization diversity scheme or careful engineering of the waveguide geometry. The latter approach is adopted in this work.

Nanophotonic versions of the integrated Mach-Zehnder and Sagnac magneto-optic switches are proposed below. The results of full-vectorial beam propagation and finite-element analyses from (Chan et al. 2005) is utilized to derive the following dimensional relationships to ensure single-mode and polarization-independent operation :

$$\frac{W}{H} = 0.05 + \frac{(0.94 + 0.25H)r}{\sqrt{1-r^2}} \tag{5.9}$$

$$0.3 \le r \le 0.5, \quad 1.0\mu m \le H \le 1.5\mu m$$

$$D_{\min} = 0.06 + 0.556H \tag{5.10}$$

where the dimensional parameters are defined with respect to Figure 54. The range of waveguide geometries that exhibit both single-mode and polarization-independent behavior for various rib heights are plotted in Figure 78.

Values of H = 1.5μm, W = 0.92μm and D = 0.9μm were chosen. The mode profile was computed in FieldDesigner and illustrated in Figure 79.

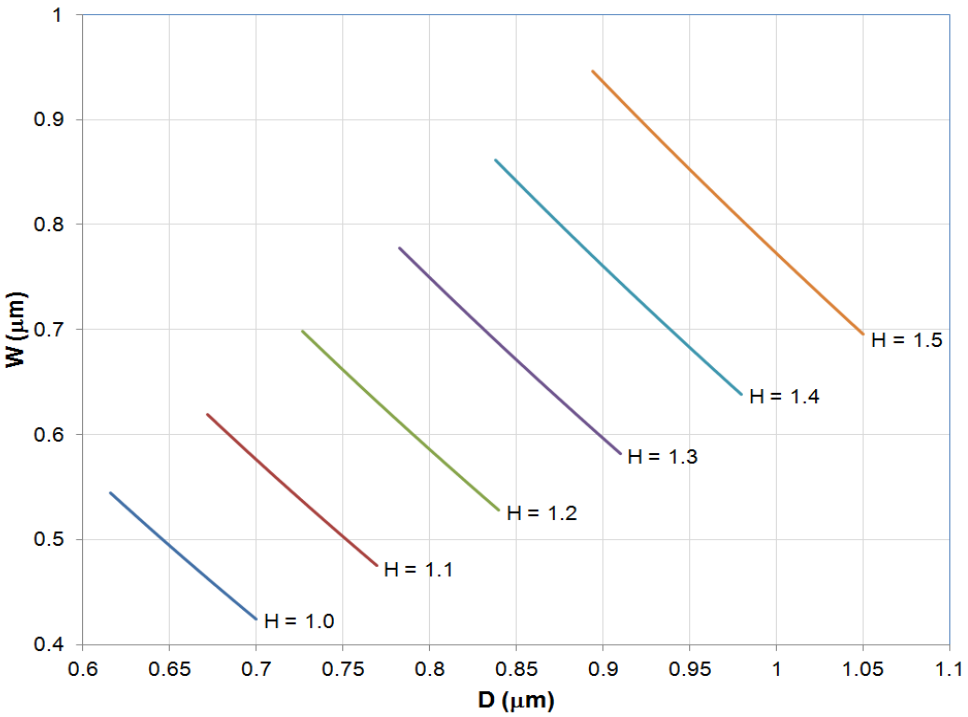

Figure 78 : Rib width versus etch depth for zero birefringence, single-mode silicon-on-insulator rib waveguides with air overcladdings and different heights.

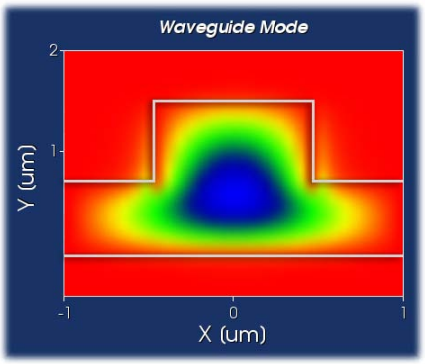

Figure 79 : Calculated fundamental mode profile for designed nanophotonic silicon-on-insulator rib waveguide.

Using the same method applied earlier to the microphotonic rib waveguide, the coupling constant κ was calculated for a range of center-to-center waveguide separations and plotted in Figure 80, where an exponentially decreasing relationship between κ and d is seen as expected. A separation of 1.92μm was chosen to impart some degree of fabrication

tolerance while having a negligible impact on overall device length. This gives a $\pi/4$ coupling length of 182μm, which is verified using OptoDesigner as shown in Figure 81.

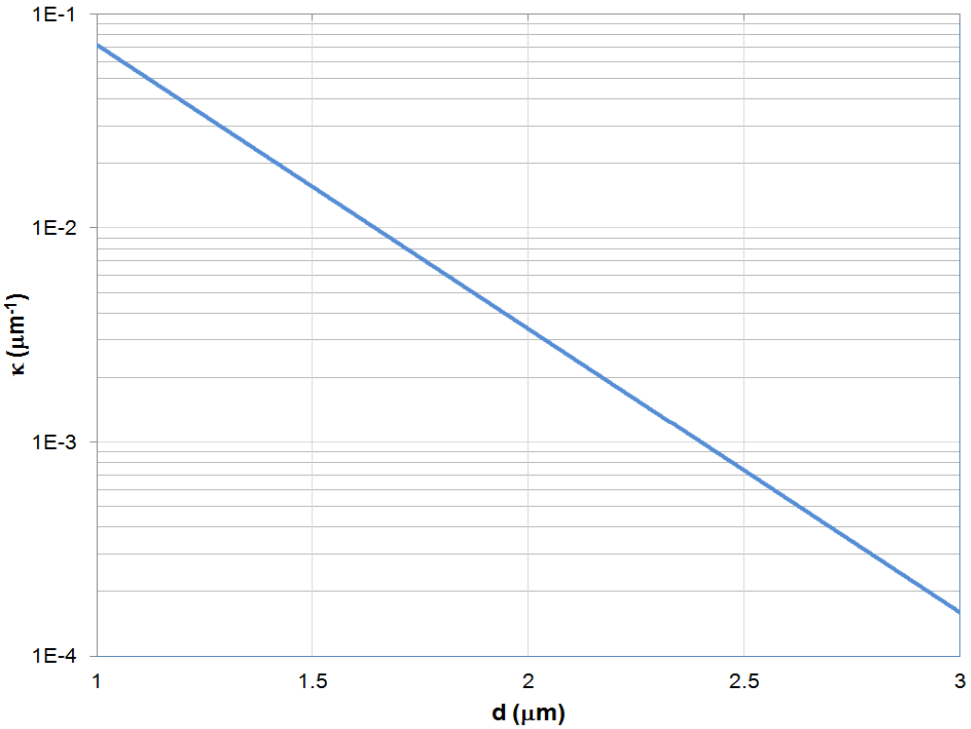

Figure 80 : Coupling constant κ as a function of center-to-center waveguide separation d for two parallel nanophotonic silicon-on-insulator rib waveguides.

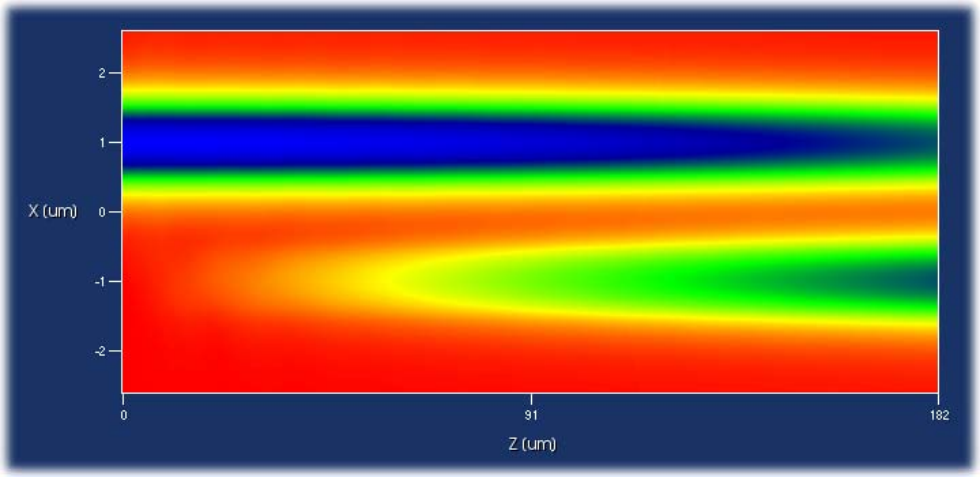

Figure 81 : Propagation profile for two parallel nanophotonic silicon-on-insulator rib waveguides.

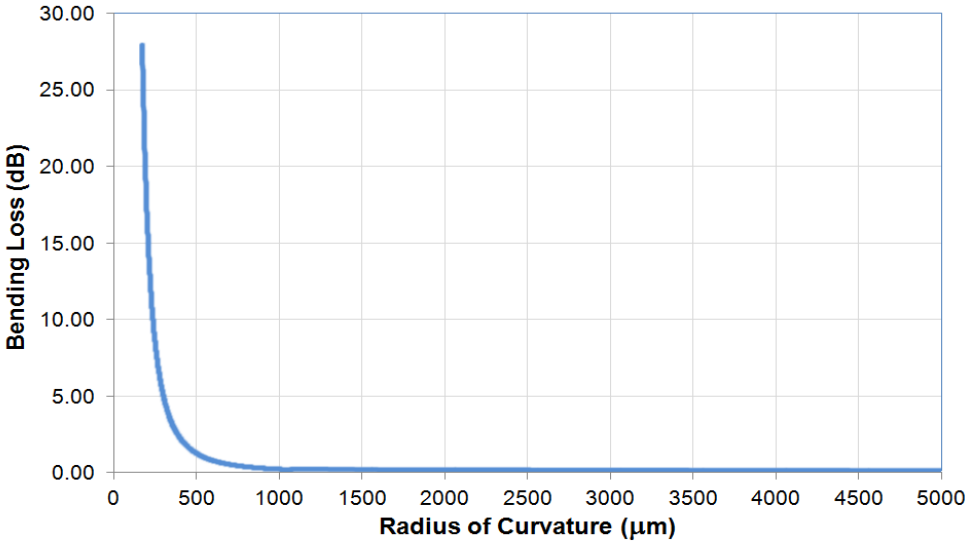

Figure 82 : Bending loss for a nanophotonic silicon-on-insulator rib waveguide as a function of the radius of curvature.

Figure 82 plots the bending loss as a function of the radius of curvature for the nanophotonic silicon-on-insulator rib waveguide geometry as calculated using the mode spectrum method described earlier. A conservative common radius of curvature of 1.8mm was selected that incurs a minimal bending loss of 0.22dB per 90° turn.

A single S-bend (rather than two staggered S-bends) with a vertical separation of 124.04μm, θ of 7.61° and length of 929μm is utilized for the nanophotonic 3dB couplers. An exception is made for the Sagnac loop S-bend transition, where a minimum radius of curvature of 2.9mm (and corresponding length of 4mm) is required to maintain $\theta \leq 45°$.

The various nanophotonic waveguide components are combined to from the nanophotonic Mach-Zehnder and Sagnac magneto-optic switches. The coupling section in the 3dB couplers were foreshortened by 40μm due to additional power transfer from the curved S-bend regions. The finalized dimensions are shown in Figures 83 – 84 and the simulated propagation profiles are shown in Figures 85 – 88. Due to the paraxiality limitation, the nanophotonic Sagnac switch was unable to be simulated in its entirety.

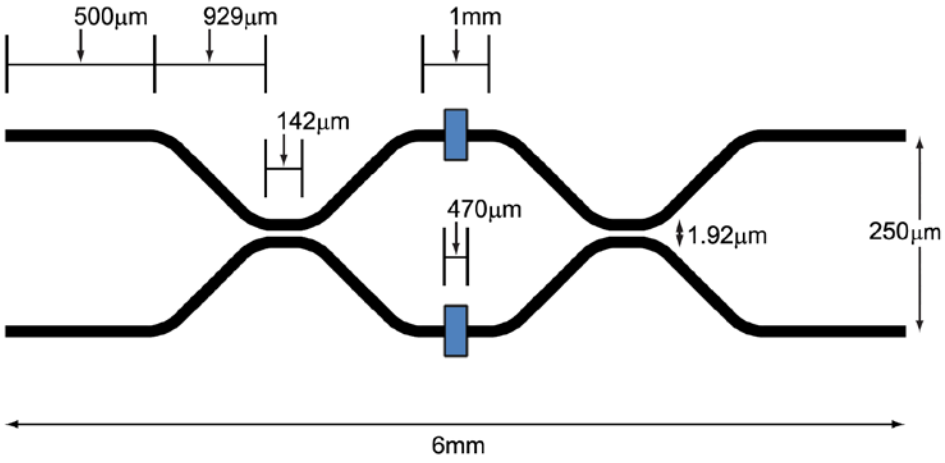

Figure 83 : Dimensions of the nanophotonic Mach-Zehnder magneto-optic switch.

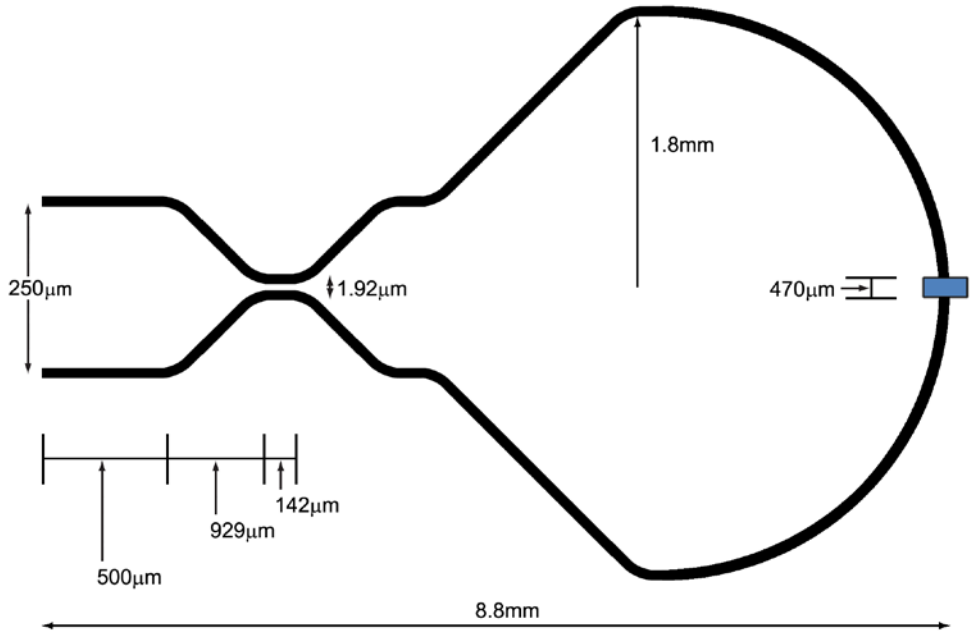

Figure 84 : Dimensions of the nanophotonic Sagnac magneto-optic switch.

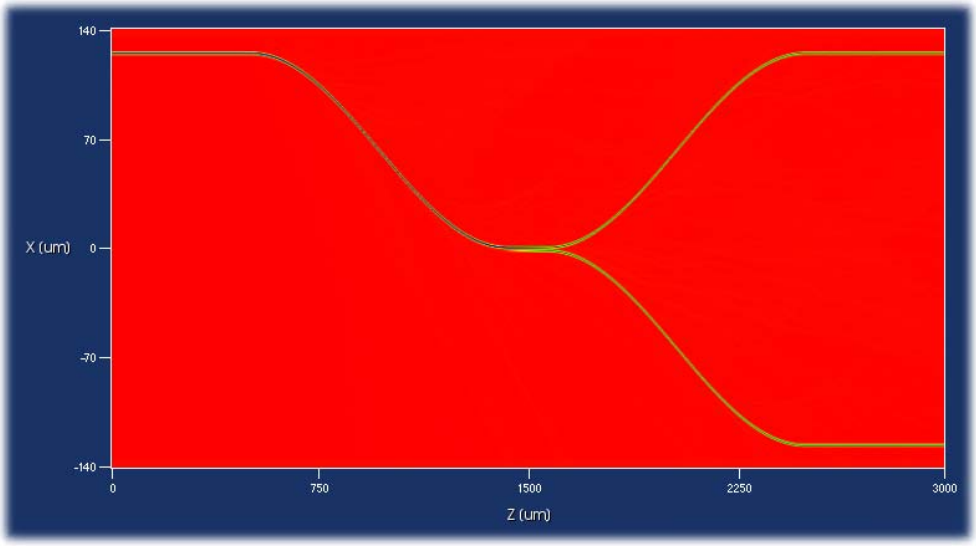

Figure 85 : Propagation profile for a nanophotonic silicon-on-insulator rib waveguide 3dB coupler.

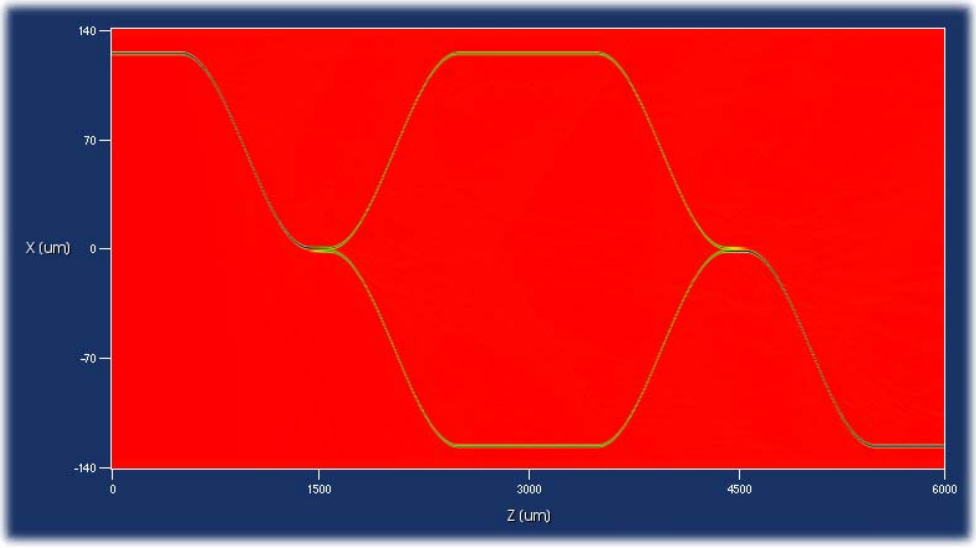

Figure 86 : Propagation profile for the nanophotonic Mach-Zehnder magneto-optic switch.

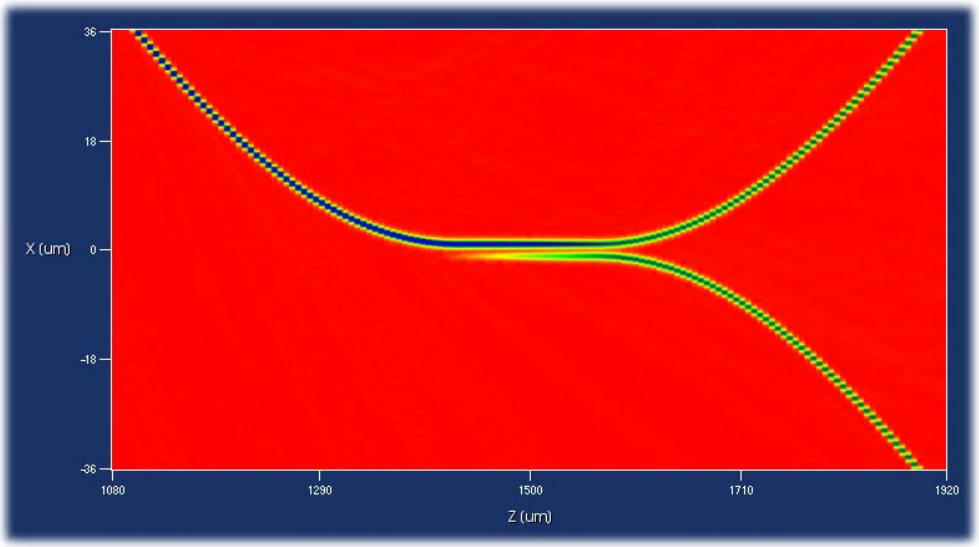

Figure 87 : Magnified propagation profile for the nanophotonic Mach-Zehnder magneto-optic switch (first 3dB coupler).

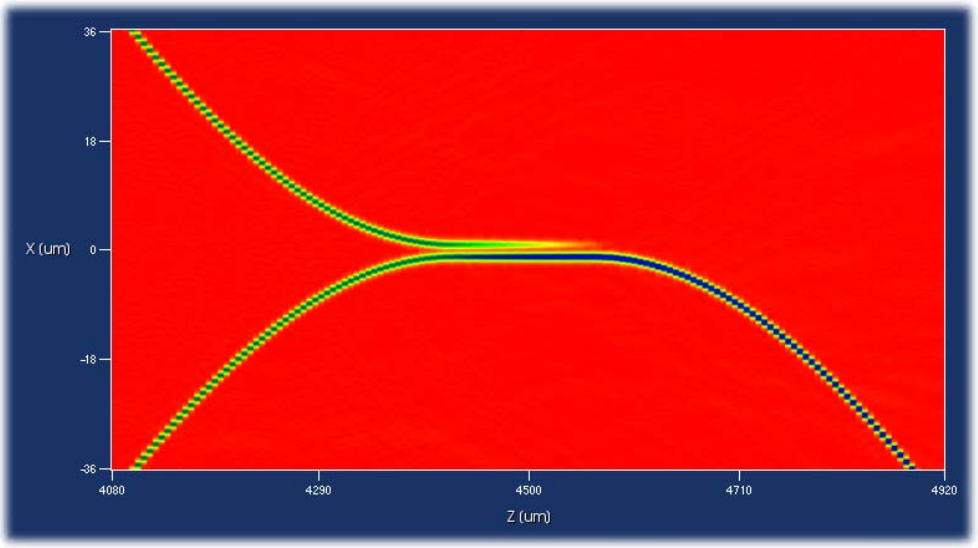

Figure 88 : Magnified propagation profile for the nanophotonic Mach-Zehnder magneto-optic switch (second 3dB coupler).

Figure 89 plots the computed coupling ratio achieved for nanophotonic waveguides that are uniformly wider or narrower, simulating the effect of unintentional feature size bias during fabrication. The waveguide widths were varied while the center-to-center waveguide separation was held constant. The nanophotonic couplers are more sensitive to geometry aberrations than their microphotonic counterparts with the coupling ratio varying by 5-6% for a ±0.1μm change in waveguide width.

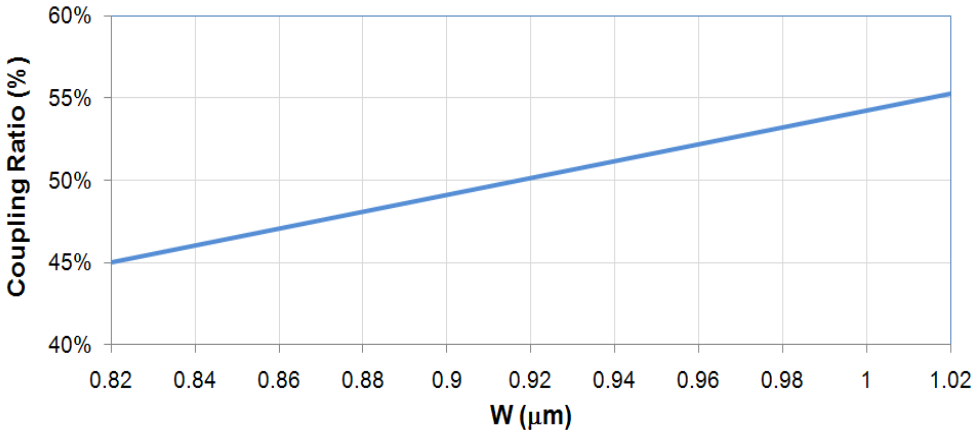

Figure 89 : Performance of the designed nanophotonic silicon-on-insulator rib waveguide 3dB coupler when the waveguide width is biased above and below its nominal value of 0.92μm.

A more pressing fabrication tolerance concern is the stability of the polarization-independent waveguide operation. Figure 90 shows the dependence of the geometrical birefringence on etch depth. A change in etch depth of ±10nm results in a change in Δn of approximately 1.2×10^{-3}, emphasizing the importance of accurate dimensional control when fabricating nanophotonic waveguides.

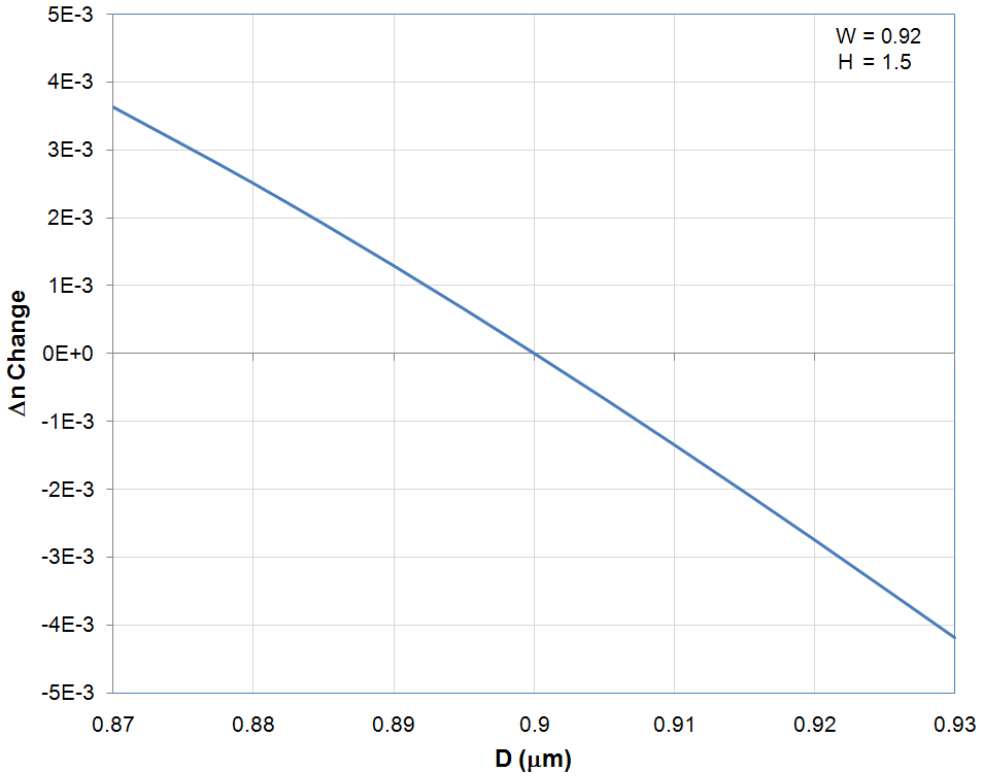

Figure 90 : Sensitivity of birefringence to etch depth for the designed nanophotonic silicon-on-insulator rib waveguides.

CHAPTER 6. INTEGRATED SWITCH FABRICATION

Thus far, a great amount of attention has been devoted to the theory and design of the optical waveguiding structures that comprise the integrated Mach-Zehnder and Sagnac magneto-optic switches. While certainly important, if the designs are unable to be physically realized at the necessary specifications, the quality of the designs becomes irrelevant. Consequently, the focus is now shifted from theory to practice and the silicon-on-insulator rib waveguide fabrication techniques and considerations are scrutinized.

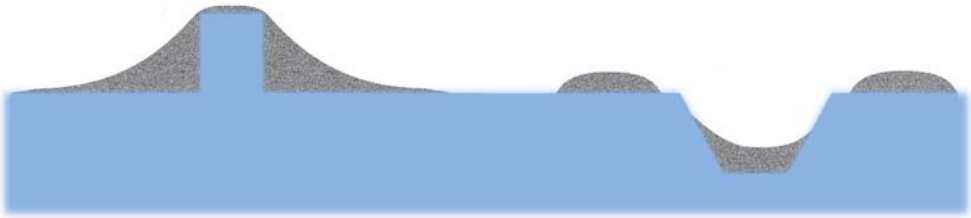

Figure 91 : Uneven resist coverage after spin coating, which complicates the lithography of optical structures.

Compatibility with standard microelectronics processing techniques is often cited by many optics research groups. However, the fabrication of integrated optical devices presents certain distinctive challenges. For instance, the etch depths involved in defining optical waveguide structures range from 0.1μm – 6μm in contrast with the typical etch depths involved in CMOS processing (100nm – 300nm). Coupled with the lower feature density inherent in optical designs, non-uniform resist coating becomes an issue as illustrated in Figure 91. Spin coating is governed by several physical phenomena including spin dynamics, solvent transport and resist rheology (Curtis et al. 2002), which result in the spun-on film beginning to cover in a conformal manner rather than planarizing. This is highly

detrimental to established nanolithographic techniques that rely upon a planar substrate, for instance to pattern fine-period Bragg gratings over relatively tall waveguides.

An additional concern is the limitation imposed by the depth of focus of the lithography tool. The higher aspect ratios required for the deeper etches demand either a masking material that offers an adequately high etch selectivity or a sufficient increase in the masking layer thickness. The depth of focus limits both the maximum thickness of the masking layer as well as the maximum tolerable non-planarity of the substrate. Optical lithography tools are able to trade resolution for depth of focus but are fundamentally bound by the diffraction limit. Thus electron-beam lithography tools are frequently utilized to pattern optical structures (as is the case in this work) since they offer a much greater depth of focus and are only limited by electron scattering.

The various optical structures to be fabricated are summarized in Figures 92 – 93, where the scale of some features has been exaggerated in order to better illustrate the devices. All the waveguides have a center-to-center separation at the chip facets of 250μm and the minimum separation between adjacent devices is 220μm. The test structures included in the first chip allow for the verification of the coupler splitting ratio as well as the characterization of propagation losses (straight waveguides) and bending losses (second and seventh waveguides). Both chips are constrained to have the same length after die-sawing for ease of testing.

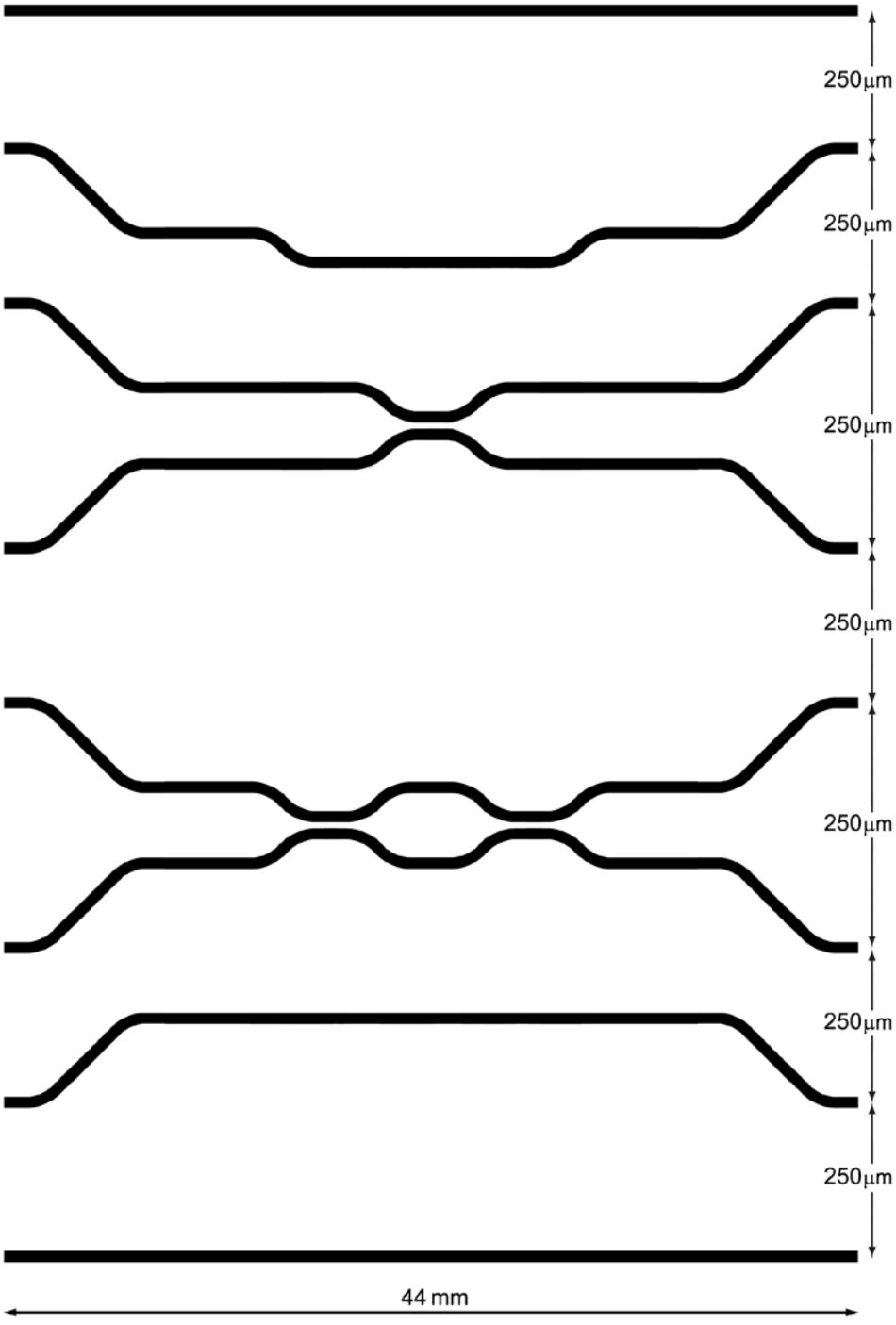

Figure 92 : Integrated Mach-Zehnder magneto-optic switch chip layout with test structures included (not to scale).

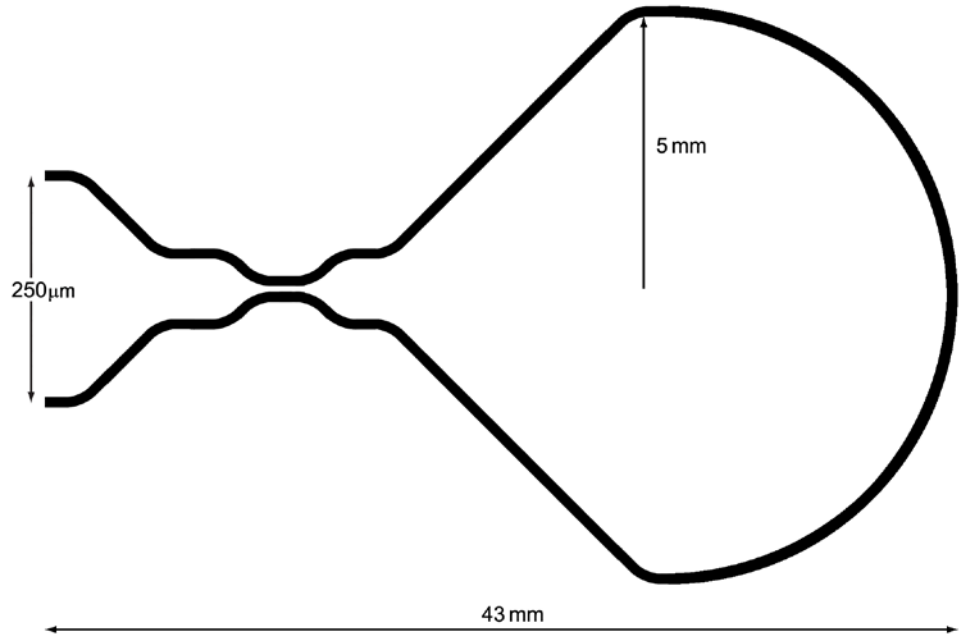

Figure 93 : Integrated Sagnac magneto-optic switch chip layout (not to scale).

6.1 Process

Fabricating rib waveguides in a silicon-on-insulator material system is a reasonably straightforward process, especially when compared to channel waveguides. Material overgrowth is not an issue since no top cladding layer is required and the etch depth involved (2.7μm) is not prohibitively deep as to cause complications with masking layer thickness or etch selectivity. Moreover, the chemistries and recipes for etching silicon are well established in the semiconductor industry.

The starting point of the waveguide fabrication process is the selection or creation of a silicon-on-insulator wafer. Commercially available bonded and etched-back (BESOI) wafers (IceMOS Technology Ltd. 2012) were utilized in this work. They were produced using the fabrication sequence illustrated in Figure 94. The process begins with a <110> primary flat silicon wafer, grinding it flat and polishing its surface to better planarize it and remove

any surface damage. This is followed by either a wet or dry oxidation step. The device silicon layer is then bonded to the handle wafer, followed by a high temperature anneal to form a stable bond. Finally, the device silicon layer is ground to the desired thickness and polished. For the devices reported in this work, the oxide thickness is 5000Å and the device silicon thickness is 10μm.

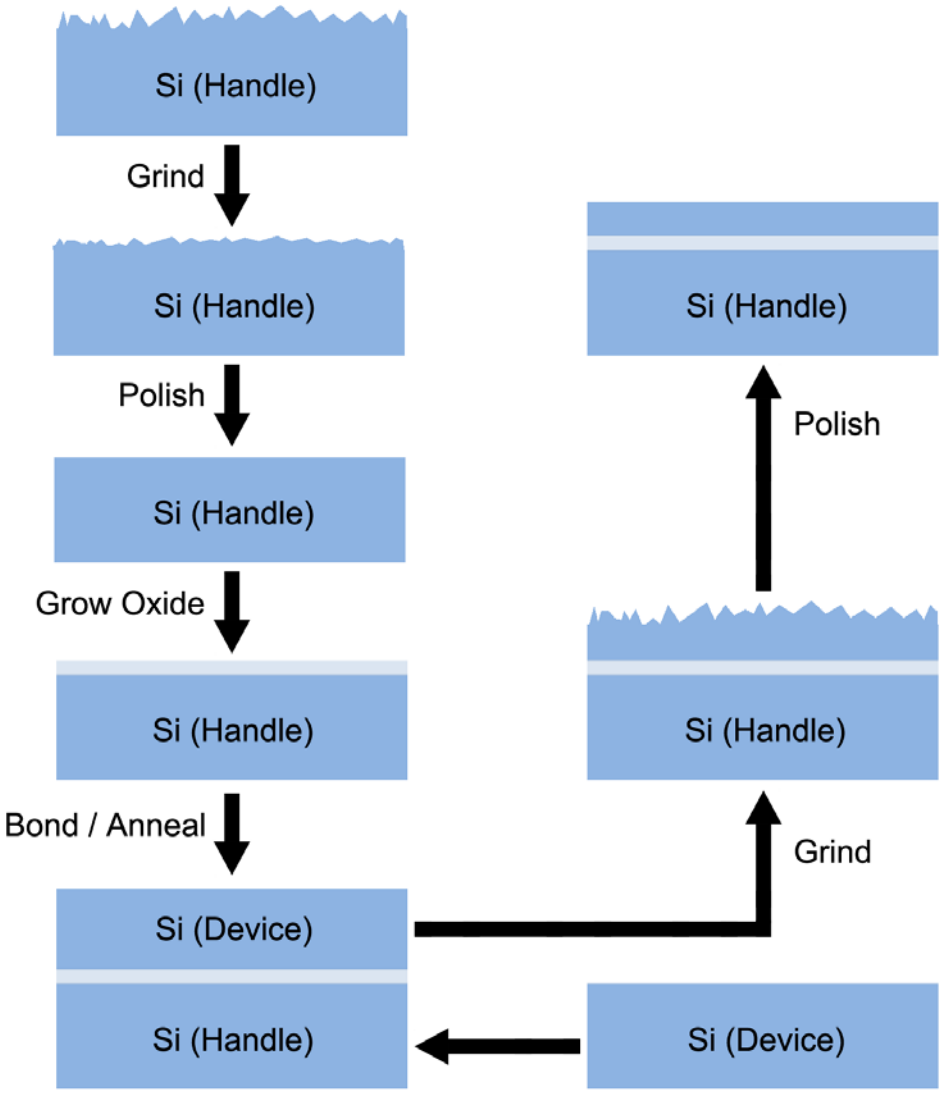

Figure 94 : Process used by IceMOS to produce bonded and etched-back silicon-on-insulator wafers.

Figures 95 and 96 outline the process steps used to pattern the silicon-on-insulator rib waveguides that comprise the proposed integrated Mach-Zehnder and Sagnac magneto-optic switches. First, a layer of hexamethyldisiloxane (HMDS) was spin coated on top of the device silicon layer to promote adhesion between the silicon and resist. A 350nm thick layer of hydrogen silsesquioxane (HSQ) was then deposited by spin coating and soft baked.

As this is the first time that this type of fabrication is being performed in this research group, optical photomasks with couplers and waveguides were unavailable. Thus the integrated switches and test structures were patterned by scanning electron-beam lithography via the use of a Raith 150 system (Figure 97). The waveguide structures were written with a voltage of 20keV, beam current of 1nA, areal dose of 190$\mu C/cm^2$, pixel size of 20nm and write field size of 100µm. A short postbake was performed after developing the HSQ in a tetramethylammonium hydroxide (TMAH) based developer (Microposit CD-26) for 300s.

After resist development, the waveguides were etched in a STS Model 320 reactive-ion etching system (Figure 98) using the patterned HSQ as a mask. The etching parameters were 25sccm of SF_6 and 4sccm of O_2 at an RF power of 100W and chamber pressure of 100mT, resulting in an approximate etch rate of 165nm/min. A short clean with O_2 plasma was performed prior to the SF_6/O_2 etch.

Finally the HSQ was removed using a solution of 10:1 $HF:H_2O$. The wafer was then either cleaved in cross-section for examination via scanning electron microscopy or had its facets die-sawed and polished for loss characterization and functionality testing. Some amount of process calibration was required to minimize sidewall roughness, maximize sidewall verticality and achieve accurate dimensional control.

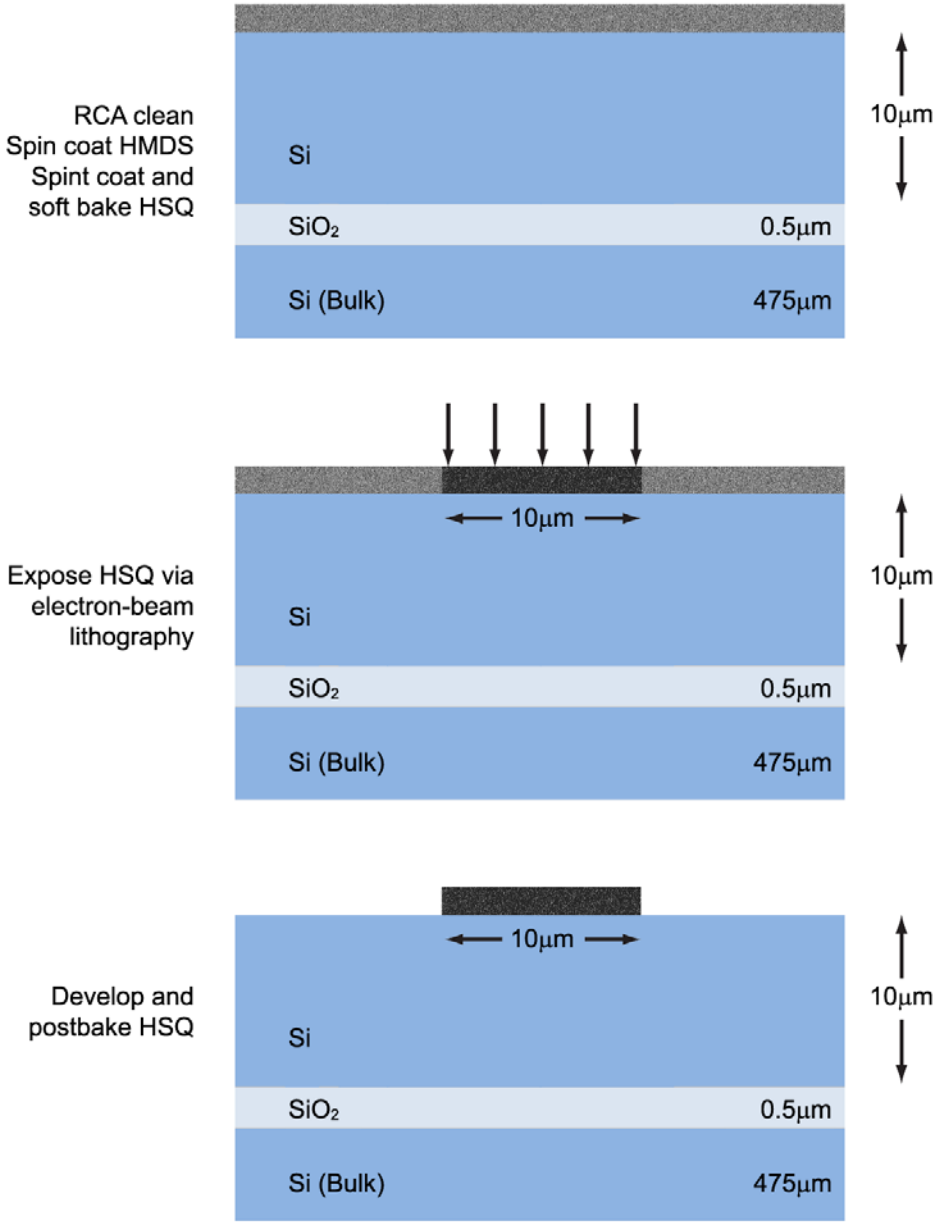

Figure 95 : Fabrication sequence for defining silicon-on-insulator rib waveguides.

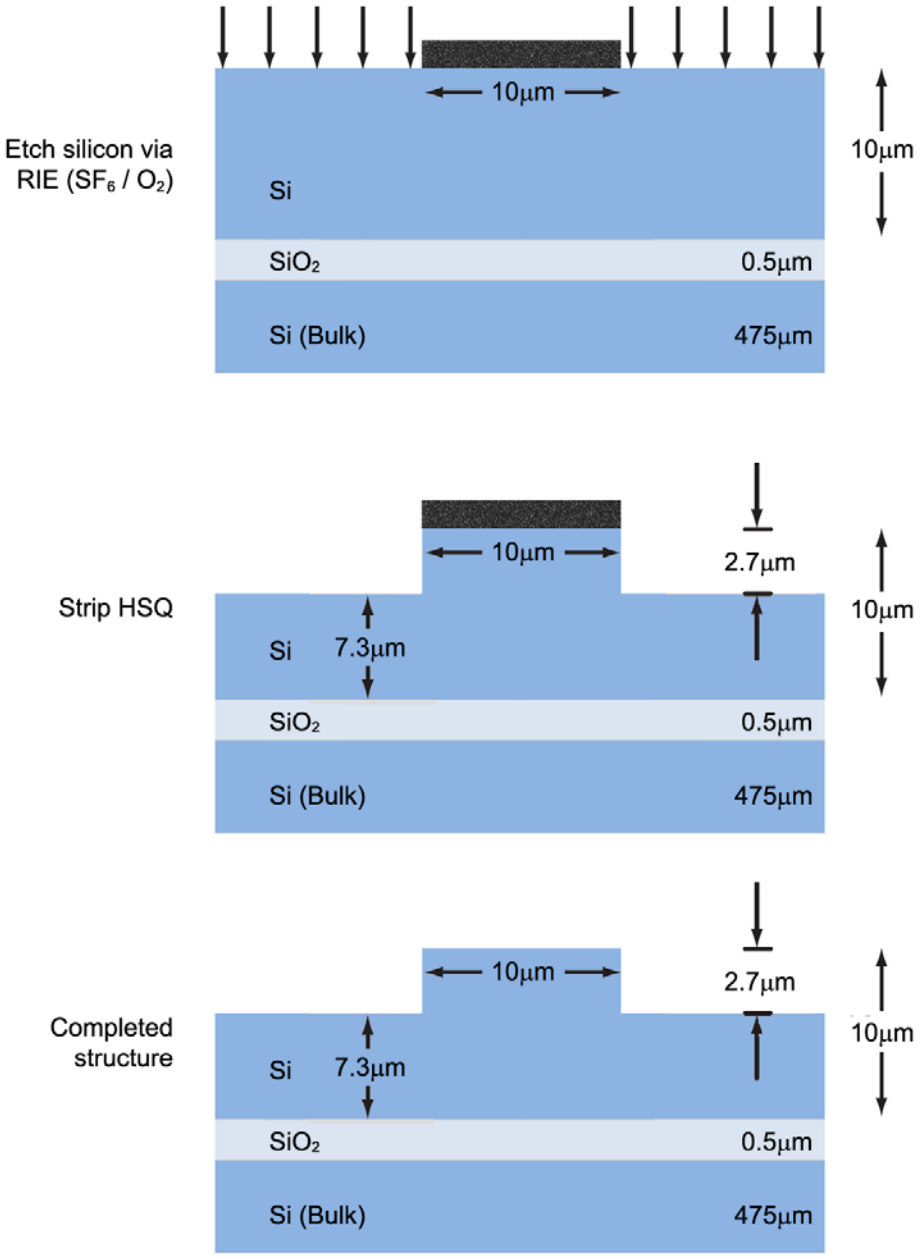

Figure 96 : (Continued) Fabrication sequence for defining silicon-on-insulator rib waveguides.

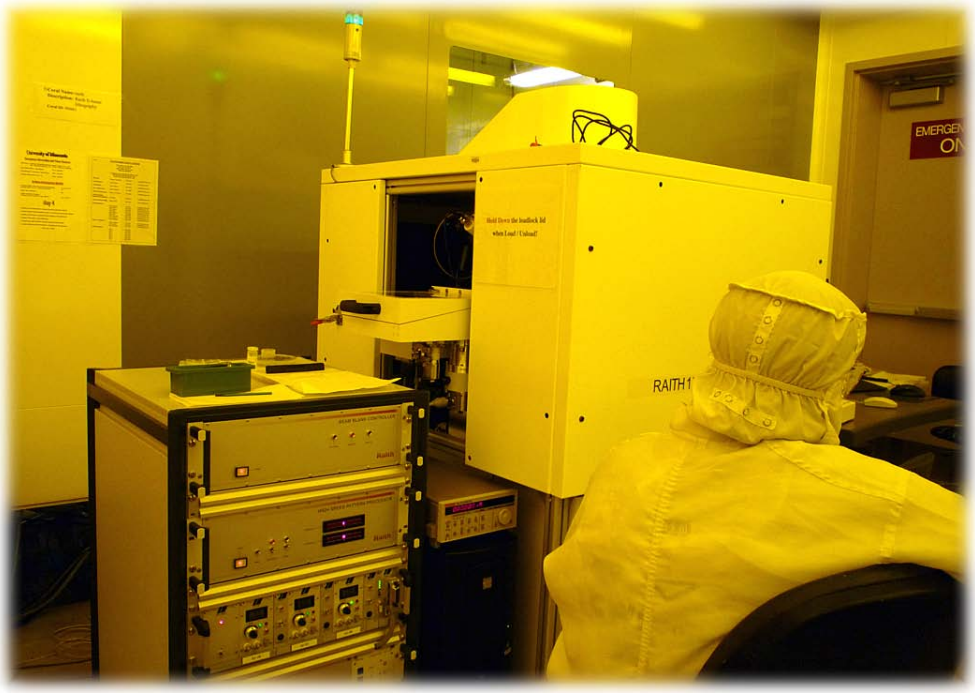

Figure 97 : Raith 150 electron-beam lithography and scanning electron microscopy system.

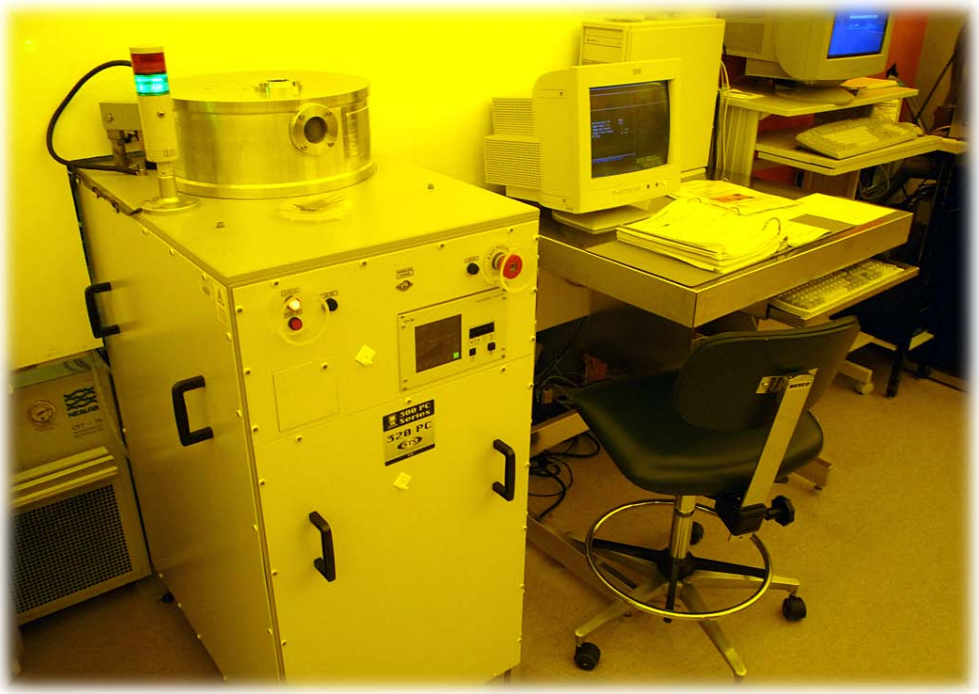

Figure 98 : STS Model 320 reactive-ion etching system.

6.1.1 Considerations

The four main approaches to the fabrication of commercial silicon-on-insulator wafers are separation by implanted oxygen (SIMOX), Smart Cut™, epitaxial layer transfer (ELTRAN) and BESOI. SIMOX wafers are made by a high-dose ion implantation of oxygen into plain silicon wafers (Celler & Cristoloveanu 2003; Jalali 1997). The buried insulator and device silicon layers cannot be made thicker than 500nm, which limits their applicability to integrated optics although they are widely used in microelectronics (Maszara et al. 1997). Smart Cut™ (Soitec 2012) involves implanting a thermally oxidized silicon wafer with hydrogen ions to introduce structural defects. The implanted wafer is then bonded to another silicon wafer, followed by a thermal anneal to separate the wafers at the hydrogen "zipper" layer. Uniform buried insulator and device silicon layers of up to 3μm and 1.5μm respectively are achievable in this approach. ELTRAN (Canon Inc. 2012) wafers are made by separating an epitaxial silicon layer from its original substrate using a high-pressure water jet, providing good uniformity and a large range of thicknesses for the buried insulator and device silicon layers. BESOI is the only inexpensive technology capable of providing the thick (≥ 5μm) device silicon layers required in this work.

HSQ is a non-chemically amplified negative tone resist that offers good etch selectivity to silicon. It was chosen instead of the more commonly used polymethylmethacrylate (PMMA) to avoid the extra pattern transfer step required for positive tone resists, which is an additional source of sidewall roughness. Chemically-amplified negative tone resists were eschewed due to the mandatory and critical post exposure bake. After being exposed and developed, the HSQ is postbaked to remove residual solvent, water and gasses as well as finalize resist cross-linking to improve its dry etch resistance.

The waveguide structures to be exposed via electron-beam lithography were biased down by approximately 80nm to account for anticipated feature broadening due to the finite electron-beam size. A conduction layer was not required as the sheet resistance of the wafer was deemed sufficient to prevent significant charge build up during exposure.

Reactive-ion etching was chosen in lieu of wet etch techniques to avoid the problem of undercutting as well as to obtain a higher etch anisotropy and finer dimensional control. A mixed SF_6/O_2 plasma was utilized due to SF_6 plasma having a higher silicon etch rate and selectivity than CF_4 plasma (Eisele 1981). The addition of O_2 improves the etch rate (d'Agostino & Flamm 1981) and anisotropy (Gomez et al. 2004; Jansen et al. 1996), which is critically important for optical waveguides where vertical sidewalls are required. As even trace amounts of contaminants in a plasma can drastically alter the achieved etch rate and profile, a short reactor clean is required prior to the actual etch.

6.2 Electron-beam Lithography

Scanning electron-beam lithography is a highly flexible high-resolution lithographic technique. A focused electron-beam is scanned across a surface covered by an electron-sensitive material (resist) to alter its solubility properties. Depending on the tone of the resist, areas exposed (positive) or not exposed (negative) are then removed by developing. Electron-beam lithography offers a larger depth of field and lower level of contamination damage than optical lithography without requiring a mask at the expense of throughput, since it is an inherently serial process. This makes it ideally suited for low-volume (eg. optical lithography mask making) and research applications.

An electron-beam lithography system consists of a chamber, electron gun and column as shown in Figure 99. The column houses the components required to generate an

electron beam, accelerate it to the desired working voltage as well as to focus, blank and deflect it as required by the pattern to be written. As the column and chamber are maintained in vacuum, samples are usually loaded in via a loadlock and placed on a laser interferometric stage.

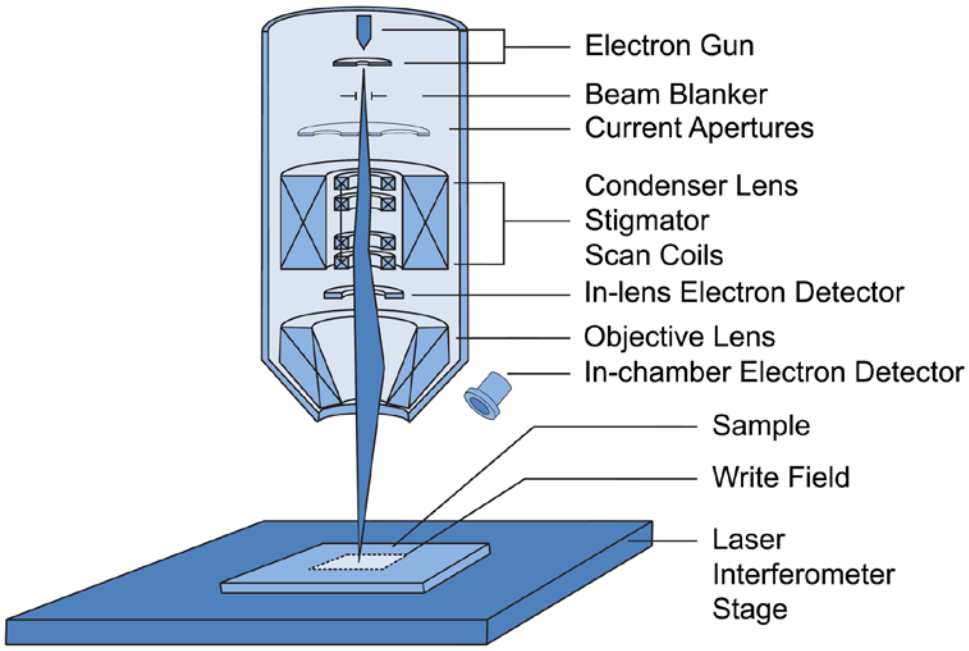

Figure 99 : Schematic view of the Raith 150 electron-beam lithography and scanning electron microscopy system.

6.2.1 Considerations

The Raith 150 electron-beam lithography system is based on a modified LEO Gemini column originally designed for scanning electron microscopy. As such it offers an unusual range of electron-beam energies (200eV – 30keV), with typical dedicated systems operating at 50keV – 100keV. For lithographic purposes, lower electron-beam energies are of limited interest despite some advantages such as lower charge build up, shorter exposure times due to lower required doses and reduced backscattering. Higher energies are usually

selected as they offer more compelling advantages such as a larger penetration depth to allow the use of thicker resist layers as well as higher resolution due to narrower beam diameters and decreased forward scattering. An exception to this rule is made for the Raith 150 where a voltage of 20keV was selected instead of the maximum system voltage of 30keV. This was done to avoid the use of the in-chamber secondary-electron detector. The in-chamber detector has a much lower signal-to-noise ratio than the in-lens detector, making parameter adjustments (aperture alignment, stigmation and focus) more problematic.

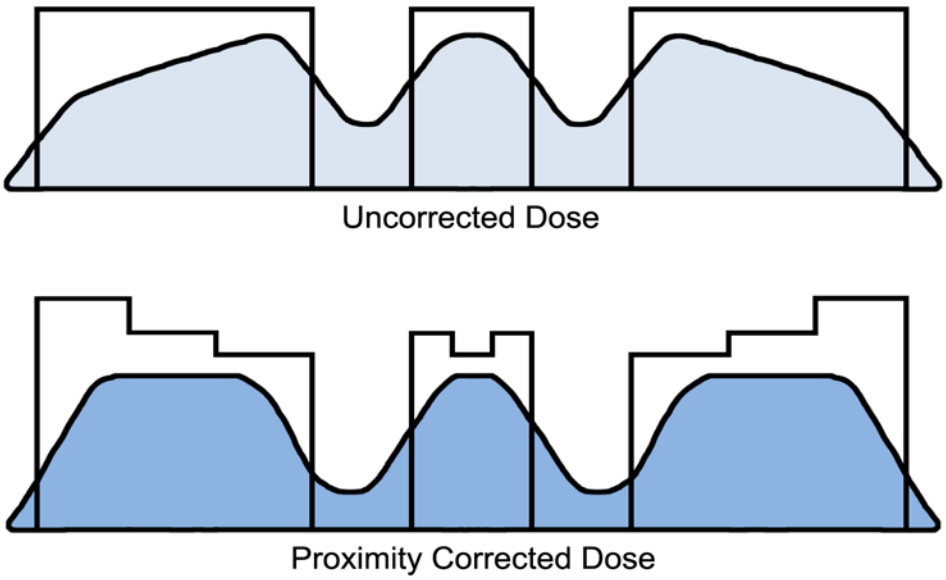

Figure 100 : Proximity effect correction by dose modulation. The effective dose is more uniform and the sidewall angle is improved.

The increased backscattering at higher voltages leads to over exposure of adjacent features and under exposure of regions at the edges of larger patterns. Achieving an optimal exposure is critically important for integrated optical devices to obtain smooth vertical sidewalls. Under exposed resist is characterized by moderately rough edges after development while over exposure leads to significant footing and roughness. Thus some

form of correction is necessary to account for backscattering. The serial nature of the scanning electron-beam lithography process allows for the control of the exposure dose by adjusting the dwell time at individual points. Convolving the point spread function of the Raith 150 system with the device layout provides the effective exposure dose as a function of position and the dose matrix is suitably altered to provide a uniform dose profile as illustrated in Figure 100.

An acute limitation of electron-beam lithography is the achievable accuracy of pattern placement. Absolute (rather than relative) dimensional control over the length of the chip is critical to the proper functioning of integrated optical devices, for instance to achieve proper coupling and phase. Large area patterns are constructed by stitching together a mosaic of small write fields. The area within each field is written by deflecting the focused electron-beam using the scan coils while successive fields are written by moving the interferometrically controlled stage. Distortions in stage motion introduce interfield or field stitching error, which cannot be systematically corrected due to its stochastic nature. Stitching errors are detrimental to fine-pitched devices such as Bragg gratings, in which the coherence required for the proper functioning of the device would be destroyed. Clearly, if stitching errors cannot be tolerated in a device, its dimensions would have to be limited to that of a single write field. In the case of the Raith 150, the usable field size is limited by the Gemini column to 100μm for the standard 6mm working distance. A thorough characterization of the system revealed a field stitching error with $\mu = 0$ and $\sigma = 20$nm (Goodberlet, Hastings & Smith 2001), which can be tolerated by the waveguides in this work.

Intrafield errors arise from a number of sources including substrate charging, digital-to-analog converter error and focus drift. In a vector scan system such as the Raith 150, the

electron beam is blanked and driven to the starting point of the scan vector. Once there, it is unblanked and scanned continuously to the vector end point, exposing the resist along the vector before being reblanked. Beam blanker timing errors would result in a positional error in the exposure, which can be mitigated by slowing down the exposure speed. The Raith 150 has a maximum exposure speed of 10MHz (or 10^6 pixels per second). However, a characterization of the system suggests that the selected exposure speed should not exceed 2MHz for acceptable results on a 100μm write field (Goodberlet, Hastings & Smith 2001). The exposure speed can be reduced by either decreasing the electron-beam current (at the expense of job time) or increasing the pixel size (at the expense of achievable resolution). A pixel size of 20nm was selected, which in tandem with the required dose of 190μC/cm^2 and beam current of 1nA translates into an exposure speed of 1.32MHz.

Another source of non-idealities is the pattern generation process. The integrated magneto-optic switches consist of long, curving waveguide structures that gradually approach and separate as they traverse the optical chip. This is in stark contrast to the dense Manhattan layouts that are prevalent in standard microelectronics designs. The Raith 150 system requires that a pattern be fractured into polygonal shapes which lie on a Cartesian grid. During exposure, these are filled in with pixels of finite dimensions and thus the complicated curved and sloped waveguides are ultimately approximated by a series of rectangular shapes, resulting in the pattern degradation illustrated in Figure 101.

The minimum pixel size is defined by the selected write field size and digital-to-analog converter resolution (2nm for a 100μm write field in the case of the Raith 150 with its 16-bit converter). In practice however, writing speed concerns impose a larger pixel size than the minimum as is the case in this work where a 20nm pixel size is utilized. It is

important that all device dimensions be rounded up or down to be multiples of the pixel size to ensure consistent discretization of the patterns.

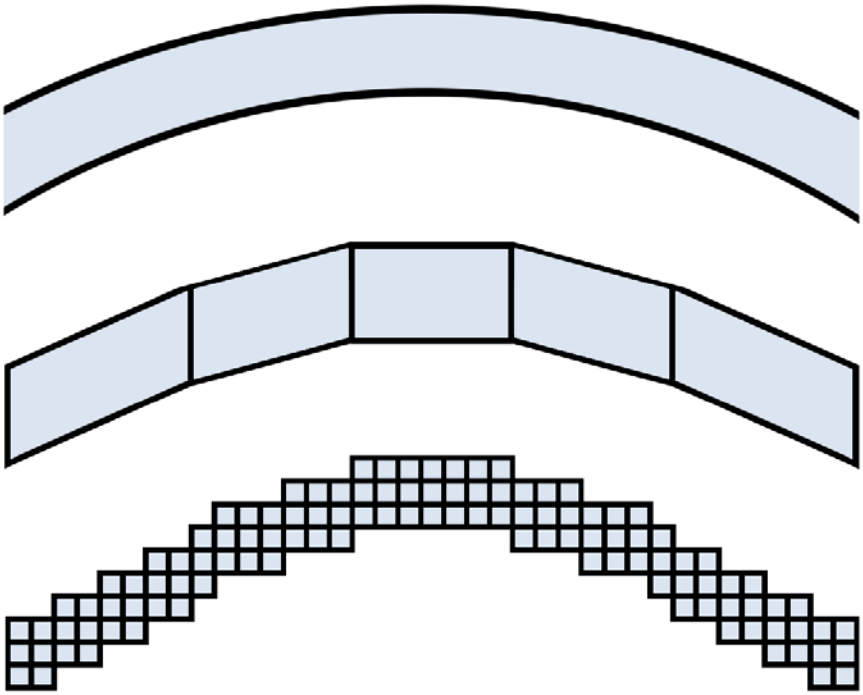

Figure 101 : Pattern fidelity degradation during the pattern generation process. The pixel size has been exaggerated for illustrative purposes.

The pattern degradation introduces a deterministic roughness due to the discretization process and arrangement of the pixels. However, the spectral components of roughness primarily responsible for optical propagation loss have spatial periods in the range of 500nm – 6μm (Chung & Dagli 1995), while that of the pattern degradation roughness is on the order of a pixel. Moreover, the pixel boundaries are smoothened due to finite beam size and the higher roughness spectral components are thus attenuated.

As a final point, given the size of the integrated magneto-optic switches (44mm long with 10μm wide waveguides), exposure of the full chip takes the better part of a day. Due to the age of the source in the particular Raith 150 utilized in this work, the electron beam

current drifts by as much as 5% per day. Thus for the long exposure times required to pattern the waveguide structures, a macro was introduced into the position list to monitor the beam current and adjust the dwell time appropriately.

6.3 Results

Figures 102 – 107 are scanning electron micrographs illustrating the fabricated silicon-on-insulator rib waveguides. The samples were cleaved in cross-section microscopy but the facets were not polished prior to imaging. The etch quality was good with clean and moderately smooth sidewalls. A consistent sidewall angle of approximately 88° and dimensional accuracy of ±1.5% were achieved, including in the critical coupling regions.

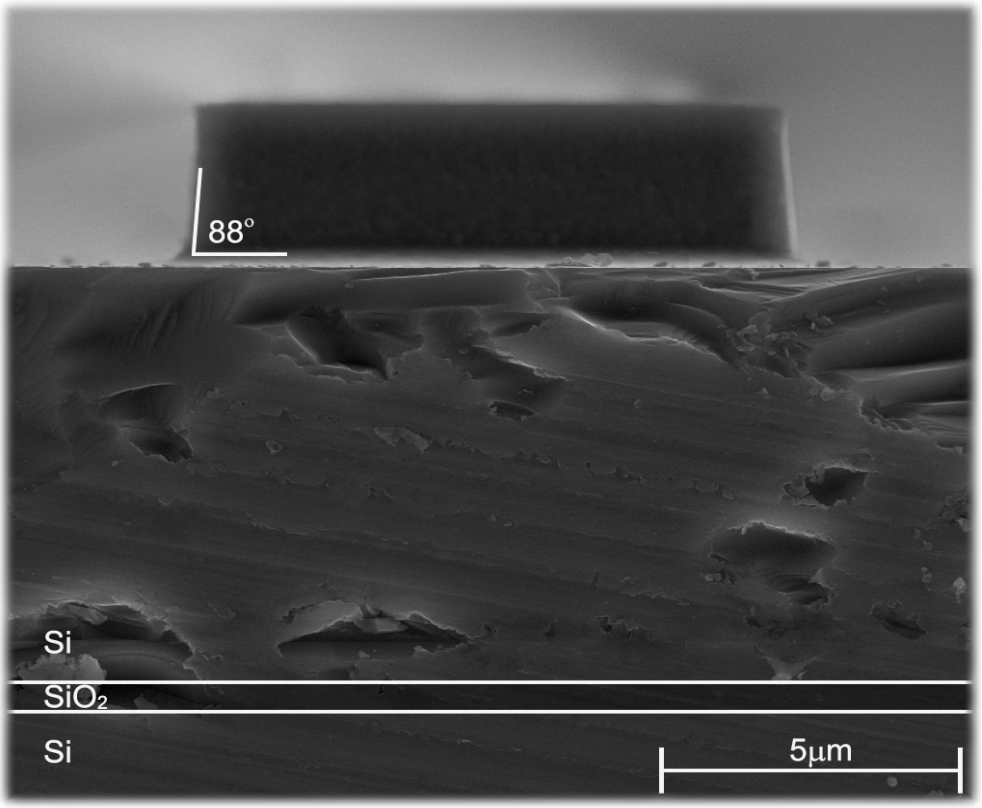

Figure 102 : Cross-section view micrograph of a silicon-on-insulator rib waveguide with an unpolished facet.

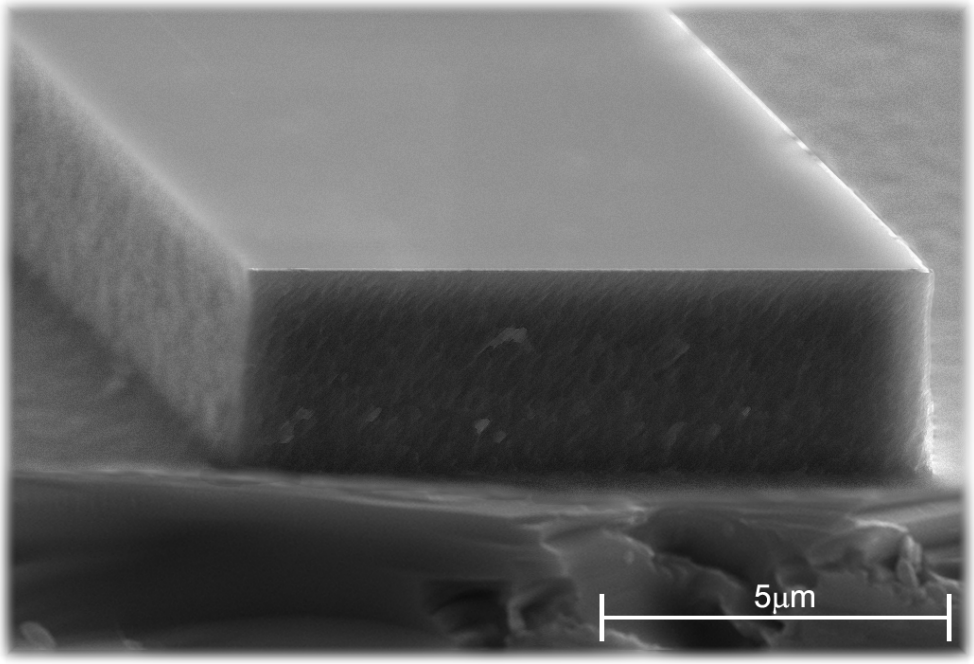

Figure 103 : Perspective view micrograph showing the sidewalls of a silicon-on-insulator rib waveguide with an unpolished facet.

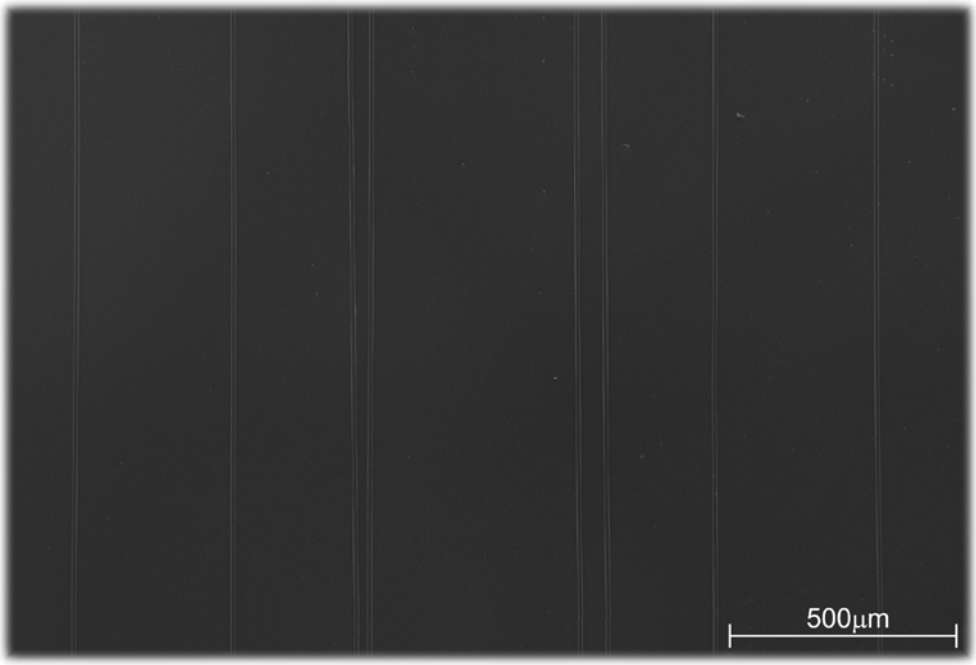

Figure 104 : Plan view micrograph of a portion of the integrated Mach-Zehnder magneto-optic switch chip.

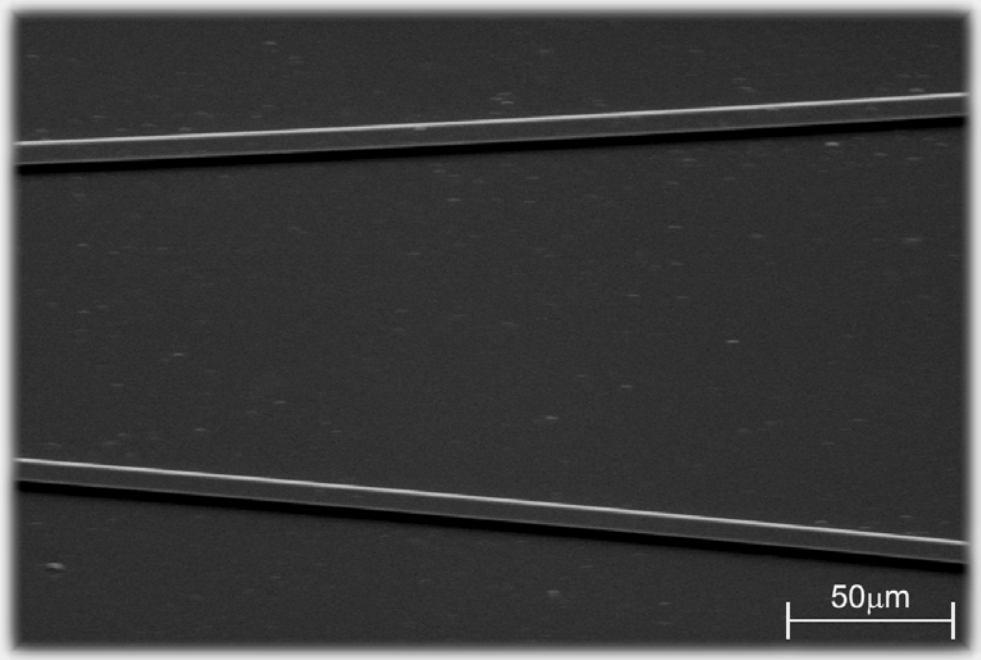

Figure 105 : Magnified plan view micrograph of two S-bend tapers on the integrated Sagnac magneto-optic switch chip.

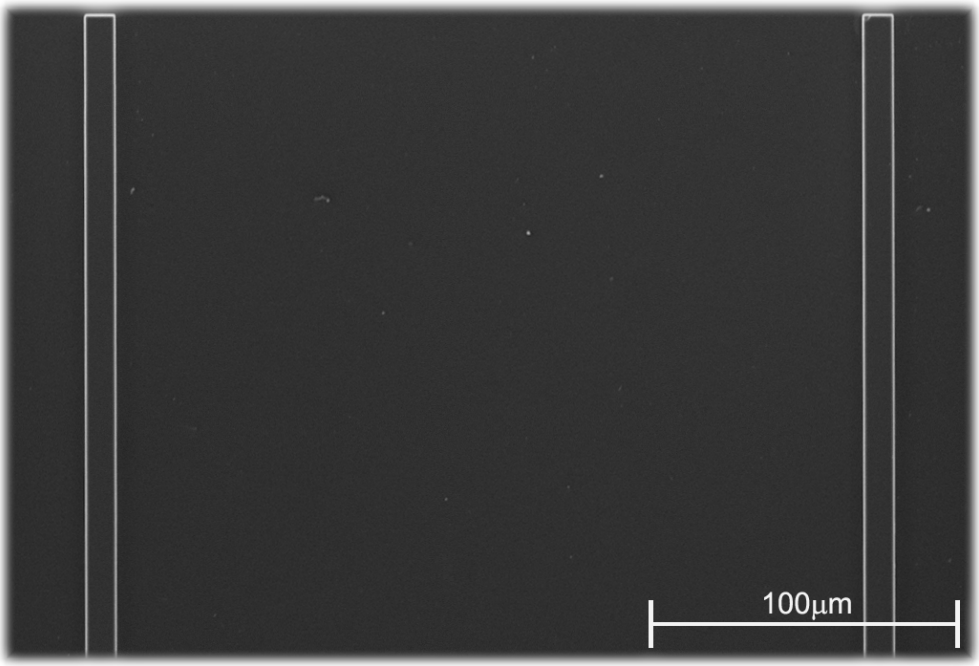

Figure 106 : Magnified plan view micrograph near the facet of the integrated Mach-Zehnder magneto-optic switch chip.

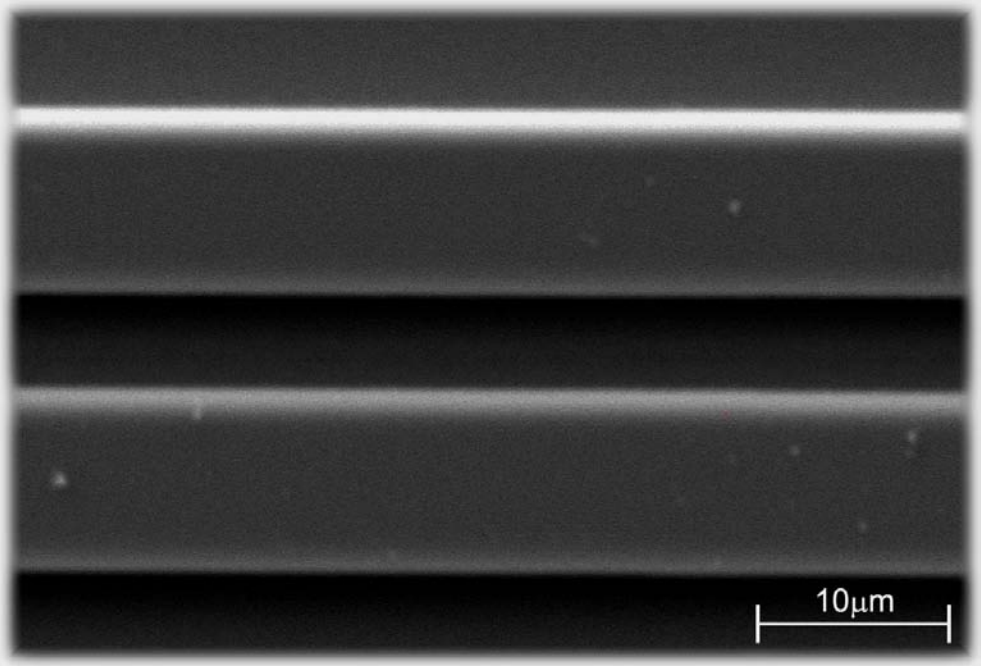

Figure 107 : Magnified plan view micrograph of coupling region on the integrated Sagnac magneto-optic switch chip.

CHAPTER 7. INTEGRATED SWITCH CHARACTERIZATION

The design and construction of the integrated magneto-optic switches have heretofore been elucidated at some length. The detailed metrology of integrated silicon-on-insulator rib waveguides is now reviewed.

A set of devices (3dB coupler, Mach-Zehnder and Sagnac interferometers) was designed and fabricated using the design and lithographic approaches described earlier. They are depicted schematically in Figures 108 and 109 with all of the relevant dimensions labeled. Identical 3dB couplers were utilized in the Mach-Zehnder and Sagnac interferometers and all the devices consist of square cross-section silicon-on-insulator rib waveguides with a nominal width and height of 10μm to facilitate efficient end-fire coupling to SMF-28 fiber. These dimensions result in an effective index contrast of 0.02% and a calculated mode mismatch loss to SMF-28 fiber of approximately 1dB.

A minimum center-to-center waveguide separation of 15μm was selected to impart a degree of fabrication tolerance, which leads to an inner-wall separation of 5μm. The waveguide separation at the chip facet was fixed at 250μm to allow for the use of commercially available V-groove fiber arrays during device characterization.

Finally, a radius of curvature of 223mm was adopted for the 3dB couplers and chip facet S-bend transitions. The bending loss for these structures was analyzed using the mode spectrum method described earlier and is predicted to contribute negligible loss (< 0.5dB), a finding subsequently confirmed by beam propagation method analyses in OptoDesigner.

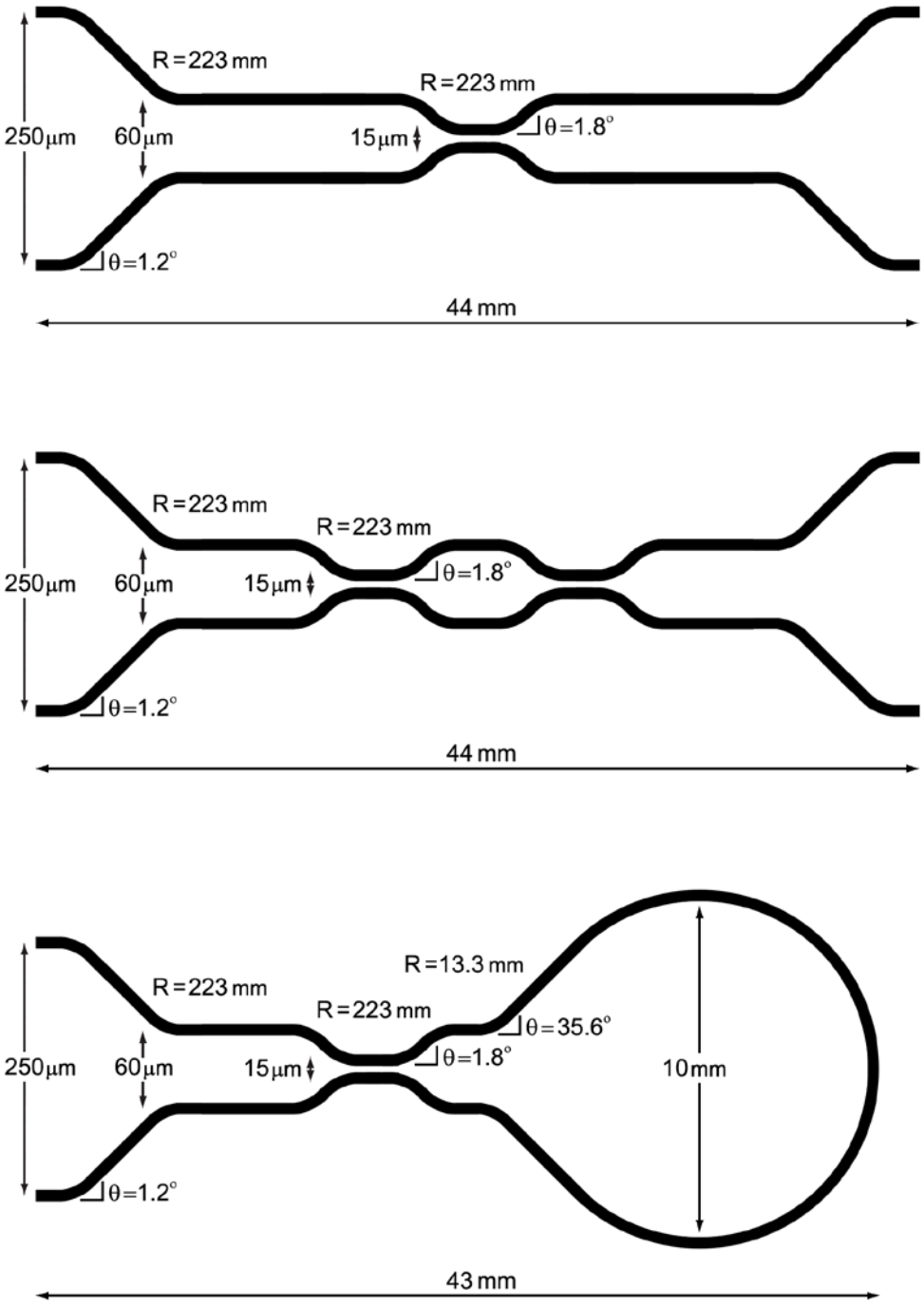

Figure 108 : Layout of a silicon-on-insulator rib waveguide 3dB coupler, Mach-Zehnder interferometer and Sagnac loop interferometer with all dimensions labeled (not to scale).

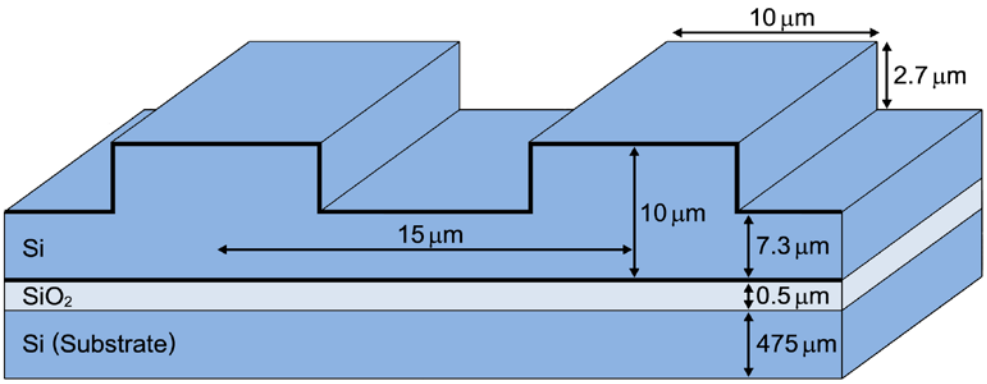

Figure 109 : Cross-section view of the silicon-on-insulator rib waveguides at the point of minimum separation.

7.1 Sample Preparation

Before a fabricated device can be characterized, an interface facet that is perpendicular to its waveguides must be created to expose their cross-sections for coupling to external fibers. This is achieved by either cleaving or die-sawing. Cleaving involves scribing the processed wafer with a diamond tip and fracturing it along the <111> plane, potentially producing an angled facet with low roughness. This method was determined to be unsuitable as a normal-angled facet is required for coupling to V-groove fiber arrays and propagation loss characterization. Moreover, it has poor reproducibility owing to difficulties in manual scribing alignment as well as a tendency for imperfect breaks to occur, resulting in rough facets.

The samples were separated using a Disco DAD 2H/6T die-saw. Prior to sawing, a thick layer of PMMA (a more stable and inexpensive resist than HSQ) was spin coated on the wafer to protect the waveguides from contamination and damage. While producing normal-angled facets, die-sawing results in severe surface imperfections as seen in Figure 102. These imperfections were smoothed out by polishing the facets with a Buehler MetaServ 250 tabletop polishing system. A minimum grit size of 0.1μm and constant pad

velocity of 125rpm produced smooth, optical quality facets. After polishing, the PMMA is removed and the samples cleaned.

7.2 Measurement Setup

The laboratory setup for the experimental evaluation of the fabricated silicon-on-insulator rib waveguide devices is shown schematically in Figure 110. Light from a laser source (either a tunable laser or supercontinuum source) is first directed through a Glan-Thompson polarizing prism to allow for control over the polarization state of the output light. Next, a broadband 10/90 coupler is used to tap off a fraction of the input light for power monitoring. This provides a reference against which other measurements are compared, allowing drifts in laser output power (and output power wavelength dependence in the case of the supercontinuum source) to be estimated.

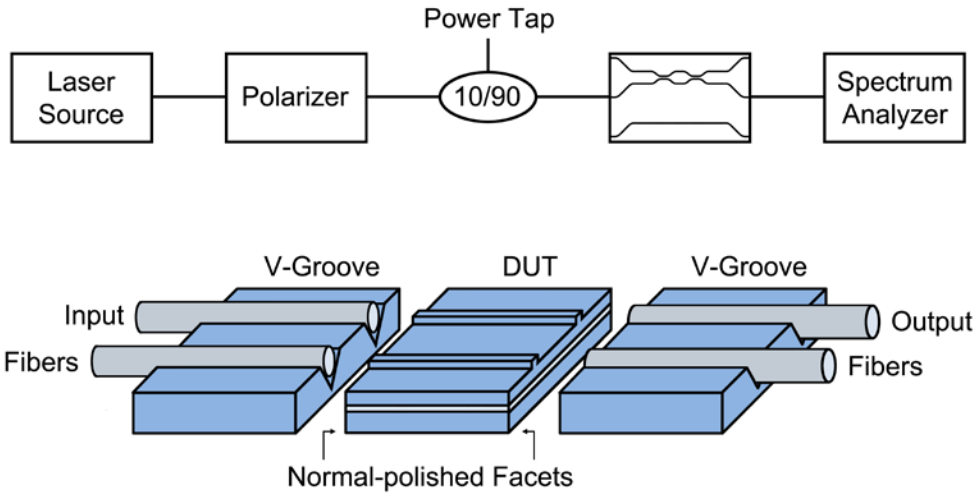

Figure 110 : Schematic of measurement setup for characterizing silicon-on-insulator rib waveguide devices.

Light from the polarizer is then fed into a V-groove pigtail SMF-28 fiber, which is in turn end-fire coupled into the waveguide input facet. An index-matching gel is used to

suppress reflections at the facet as well as to prevent spurious Fabry-Perot effects caused by the formation of an air gap between the V-groove and waveguide facet. Even though the free spectral range of the air gap is relatively large, the measured power changes substantially for fractional changes in the size of the gap. The use of index-matching gel greatly desensitizes the input and output coupling efficiencies to variations in the air gap size, increasing measurement stability and repeatability.

A similar arrangement is utilized at the waveguide output facet where light is end-fire coupled into an output V-groove SMF-28 fiber array and subsequently captured by an optical spectrum analyzer. As polarization-maintaining fibers were not utilized in the setup, minimal lengths of fiber were used and the fibers were clamped down where possible to prevent any bending or twisting that might alter the polarization state.

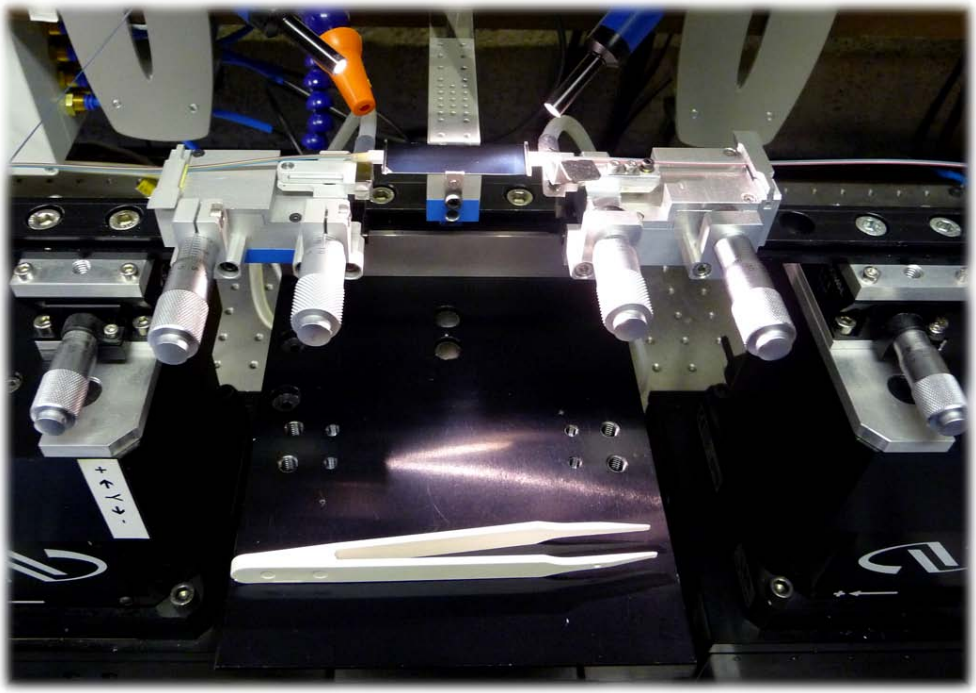

Figure 111 : End-fire coupling alignment and measurement setup for characterizing silicon-on-insulator rib waveguide devices.

Efficient end-fire coupling to integrated optical devices requires careful and precise alignment to ensure that the launch and capture angles that result in maximal power transfer are achieved. To this end, the measurement setup was built on an isolation table with two 6-axis stages that allow for x, y, z, tilt, roll and yaw adjustments. As shown in Figure 111, the input and output V-groove fiber arrays were mounted on the stages while the samples containing the devices remained stationary on a vacuum chuck. After a visual alignment, the V-grooves and waveguide facets were bonded with UV-curable and index-matched glue.

7.3 Loss Characterization

Insertion loss is an important figure of merit for any integrated optical device. Among the contributing components are bending, coupling and propagation losses. Based on insertion loss measurements at 1550nm, each S-bend induces a loss of approximately 0.25dB, which is higher than was calculated. This discrepancy can be attributed to the interaction of the bent mode profile with the non-smooth waveguide sidewalls, which results in additional loss due to sidewall scattering.

Coupling loss could not be measured directly but can be estimated by summing the calculated losses arising from mode mismatch between the waveguide and fiber (~ 1dB per facet) as well as reflections at the waveguide / fiber interface. The use of the Fresnel reflection equation below results in a calculated reflection loss of 0.8dB per facet with an index-matching fluid.

$$R = \left(\frac{n_1 - n_2}{n_1 + n_2} \right)^2 \tag{7.1}$$

Propagation loss arises from a number of factors including substrate leakage, absorption and scattering. 1dB/cm is the widely accepted benchmark for propagation loss since an integrated optical circuit is typically a few centimeters in length. Thus a loss of 1dB/cm provides a sufficient signal-to-noise ratio at the circuit output.

Substrate leakage is nominally negligible owing to the thickness of the oxide isolation layer (5000Å). Absorption loss has an interband and free carrier component. While interband absorption can be significant (2.87dB/cm at 1100nm), it drops significantly as wavelength increases (0.0004dB/cm at 1523nm) thus rendering it negligible for the devices in this work (Aspnes 1988).

Free carrier absorption can be described by the Drude-Lorentz equation (Auslender & Hava 1992). The device silicon layer of the wafers used in this work is phosphorous-doped and were measured to have a resistivity of 13Ω-cm, translating into a carrier concentration (N) that is on the order of $10^{15}/cm^3$ (Thurber et al. 1981). The linear absorption induced by background free carriers can thus be estimated from σN, where the free carrier absorption coefficient value for silicon is $\sigma = 1.45 \times 10^{-21}/m^2$. The free carrier absorption is thus calculated to be approximately 0.07dB/cm and it is clear that it does not become significant until carrier densities much higher than $10^{16}/cm^3$ are encountered.

Finally, there are two types of scattering loss in an optical waveguide – volume scattering and surface scattering. Volume scattering is caused by imperfections in the bulk waveguide material, such as voids, crystalline defects and contaminant atoms. It is proportional to the number of imperfections per unit length and depends strongly on the size of the imperfections relative to the wavelength of light in the material. Due to the well-established nature of silicon-on-insulator material technology, volume scattering should be negligible due to sufficient material improvement prior to waveguide fabrication.

Surface scattering is generally considered to be the dominant loss mechanism in integrated optical waveguides. It is caused by roughness at the waveguide cladding interface, which is characterized by a root-mean-square roughness σ (a measure of asperity height) and correlation length L_C (a measure of asperity width). A closed-form analytical expression that describes the scattering loss in slab waveguides in terms of normalized parameters of waveguide geometry and surface roughness was proposed in (Payne & Lacey 1994). It is based on the direct computation of the far field radiation loss caused by asperities at the waveguide surface and is written as :

$$\alpha_{scattering} = \frac{\sigma^2}{\sqrt{2}k_o d^4 n_{core}}.g.f \tag{7.2}$$

where k_o is the free-space wavenumber and d is the waveguide half-width. g is determined by waveguide parameters and f is determined by the waveguide index step and correlation length. The scattering loss coefficient in Equation 7.2 has the following upper bound :

$$\alpha_{scattering} \leq \frac{\sigma^2}{k_o d^4 n_{core}}\kappa \tag{7.3}$$

where the value of κ depends on the assumed statistical distribution of roughness. Applying this analysis to silicon-on-insulator rib waveguides first requires the application of the effective index method as illustrated in Figure 65. n_{core} in Equations 7.2 and 7.3 is then replaced by the effective core index.

Waveguide propagation loss can be obtained empirically using the cutback and Fabry-Perot methods. The cutback method is conceptually simple, literally involving the measurement of output intensities of a waveguide that is cleaved to progressively shorter

lengths. By assuming constant coupling and propagation losses, the propagation loss coefficient can be estimated using the following expression :

$$\alpha_{prop} = \frac{\ln(P_2 / P_1)}{L_1 - L_2} \tag{7.4}$$

The limitation to the accuracy of this technique arises from uncertainties in the coupling loss due to variations in the quality of the waveguide facets. This technique is thus unsuitable for the measurement of the silicon-on-insulator rib waveguides as the coupling loss is comparable to the maximum anticipated propagation loss (1dB/cm), which leads to a high measurement uncertainty.

The Fabry-Perot method (Kaminow & Stulz 1978) is based on the extraction of propagation loss from the transmission spectrum of a waveguide. A waveguide with facets polished at a normal angle forms a lossy Fabry-Perot cavity. Thus a transmission scan vs. wavelength for a waveguide with highly polished facets results in Fabry-Perot fringes with a free spectral range of :

$$\Delta\lambda = \frac{\lambda^2}{2Ln_{eff} + \lambda} \tag{7.5}$$

This method is essentially a measurement of the cavity quality factor and the propagation loss coefficient of the waveguide can be inferred as follows :

$$\alpha_{prop} = -\frac{1}{L}\ln\left(\frac{1}{R}\frac{\sqrt{I_{max}/I_{min}} - 1}{\sqrt{I_{max}/I_{min}} + 1}\right) \tag{7.6}$$

where I_{max} and I_{min} are the maximum and minimum fringe intensities respectively, L is the cavity length and R is the internal reflection coefficient at the chip facet approximated by the

Fresnel reflection equation for normal incidence. The advantages afforded by the Fabry-Perot method are that it is non-destructive and independent of the fiber-to-waveguide and waveguide-to-fiber coupling losses. Measurement uncertainties using this method stem from its reliance on an accurate estimate of the internal reflectivity at the two waveguide facets. The reflectivity of a perfect facet is well described by the Fresnel reflection equation. However, if the facet is damaged, scratched or misoriented, the internal reflectivity can deviate significantly from this estimate.

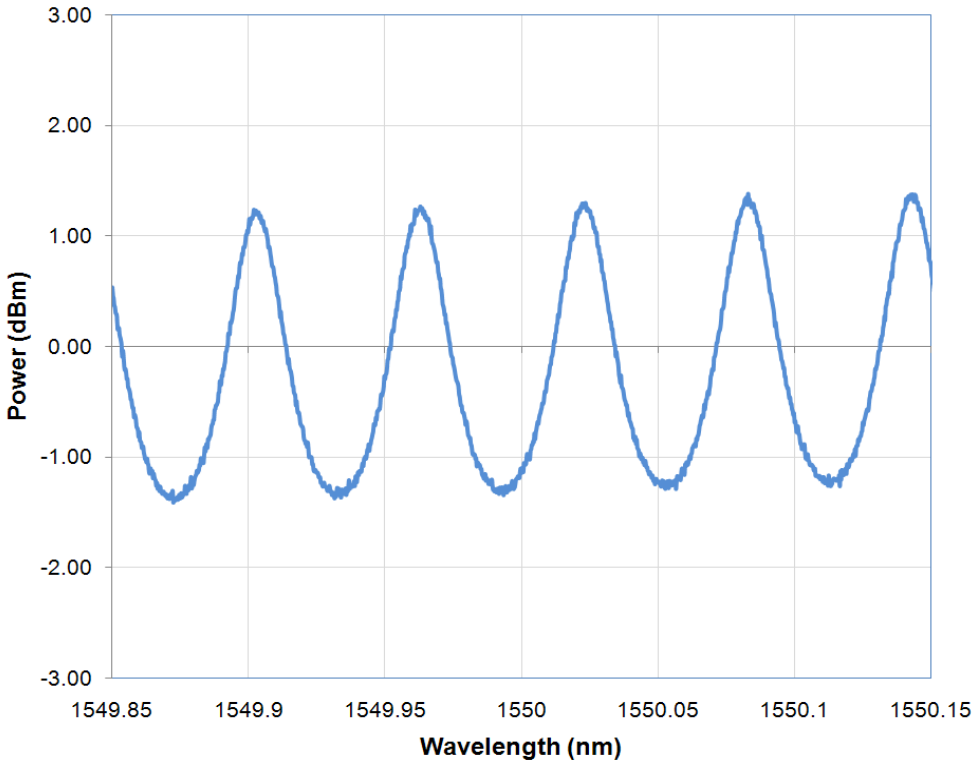

Figure 112 : Fabry-Perot transmission spectrum for a silicon-on-insulator rib waveguide that is representative of a 6mm sample.

The silicon-on-insulator rib waveguide structures being characterized have a very high effective index, which constrains the length of the waveguide test structure due to finite equipment wavelength resolution. The 44mm straight waveguide test structures included on

the integrated Mach-Zehnder magneto-optic switch chip have a free spectral range of 8pm. Due to the limited wavelength resolution of the tunable laser source used, an accurate assessment of the Fabry-Perot fringes could not be performed. This necessitated the cleaving of the waveguide to a shorter length for loss characterization. A 6mm length resulted in a free spectral range of 58pm and a measured loss of 0.4dB/cm inferred from the contrast ratio of the fringes shown in Figure 112, where the spectrum has been centered at an average power of 0dBm for clarity. The propagation loss was measured to be approximately equivalent (within the measurement uncertainty) for TE and TM polarizations.

7.4 Functional Characterization

The 3dB coupler, Mach-Zehnder interferometer and Sagnac loop interferometer were measured by illuminating them with a supercontinuum source and measuring the output spectrum. The measured spectra (normalized to the total power in the bar and cross outputs) are shown in Figures 113 – 116. The coupler has an insertion loss of 6.5dB at 1550nm and exhibits broadband 3dB splitting behavior. Some polarization dependence is noted in Figure 114, where the coupling ratio is consistently about 3.8% lower for TM-polarized light, a trend consistent with calculations of the coupling constant (see Figure 59).

Owing to the broadband performance of the 3dB coupler, the Mach-Zehnder interferometer also functions correctly over a broad spectral range, with a TE contrast ratio of over 20dB and insertion loss of 7.1dB at 1550nm. However, the polarization dependence of the 3dB coupler results in a lower TM contrast ratio of approximately 19dB at 1550nm.

Somewhat unfortunately, the theoretical predictions of bending loss for the radii of curvature utilized in the Sagnac magneto-optic switch proved to be accurate. No measurable response was detected from the Sagnac interferometer.

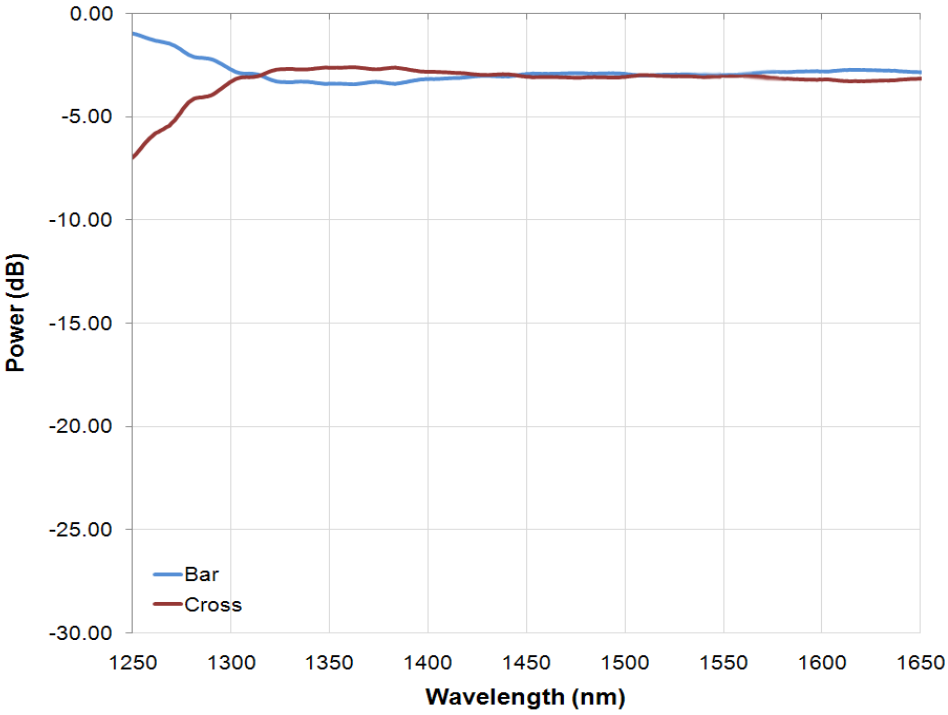

Figure 113 : Measured TE output spectrum of 3dB coupler.

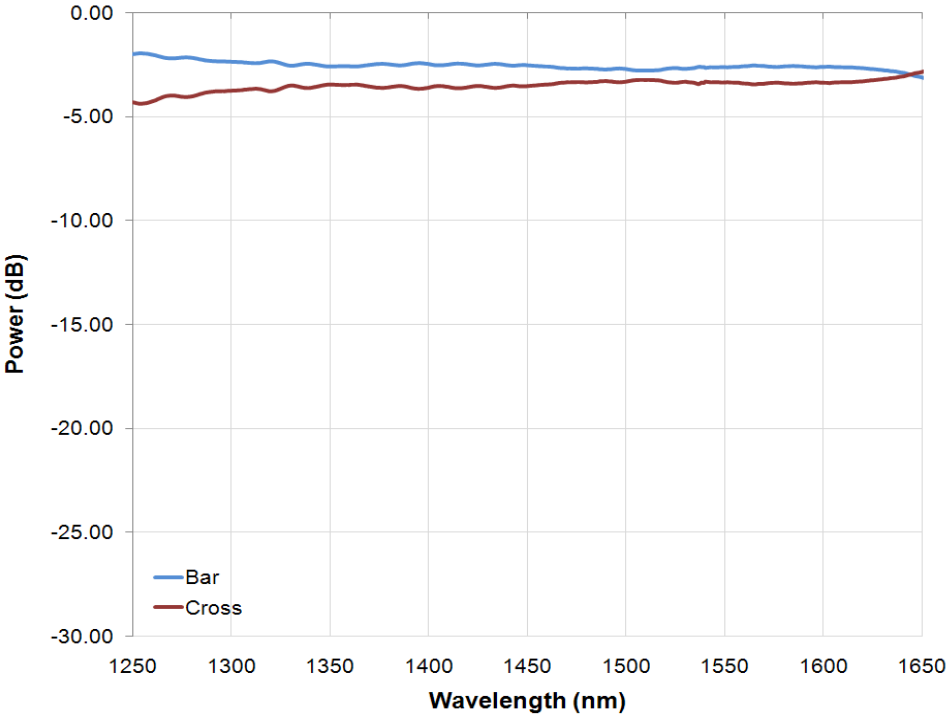

Figure 114 : Measured TM output spectrum of 3dB coupler.

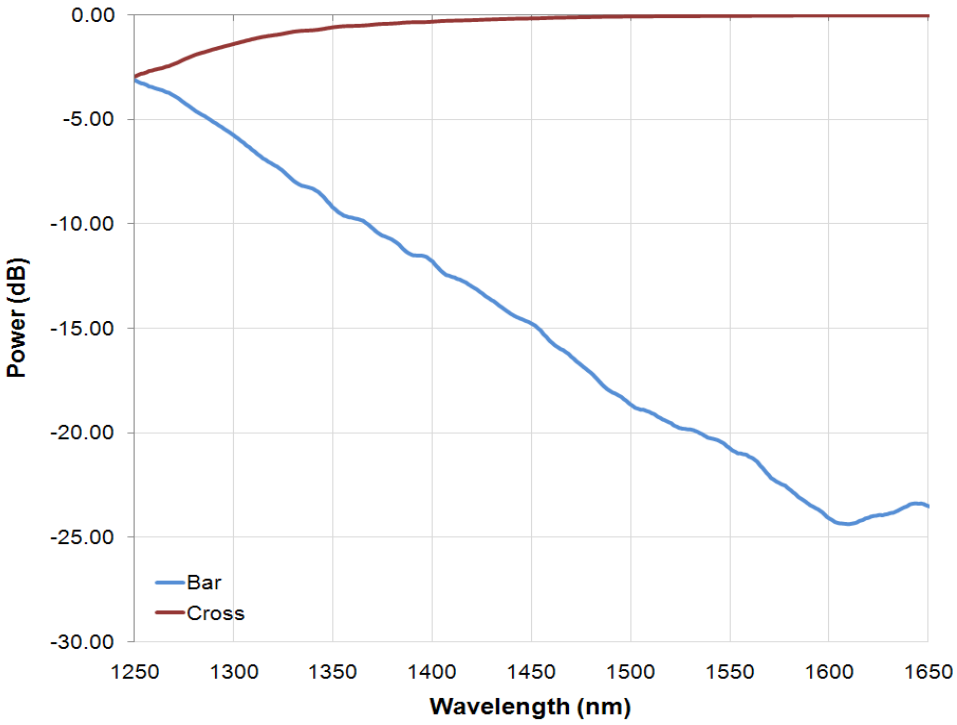

Figure 115 : Measured TE output spectrum of Mach-Zehnder interferometer.

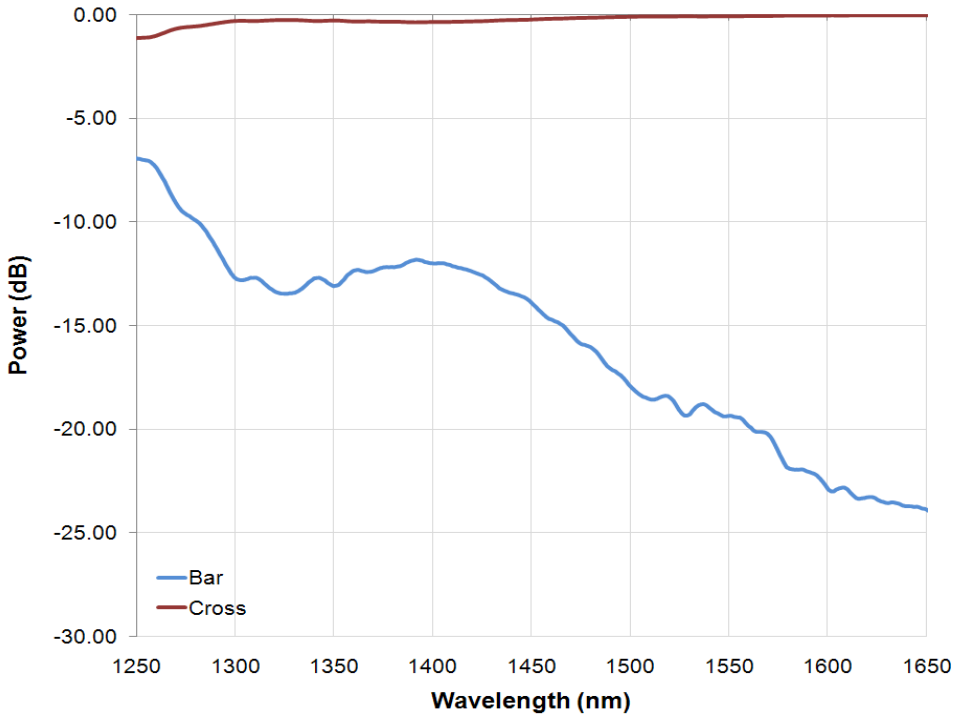

Figure 116 : Measured TM output spectrum of Mach-Zehnder interferometer

CHAPTER 8. CONCLUSION

The paradigm shift from connection-oriented communications to IP-centric packet switched data traffic over the past decade has necessitated transparent networks that are scalable and insensitive to bit-rate, protocol and format. New technologies are thus required to facilitate the most basic networking functions; routing, switching and multiplexing. An overview of several different switch implementation technologies was given with each representing a different set of engineering tradeoffs and having different performance characteristics in terms of switching speed, extinction ratio, scalability, insertion loss, polarization-dependent loss, crosstalk and power consumption.

A number of recent advances in suitable materials have made switches based on magneto-optic effects more viable and instigated the proposal, analysis and characterization of fiber-based switches utilizing bismuth-substituted iron garnets as Faraday rotators in Mach-Zehnder and Sagnac interferometer configurations. The issues and limitations of these switches were investigated and they were found to perform below theoretical limits, indicating the potential for improvement. Efforts were thus undertaken to model and optimize the field generating coil, resulting in new tractable models and approaches for computing and optimizing the coil impedance parameters.

In the interest of improving the performance and scalability of the fiber-based switches, microphotonic versions of the switches were designed, analyzed, fabricated and characterized. This process included the selection of a suitable material system, design of the waveguide geometry while taking various considerations into account (mode confinement, birefringence, coupling efficiency to fiber, bending loss, etc.), creation and

calibration of a suitable fabrication process as well as determination of the switches' fabrication tolerance.

While the larger waveguide cross-section of the microphotonic switches enabled efficient coupling to fiber and greatly reduced geometrical birefringence, the weak confinement resulted in necessarily longer device lengths to minimize bending losses, a tradeoff made feasible by the low waveguide propagation loss. The small but finite birefringence resulted in a degree of polarization dependence in the measured switch performance. Consequently, compact and nominally non-birefringent nanophotonic versions of the interferometric switches are proposed and analyzed in the interest of further improving switch performance and scalability.

In conclusion, the results of the research contained herein aid in furthering the application of magneto-optic materials in general, and the development of magneto-optic switches in specific. The contributions over the course of this work are summarized below :

- Characterization and analysis of fiber-based magneto-optic switches
- Modeling and optimization of field generating coil impedance parameters
- Design and analysis of micro- and nanophotonic integrated magneto-optic switches
- Creation and calibration of a fabrication process for microphotonic silicon-on-insulator rib waveguides and devices based on direct-write scanning electron-beam lithography
- Characterization of microphotonic silicon-on-insulator rib waveguides, couplers, Mach-Zehnder and Sagnac loop interferometers

8.1 Future Work

Having successfully demonstrated microphotonic silicon-on-insulator rib waveguide couplers and Mach-Zehnder interferometers, the next task will be to investigate deep trench etching for enabling the insertion of the bismuth-substituted iron garnet Faraday rotators to form complete magneto-optic switches. Preliminary attempts at etching the trenches resulted in scalloping on the sidewalls due to the alternating etch and passivation steps of the Bosch process, which would result in severe scattering losses at the waveguide - garnet interfaces.

Another obvious task would be the creation of a suitable fabrication process for the proposed nanophotonic magneto-optic switches. While every effort was made to ensure accurate dimensional control in fabricating the microphotonic switches, this is even more critical for nanophotonic structures due to the decreased degree of fabrication tolerance and the desire to attain zero birefringence via geometry control. In addition, the quality of the waveguide sidewalls becomes more important to minimize propagation losses due to the increased interaction of the guided mode with the sidewall. Sidewall quality was only regarded qualitatively in this work by means of surface visual reflectivity and cross-section scanning electron micrographs after etching. A quantitative evaluation of sidewall roughness via atomic force microscopy would be appropriate. If deemed excessive, techniques to reduce it (eg. post-etch oxidation of the silicon surface (Sparacin, Spector & Kimerling 2005)) would certainly merit investigation.

An interesting line of investigation would be the effect of spot size on the magneto-optic switching efficiency. This could be accomplished by utilizing an inverted adiabatic taper (Almeida, Panepucci & Lipson 2003) as illustrated in Figure 117. In contrast to standard tapers (Day et al. 2003), the waveguide width is decreased to a narrow tip to create a loss of

mode confinement and force mode expansion. The result is a compact device relative to standard tapers (tens of μm vs. several mm) that is fairly broadband (several hundred nm) and single-moded. Performance can be further enhanced by depositing a cladding material to further reduce the index contrast and thus the mode confinement.

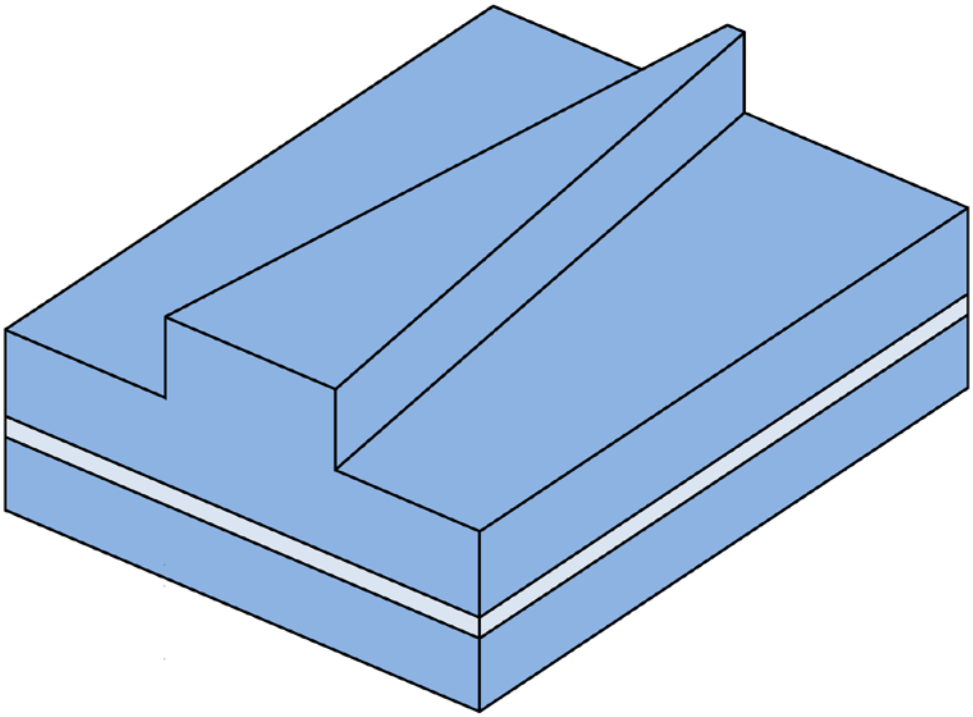

Figure 117 : Geometry of an inverted silicon-on-insulator rib waveguide taper.

Finally, a degree of instability in the extinction ratio was noted when characterizing the fiber-based switches. This is conjectured to be caused by irreversible displacement of domain walls caused by energy minimization in defect sites. A possible approach to stabilize the magnetic domains is to etch the thin film into separated islands (Hill 1984).

The author has mentioned a few possible directions for future research and it is his hope that this work provides adequate theoretical and practical information to encourage others to develop new ideas and applications for magneto-optic materials.

APPENDIX A. MEASUREMENT APPARATUS

The equipment and components in the High-speed Systems Engineering laboratory that were utilized in the course of this work are shown and tabulated below.

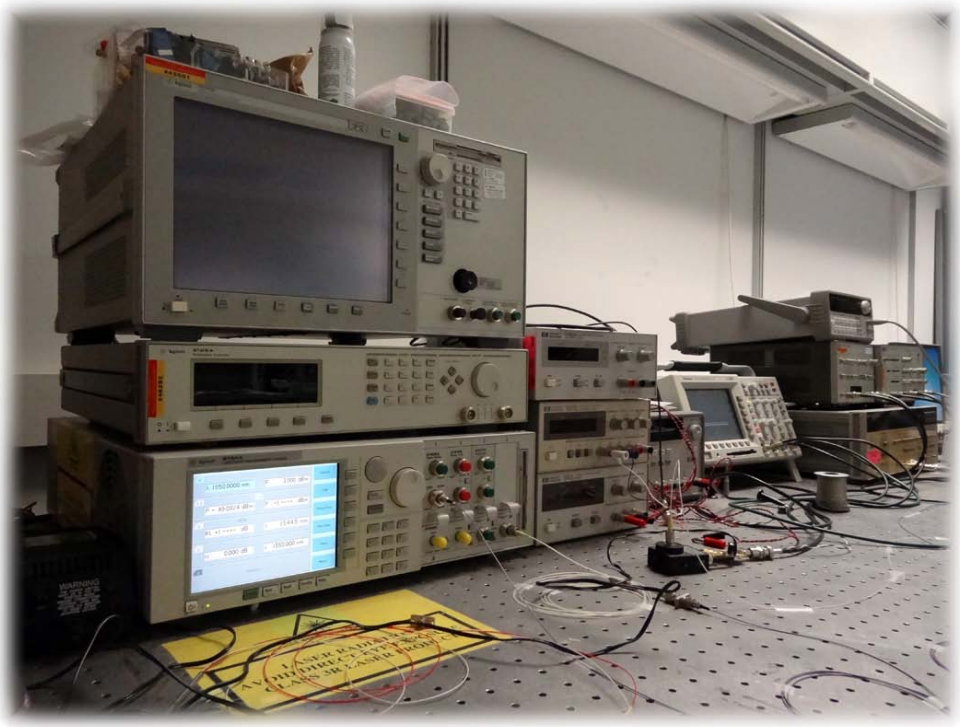

Figure 118 : Overview of the High-speed Systems Engineering laboratory.

Table 5 : Equipment and components utilized in this work.

	Manufacturer	Model
Tunable Laser	Agilent	81640A
Optical Power Sensor	Agilent	81635A
Optical Spectrum Analyzer	Agilent	86146B
Polarization Controller	Agilent	8169A

3dB Optical Coupler	Thorlabs	10202A-50-FC
Fiber Phase Shifter	General Photonics	FPS-001-01
Optical Circulator	Thorlabs	6015-3
Optical Isolator	Thorlabs	IO-H-1550
Photodiode	Thorlabs	DET10C
DC Power Supplies	Agilent	E3631A
	Hewlett-Packard	E3610A
	Hewlett-Packard	E3611A
	Hewlett-Packard	E3630A
	Lambda	LLS8081
Oscilloscope	Tektronix	TDS3054
Function Generator	Agilent	33120A

APPENDIX B. BEAM PROPAGATION METHOD

The beam propagation method (Feit & Fleck 1978) is a valuable tool in the design and analysis of integrated optical structures. Indeed, most commercial photonics design software suites are based on this technique. Its popularity arises from the significant advantages it affords, such as being conceptually straightforward, readily applicable to arbitrary waveguide geometries, computationally efficient, extensible, and automatically inclusive of both guided and radiating fields as well as mode coupling and conversion.

A waveguide supports an electromagnetic field that can be expressed in terms of electric field components to produce the following vector wave equation :

$$-\nabla^2\vec{E} + \nabla\left(\nabla \bullet \vec{E}\right) = n^2 k_0^2 \vec{E} \tag{B.1}$$

The scalar approximation of Equation B.1 can be obtained by assuming that the field magnitude and gradient are constant across dielectric boundaries. Thus, the vector field $\bar{E}$ is replaced by the scalar field ϕ, giving rise to the ubiquitous Helmholtz equation for :

$$\frac{\partial^2\phi}{\partial x^2} + \frac{\partial^2\phi}{\partial y^2} + \frac{\partial^2\phi}{\partial z^2} + k_0^2 n^2\left(x,y,z\right) = 0 \tag{B.2}$$

where the geometry of the problem is defined entirely by the refractive index profile n.

The beam propagation method involves making several simplifying approximations. The first is the assumption that the guiding axis is predominantly along the z direction. The second is the assumption that the most rapid variation in the field ϕ is the phase variation

due to propagation along said guiding axis. This phase variation is factored out of the field by introducing a new field φ :

$$\phi(x,y,z) = \varphi(x,y,z)e^{jn'k_o z} \tag{B.3}$$

where n' is a reference refractive index, typically taken to be that of the cladding (Xu & Huang 1995). Introducing φ into Equation B.2 results in the altered Helmholtz equation :

$$\frac{\partial^2 \varphi}{\partial z^2} + j2k_0 n'(x,y,z)\frac{\partial \varphi}{\partial z} + \frac{\partial^2 \varphi}{\partial x^2} + \frac{\partial^2 \varphi}{\partial y^2} + k_0^2\left(n^2(x,y,z) - n'^2(x,y,z)\right)\varphi = 0 \tag{B.4}$$

The final approximation is the slowly varying envelope or paraxial approximation, where the variation of φ with respect to z is assumed sufficiently slow to enable the neglect of the first term in Equation B.4. This limits consideration to fields propagating along or at shallow angles to the z axis. Additionally, the removal of the second-order derivative precludes the possibility of backward travelling wave solutions, thus rendering the beam propagation method a unidirectional technique.

BIBLIOGRAPHY

Abdulla, S, Kauppinen, L, Dijkstra, M, Berenschot, E, de Boer, MJ, de Ridder, RM & Krijnen, G 2011, 'Mechano-optical switching in a MEMS integrated photonic crystal slab waveguide', IEEE Conf. MEMS, pp. 9-12.

Abramowitz, M & Stegun, IA 1965, Handboook of Mathematical Functions, 1st end, Dover, New York.

Aichele, T, Lorenz, A, Hergt, R & Görnert, P 2003, 'Garnet layers prepared by liquid phase epitaxy for microwave and magneto-optical applications - a review', Cryst. Res. Tech., vol. 38, pp. 575-587.

Al-Hetar, AM, Mohammad, AB, Supa'at, ASM & Shamsan, ZA 2011, 'MMI-MZI Polymer Thermo-Optic Switch With a High Refractive Index Contrast', J. Lightwave Tech., vol. 29, no. 2, pp. 171-178.

Almeida, VR, Panepucci, RR & Lipson, M 2003, 'Nanotaper for compact mode conversion', Optics Lett., vol. 28, no. 15, pp. 1302-1304.

Anicin, BA, Davidovic, DM, Karanovic, P, Miljevic, VM & Radojevic, V 1997, 'Circuit Properties of Coils', IEE Proc. Sci. Meas. Technol., vol. 144, no. 5, pp. 234-239.

Aubin, G, Sapriel, J, Molchanov, VY, Gabet, R, Grosso, P, Gosselin, S & Jaouen, Y 2004, 'Multichannel acousto-optic cells for fast optical crossconnect', Electron. Lett., vol. 40, no. 7, pp. 448-449.

Auslender, M & Hava, S 1992, 'Free carrier contribution to dynamic dielectric function of heavily doped semiconductors. Application to n-type silicon', Physica Status Solidi B, vol. 174, no. 2, pp. 565-574.

Bartoli, M, Reatti, A & Kazimierczuk, MK 1994, 'Modeling of iron-powder inductors at high frequencies', Proc. IEEE Industry Applications Conf., Denver, CO.

Bell, AG 1880, Apparatus for signaling and communicating, called 'Photophone', U.S. Patent 235199.

Bolduc, M, Taussig, AR, Rajamani, A, Dionne, GF & Ross, CA 2006, 'Magnetism and Magnetooptical Effects in Ce-Fe Oxides', IEEE Trans. Mag., vol. 42, no. 10, pp. 3093-3095.

Bona, GL, Germann, R & Offrein, BJ 2003, 'SiON high-refractive-index waveguide and planar lightwave circuits', IBM J. Res. Dev., vol. 47, pp. 239-249.

Boudiara, T, Payet-Gervya, B, Blanc-Mignona, MF, Rousseaua, JJ, Le Berreb, M & Joistenc, H 2004, 'Magneto-optical properties of yttrium iron garnet (YIG) thin films

elaborated by radio frequency sputtering', J. Magnetism Mag. Materials, vol. 284, pp. 77-85.

Brooke, GH & Kharadly, MMZ 1976, 'Step discontinuities on dielectric waveguide', Electron. Lett., vol. 12, pp. 473-475.

Brown, TG, Bradfield, PL, Hall, DG & Soref, RA 1987, 'Optical emission from impurities within an epitaxial silicon optical waveguide', Optics Lett., vol. 12, no. 9, pp. 753-755.

Callon, R, Doolan, P, Feldman, N, Fredette, A, Swallow, G & Viswanathan, A 1997, 'A Framework for Multiprotocol Label Switching', Internet Draft.

Canon Inc. 2012, Canon Inc., Tokyo, Japan, <http://www.canon.com/technology/detail/device/soi/index.html>

Celler, GK & Cristoloveanu, S 2003, 'Frontiers of silicon-on-insulator', J. App. Phys., vol. 93, no. 9, pp. 4955-4978.

Chan, SP, Png, CE, Lim, ST, Reed, GT & Passaro, VMN 2005, 'Single mode and polarization independent SOI waveguides with small cross section', J. Lightwave Tech., vol. 23, no. 6, pp. 1573-1582.

Chen, C, Zhang, F, Wang, H, Sun, X, Wang, F, Cui, Z & Zhang, D 2011, 'UV Curable Electro-Optic Polymer Switch Based on Direct Photodefinition Technique', IEEE J. Quantum Electron., vol. 47, no. 7, pp. 959-964.

Chen, Q, Wu, W, Mao, H, Du, B, Li, L & Hao, Y 2010, 'Dualfunctional MEMS Optical Device with Compound Electrostatic Actuators for Compact and Flexible Photonic Networks', IEEE Conf. Sensors, pp. 2061-2064.

Chiang, KS 1994, 'Review of numerical and approximate methods for the modal analysis of general optical dielectric waveguides', Opt. Quantum Electron., vol. 26, pp. S113-S134.

Chiang, YC, Chiou, YP and Chang, HC 2002, 'Improved Full-Vectorial Finite-Difference Mode Solver for Optical Waveguides With Step-Index Profiles', J. Lightwave Tech., vol. 20, no. 8, pp. 1609-1618.

Chung, Y & Dagli, N 1995, 'Experimental and theoretical study of turning mirrors and beam splitters with optimized waveguide structures', Opt. Quantum Electron., vol. 27, no. 5, pp. 305-403.

Cisco Systems Inc. 2011, 'Global IP Traffic Forecast and Methodology 2010-2015'.

Cowin, M 2001, 'Manufacturers Poised to Profit from Polymeric Breakthroughs', Fibre Systems Europe, pp. 113-118.

Cristoloveanu, S 2001, 'Silicon on insulator technology and devices: from present to future', Solid State Electron. vol. 45, pp. 1403-1411.

Curtis, A, Bisson, P, Hamel, C & Hughlett, E 2002, 'Minimum Consumption Wafer Coating', Proc. 8th Int. Symposium Adv. Packaging Materials, pp. 302-310.

d'Agostino, R & Flamm, DL 1981, 'Plasma etching of Si and SiO_2 in SF_6/O_2 mixtures', J. App. Phys., vol. 52, no. 1, pp. 162-167.

Damask, J 2005, Polarization Optics in Telecommunications, Springer, New York.

Day, I, Evans, I, Knights, A, Hopper, F, Roberts, S, Johnston, J, Day, S, Luff, J, Tsang, H & Asghari, M 2003, 'Tapered silicon waveguides for low insertion-loss highly efficient high-speed electronic variable attenuators', OFC 2003, vol. 1, pp. 249-251.

Deck, RT, Mirkov, M & Bagley, BG 1998, 'Determination of Bending Losses in Rectangular Waveguides', J. Lightwave Tech., vol. 16, no. 9, pp. 1703-1714.

Didosyan, YS & Barash, VY 1995, 'Faraday effect in yttrium orthoferrite in the range 1280-1600 nm', J. Magnetism Mag. Materials, vol. 151, pp. 207-210.

Didosyan, YS, Hauser, H & Reider, GA 2002, 'Magneto-optic switch based on domain wall motion in orthoferrites', IEEE Trans. Mag., vol. 38, no. 5, pp. 3242-3245.

Donisi, D, Bellini, B, Beccherelli, R, Asquini, R, Gilardi, G, Trotta, M, & d'Alessandro, A 2010, 'A Switchable Liquid-Crystal Optical Channel Waveguide on Silicon', IEEE J. Quantum Electron., vol. 46, no. 5, pp. 762-768.

Dowell, PL 1966, 'Effects of eddy currents in transformer windings', Proc. IEE, vol. 113, no. 8, pp. 1287-1394.

Eisele, KM 1981, 'SF_6, a Preferable Etchant for Plasma Etching Silicon', J. Electrochem. Soc., vol. 128, pp. 123-126.

Eschenfelder, AH 1980, Magnetic Bubble Technology, 2nd edn, Springer Verlag, New York.

Faraday, M 1855, Experimental Researches in Electricity, vol. III, London.

Feit, MD & Fleck, JA 1978, 'Light propagation in graded-index optical fibers', App. Optics, vol. 17, pp. 3990-3998.

Feynman, RP 1960, 'There's Plenty of Room at the Bottom', Engineering & Science, vol. 23, no. 5, pp. 22-36.

Flanagan, WM 1986, Handbook of Transformer Applications, McGraw-Hill, New York.

Fletcher, R 1980, Practical Methods of Optimization, 1st edn, Wiley, Chichester.

Foresi, JS, Black, MR, Agarwal, AM & Kimerling, LC 1996, 'Losses in polycrystalline silicon waveguides', App. Phys. Lett., vol.68, no.15, pp.2052-2054.

Fratello, VJ, Licht, SJ & Brandle, CD 1996, 'Innovative improvements in bismuth doped rare-earth iron garnet Faraday rotators', IEEE Trans. Mag., vol. 32, no. 5, pp. 4102-4107.

Fratello, VJ, Licht, SJ & Brandle, CD 1999, 'Compositional design of Faraday rotator materials, in multicomponent oxide films for electronics', Proc. Materials Research Soc. Symp., vol. 574, pp. 225-236.

Fratello, VJ, Licht, SJ, Brandle, CD & O'Connor, RG 1997, 'Nucleation induced coercivity in Faraday rotator garnets', Proc. Int. Symp. Laser and Nonlinear Optical Materials, pp. 59-66.

Gao, Q, Li, L & Niu, G 2010, 'Research on Aircraft Skin Cracks Recognition Based on the Crack-Isolated Method', ICBECS, pp. 1-4.

Ghosh, S, Steuerman, DW, Maertz, B, Ohtani, K, Xu, H, Ohno, H & Awschalom, DD 2008, 'Electrical control of spin coherence in ZnO', App. Phys. Lett., vol. 92, no. 16, pp. 162109-162109-3.

Gomez, S, Jun Belen, R, Kiehlbauch, M & Aydil, ES 2004, 'Etching of high aspect ratio structures in Si using SF_6/O_2 plasma', J. Vac. Sci. Tech. A, vol. 22, no. 3, pp. 606-615.

Goodberlet, JG, Hastings, JT & Smith, HI 2001, 'Performance of the Raith 150 electron-beam lithography system', J. Vac. Sci. Tech. B, vol. 19, no. 6, pp. 2499-2503.

Gould, RW 1955, 'A coupled mode description of the backward wave oscillator and the Kompfner dip condition', IRE Trans. Electron Devices,, vol. PGED-2, pp. 37-42.

Goyal, IC, Gallawa, RL & Ghatak, AK 1987, 'Bent Planar Waveguides and Whispering Gallery Modes: A New Method of Analysis', J. Lightwave Tech., vol. 11, no. 12, pp. 2206.

Grandi, G, Casedei, D & Reggiani, U 1997 'Equivalent Circuit of Mush Wound AC Windings for High Frequency Analysis', ISIE, vol. 1, pp. 7-11.

GranOpt Co. Ltd. 2012, GranOpt Co. Ltd., Akita, Japan, <http://www.granopt.jp>

Greene, JM 1965, 'Calculation of the singularities of a magnetic field (External magnetic field necessary to support hydromagnetic configuration)', Physics of Fluids, vol. 8, no. 4, pp. 704-707.

Grossner, NR 1983, Transformers for Electronic Circuits, 2nd edn, McGraw-Hill, New York.

Grzegorczyk, TM & Kong, JA 2005, 'Visualization of Faraday Rotation and Optical Activity at Oblique Incidence', IEEE Antennas and Prop. Magazine, vol. 47, no. 5, pp. 23-33.

Guillemot, C, Henry, M, Clerot, F, LeCorre A, Kervaree, J, Dupas, A & Gravey, P 2000, 'KEOPS Optical Packet Switch Demonstrator : Architecture and Test Bed Performance', Optical Fiber Comm. Conf., vol. 3, pp. 204-206.

Gumaste, A & Chlamtac, I 2003, 'Light-trails : A Novel Conceptual Framework for Conducting Optical Communications', 3rd IEEE Workshop on HPSR, Proc. HPSR, pp. 24-27.

Hadamard, J 1902, 'Sur les problèmes aux dérivées partielles et leur signification physique', Princeton Univ. Bulletin, vol. 13, pp. 49-52.

Halldorsson, J, Arnfinnsdottir, NB, Jonsdottir, AB, Agnarsson, B & Leosson, K 2010, 'High index contrast polymer waveguide platform for integrated biophotonics', Opt. Express, vol. 18, pp. 16217-16226.

Hashizume, Y, Tsuchizawa, T, Watanabe, T, Yamada, K, Itabashi, S, Nasu, Y & Itoh, M 2010, 'Improvement in extinction ratio of silicon-silica hybrid thermooptic switch by using UV laser trimming technique', OECC, pp. 80-81.

Heiblum, M & Harris, JH 1975, 'Analysis of curved optical waveguides by conformal transformation', IEEE J. Quantum Electron., vol. 11, no. 2, pp. 75-83.

Hill, B 1984, 'Magneto-optic light switching array for electrophotographic printing', IEEE Trans. Mag., vol. 20, no. 5, pp. 978-982.

Hockham, GA & Sharpe, AB 1972, 'Dielectric-waveguide discontinuities', Electron. Lett., vol. 8, pp. 230-231.

Holzmann, GJ & Pehrson, B 1994, The Early History of Data Networks, 1st edn, Wiley - IEEE Comp. Soc.

Hunt, RP 1967, 'Magneto-optic scattering from thin solid films', J. App. Phys., vol. 38, pp. 1652-1671.

IceMOS Technology Ltd. 2012, IceMOS Technology Ltd., Belfast, Ireland, <http://www.icemostech.com/ice/SOIQuote/soi.aspx>

Integrated Photonics Inc. 2012, Integrated Photonics Inc., Hillsborough, New Jersey, <http://www.integratedphotonics.com>

Jackson, JD 1998, Classical Electrodynamics, 3rd edn, Wiley, New York.

Jalali, B 1997, 'Silicon-on-insulator photonic integrated circuit (SOI-PIC) technology', Proc. SPIE, vol. 2997, pp. 60-71.

Jansen, HV, Gardeniers, JGE, de Boer, MJ, Elwenspoek, MC & Fluitman, JHJ 1996, 'A survey on the reactive ion etching of silicon in microtechnology', J. Micromech. Microeng., vol. 6, pp. 14-28.

Jutty, MK, Swaminathan, V & Kazimierczuk, MK 1993, 'Frequency characteristics of ferrite core inductors', Proc. IEEE Electrical Manufacturing and Coil Winding Symp., Chicago, IL.

Kahn, FJ, Pershan, PS & Remeika, JP 1969, 'Ultraviolet Magneto-Optical Properties of Single-Crystal Orthoferrites, Garnets, and Other Ferric Oxide Compounds', Phys. Rev., vol. 186, no. 3, pp. 891-918.

Kalandadze, L 2008, 'Influence of Implantation on the Magneto-Optical Properties of Garnet Surface', IEEE Trans. Mag., vol. 44, no. 11, pp. 3293-3295.

Kaminow, IP & Stulz, LW 1978, 'Loss in cleaved Ti-diffused LiNbO3 waveguides', App. Phys. Lett., vol. 33, pp. 62-64.

Kao, KC & Hockham GA 1966, 'Dielectric surface waveguide for optical frequencies', Proc. IEE, vol. 113, pp. 1151-1158.

Kapron, FP, Keck, DB & Maurer, RD 1970, 'Radiation losses in glass optical waveguides', App. Phys. Lett., vol. 17, pp. 423-425.

Kawachi, M 1990, 'Silica waveguides on silicon and their application to integrated-optic components', Opt. Quantum Electron., vol. 22, no. 5, pp. 391-416.

Kemmet, S, Mina, M & Weber, RJ 2011, 'Magnetic pulse generation for high-speed magneto-optic switching', J. App. Phys., vol. 109, no. 7, pp. 07E333-07E333-3.

Kikkawa, JM & Awschalom, DD 2008, 'Resonant Spin Amplification in n-Type GaAs', Phys. Rev. Lett., vol. 80, no. 19, pp. 4313-4316.

Kirkpatrick, S, Gelatt, CD & Vecchi, MP 1983, 'Optimization by Simulated Annealing', Science, vol. 220, pp. 671-680.

Kissa, K, Yi-Yan, A, Murphy, E, Lafaw, D, Hallemeier, P, Maack, D, Attanasio, D, Fritz, D, McBrien, G & Bossi, D 2000, 'A review of lithium niobate modulators for fiber-optic communications systems', J. Select Topics in Quantum Electron., vol. 6, no. 1, pp. 69-82.

Kobrinsky, MJ, Block, BA, Zheng, JF, Barnett, BC, Mohammed, R, Reshotko, M, Robertson, F, List, S, Young, I & Cadien, K 2004, 'On-chip optical interconnects', Intel Technol. J., vol. 8, pp. 129-141.

Kogelnik, H 1969, 'Coupled wave theory for thick hologram gratings', Bell Systems Tech. J. , vol, 48, pp. 2909-2947.

Kron, G 1939, 'Tensor Analysis of Networks', Wiley, New York.

Krumme, JP, Doorman, V & Eckart, R 1984, 'Bismuth-substituted Iron garnet films prepared by RF diode sputtering', IEEE. Trans. Mag., vol. 20, no. 5, pp. 983-985.

Kuratani, Y & Kadota, M 2010, 'High-speed and low driving voltage $LiNbO_3$ optical switch composed of new structure', CLEO, pp. 1-2.

Kurokawa, K 1965, 'Power Waves and the Scattering Matrix', IEEE Trans. MTT, vol. 13, no. 2, pp. 194-202.

Lammeraner, J & Stafl, M 1964, Eddy Currents, CRC Press, Cleveland.

Landau, LD & Lifschitz, EM 1984, Electrodynamic of Continuous Media, 2nd edn, Pergamon Press, New York.

Laslett, LJ 1966, 'An equivalent distribution of surface currents for the generation of a prescribed static magnetic field within an enclosed volume', J. App. Phys., vol. 37, no. 6, pp. 2361-2363.

Lorentz, HA 1915, The Theory of Electrons, 1st edn, B. G. Teubner, Leipzig.

Louisell, WH 1954, 'Analysis of the single tapered mode coupler', Bell Systems Tech. J., vol. 33, pp. 853-871.

Luff, B, Feng, D, Lee, D, Qian, W, Liang, H & Asghari, M 2008, 'Hybrid silicon photonics for low-cost high-bandwidth link applications', Adv. Opt. Tech., vol. 2008, pp. 1-6.

Mach, L 1892, 'Über einen Interferenzrefraktor', Z. Instrumentenkunde, vol. 12, pp. 89-93.

Maiman, TH 1960, 'Stimulated optical radiation in ruby', Nature, vol. 187, pp. 493-494.

Marcuse, D 1971, 'The coupling of degenerate modes in two parallel dielectric waveguides', Bell Systems Tech. J., vol. 50, pp. 1791-1816.

Marcuse, D 1972, Light Transmission Optics, 1st edn, Van Nostrand Reinhold, New York.

Massarini, A & Kazimierczuk, MK 1996, 'Modeling the Parasitic Capacitance of Inductors', Proc. of 16th Cap. Res. Tech. Symp. (CARTS 96), New Orleans, pp. 78-85.

Maszara, WP, Dockerty, R, Gondran, CFH & Vasudev, PK 1997, 'SOI materials for mainstream CMOS technology', Proc. Electrochem. Soc., vol. 97, pp. 15-26.

Matthews, EW 1955, 'The Use of Scattering Matrices in Microwave Circuits', IRE Trans. MTT, vol. 3, no. 3, pp. 21-26.

Maurice, D & Minns, RH 1947, 'Very-wide-band radio frequency transformers', Wireless Eng., vol. 24, pp. 168.

Maxwell, JC 1904, A Treatise on Electricity and Magnetism, Clarendon Press, Oxford.

Medhurst, RG 1947, 'H. F. Resistance and Self Capacitance of Single-Layer Solenoids', Wireless Engr., vol. 24, pp. 35-43.

Merkel, P 1987, 'Solution of stellarator boundary value problems with external currents', Nuclear Fusion, vol. 27, no. 5, pp.867-871.

Metropolis, N, Rosenbluth, AW, Rosenbluth, MN, Teller, AH & Teller, E 1953, 'Equation of State Calculations by Fast Computing Machines', J. Chem. Phys., vol. 21, pp. 1087-1092.

Miller, SE 1954, 'Coupled wave theory and waveguide applications', Bell Systems Tech. J., vol. 33, pp. 661-719.

Miller, SE 1969, 'Integrated Optics: An Introduction', Bell Systems Tech. J., vol. 48, pp. 2059-2068.

Milosevic, M, Matavulj, P, Timotijevic, B, Reed, G & Mashanovich, G 2008, 'Design rules for singlemode and polarization-independent silicon-on-insulator rib waveguides using stress engineering', J. Lightwave Tech., vol. 26, pp. 1840-1846.

Milton, AF & Burns, WK 1979, 'Mode coupling in tapered optical waveguide structures and electro-optic switches', IEEE Trans. Circuits and Systems, vol. 26, no. 12, pp. 1020-1028.

Mitra, D, Romeo, F & Sangiovanni-Vincentelli, AL 1985, 'Convergence and finite-time behavior of simulated annealing', Proc. 24th Conf. Decision and Control, pp. 761-767.

Morse, SFB 1840, Telegraph Signs, U.S. Patent 1647.

Moses, AJ, Williams, PI & Hoshtanar, OA 2005, 'A novel instrument for real-time dynamic domain observation in bulk and micromagnetic materials', IEEE. Trans. Mag., vol. 41, no. 10, pp. 3736-3738.

Nomura, T, Kishida, M, Hayashi, N & Ishibashi, T 2011, 'Evaluation of Garnet Film as Magneto-Optic Transfer Readout Film', IEEE Trans. Mag., vol. 47, no. 8, pp. 2081-2086.

Okuda, T, Katayama, T, Kobayashi, H, Kobayashi, N 1990, 'Magnetic properties of $Bi_3Fe_5O_{12}$ garnet', J. App. Phys., vol. 67, pp. 4944-4946.

Panmand, RP, Kumar, G, Mahajan, SM, Kulkarni, MV, Amalnerkar, DP, Kale, BB & Gosavi, SW 2011, 'Functionality of bismuth sulfide quantum dots/wires-glass nanocomposite as an optical current sensor with enhanced Verdet constant', J. App. Phys., vol. 109, no. 3, pp. 033101-033101-7.

Paoletti, A 1978, Physics of Magnetic Garnets, North-Holland Publishing Co., Amsterdam.

Park, HS, Song, KY, Yun, SH & Kim, BY 2001, 'All-fiber wavelength tunable acousto-optic switch', OFC 2001, vol. 3, pp. 1-3.

Payne, FP & Lacey, JPR 1994, 'A theoretical analysis of scattering loss from planar optical waveguides', Opt. Quantum Electron., vol. 26, no. 10, pp. 977-986.

Pedrotti, FL, Pedrotti, LM & Pedrotti, LS 2007, Introduction to Optics, 3rd edn, Addison-Wesley, New Jersey.

Phoenix Software 2012, FieldDesigner, Enschede, Netherlands, <http://www.phoenixbv.com/product.php?prodid=50020101&submenu=dfa&prdgrpID=3&prodname=FieldDesigner>

Phoenix Software 2012, OptoDesigner - BPM Simulation Engine, Enschede, Netherlands, <http://www.phoenixbv.com/product.php?prodid=50021101&submenu=dfa&prdgrpID=3&prodname=OptoDesigner - BPM simulation engine>

Pierce, JR 1954, 'Coupling of modes of propagation', J. App. Phys., vol. 25, pp. 179-183.

Pogossian, SP, Vescan, L & Vonsovici, A 1998, 'The Single-Mode Condition for Semiconductor Rib Waveguides with Large Cross-section', J. Lightwave Tech., vol. 16, no. 10, pp. 1851-1853.

Powell, JR 2008, 'The Quantum Limit of Moore's Law', Proc. IEEE, vol. 96, no. 8, pp. 1247-1248.

Pross, E, Tolksdorf, W & Dammann, H 1988, 'Yttrium iron garnet single-mode buried channel waveguides for waveguide isolators', App. Phys. Lett., vol. 52, pp. 682-684.

PureBand® Zero Water Peak Fiber Specification 2008, Sumitomo Electric Lightwave Corp., Research Triangle Park, NC.

Qiao, C & Yoo, M 1999, 'Optical Burst Switching (OBS) - A New Paradigm for an Optical Internet', J. High Speed Networks, vol. 8, pp. 69-84.

Ray, S & Mittra, R 1984, 'Numerical analysis of open waveguide discontinuities', Radio Sci., 1984, vol. 19, pp. 1289-1293.

Rosen, E, Viswanathan, A & Callon, R 1997, 'A Proposed Architecture for MPLS', Internet draft.

Rozzi, TE 1978, 'Rigorous Analysis of the Step Discontinuity in a Planar Dielectric Waveguide', IEEE Trans. MTT, vol. 26, no. 10, pp. 738-746.

Sabapathia, T & Sundaravadivelub, S 2010, 'Analysis of bottlenecks in DWDM fiber optic communication system', Optik - Intl. J. Light and Electron Optics, vol. 122, no. 16, pp. 1453-1457.

Sagnac, G 1913a, 'The demonstration of the luminiferous aether by an interferometer in uniform rotation', Comptes Rendus, vol. 157, pp. 708-710.

Sagnac, G 1913b, 'On the proof of the reality of the luminiferous aether by the experiment with a rotating interferometer', Comptes Rendus, vol. 157, pp. 1410-1413.

Sapriel, J, Charissoux, D, Voloshinov, V & Molchanov, V 2002, 'Tunable Acoustooptic Filters and Equalizers for WDM Applications', J. Lightwave Tech., vol. 20, no. 5, pp. 892-899.

Shaoying, K, Shizhuo, Y, Adyam, V, Qi, L & Yong, Z 2007, 'Bi_3 $Fe_4Ga_1O_{12}$ Garnet Properties and Its Application to Ultrafast Switching in the Visible Spectrum', IEEE Trans. Mag., vol. 43, pp. 3656-3660.

Shirasaki, M, Wada, F, Takamatsu, H, Nakajima, H & Asama, K 1984, 'Magnetooptical 2x2 switch for single-mode fibers', App. Optics, vol. 23, no. 19, pp. 3271-3276.

SMF-28e Optical Fiber Specification 2004, Corning Incorporated., Corning, NY.

Snyder, AW 1972, 'Coupled mode theory for optical fibers', J. Opt. Soc. Am., vol. 62, pp. 1267-1277.

Soitec 2012, Soitec, Bernin, France, <http://www.soitec.com/en/technologies/smart-cut/>

Soref, RA & Lorenzo, JP 1985, 'Single-crystal Silicon-A new material for 1.3 and 1.6μm integrated-optical components', Electron. Lett., vol. 21, pp. 953-954.

Soref, RA, Schmidtchen, J & Peterman, K 1991, 'Large Single-Mode Rib Waveguides in GeSi-Si and Si-on-SiO_2', IEEE J. Quantum Electron., vol. 27, no. 8, pp. 1971-1974.

Sparacin, DL, Spector, SJ & Kimerling, LC 2005, 'Silicon waveguide sidewall smoothing by wet chemical oxidation', J. Lightwave Tech., vol. 23, no. 8, pp.2455-2461.

Sudbo, AS 1992, 'Why are accurate computations of mode fields in rectangular dialectic waveguides difficult?', J. Lightwave Tech., vol. 10, no. 4, pp. 418-419.

Sudbo, AS 1993, 'Film mode matching : a versatile numerical method for vector mode field calculations in dielectric waveguides', Pure App. Opt., vol. 2, no. 3, pp. 211-233.

Sugimoto, N, Terui, H, Tate, A, Katoh, Y, Yamada, Y, Sugita, A, Shibukawa, A & Inoue, Y 1996, 'A hybrid integrated waveguide isolator on a silica-based planar waveguide circuit', J. Lightwave Tech., vol. 14, pp. 2537-2546.

Suzuki, J, Komai, A, Ohuchi, Y, Tezuka, Y, Konishi, H, Nishiyama, M, Suzuki, Y & Owa, S 2008, 'Micro-mirror On Ribbon-actuator (MOR) for high speed spatial light modulator', IEEE Conf. MEMS, pp. 762-765.

Takeuchi, H, Shinagawa, K & Taniguchi, S 1973, 'Faraday Effect of Bi-Substituted Rare-Earth Iron Garnet', Japanese J. App. Phys., vol. 12, no. 3, pp. 465.

Thurber, WR, Mattis, RL, Liu, YM & Filliben, JJ 1981, Semiconductor Measurement Technology: The Relationship Between Resistivity and Dopant Density for Phosphorus- and Boron-Doped Silicon, 1st edn, National Bureau of Standards, Washington D.C.

Tikhonov, AN & Arsenin, VY 1977, Solutions of Ill-Posed Problems, Winston, New York.

Tkachuk, S, Bowen, D, Krafft, C & Mayergoyz, I 2008, 'Controllability of Anisotropy of Bi and Pr Containing Garnet Films Grown on (210)-Oriented Substrates', IEEE Trans. Mag., vol. 44, pp. 3307-3310.

Tkachuk, S, Fratello, VJ, Krafft, C, Lang, G & Mayergoyz, ID 2009, 'Imaging capabilities of Bismuth Iron Garnet films with low growth induced uniaxial anisotropy', IEEE Trans. Mag., vol. 45, no. 10, pp. 4238-4241.

Tsang, CH, White, RM & White, RL 1978, 'Transit-time measurements of domain-wall mobilities in $YFeO_3$', J. App. Phys., vol. 49, no. 12, pp. 6052-6062.

Turner, R 1986, 'A target field approach to optimal coil design', J. Phys. D, App. Phys., vol. 19, pp. 147-151.

Van Laarhoven, PJ & Aarts, EH 1987, Simulated Annealing : Theory and Applications, Kluwer Academic Publishers, Norwell.

Van Vleck, JH 1932, The Theory of Electronic and Magnetic Susceptibility, 1st edn, Oxford University Press, New York.

Volterra, H & Zimmerman, M 2000, 'Indium Phosphide Benefits High-Performance Transmission', WDM Solutions, pp. 47-49.

Wakao, K, Soda, H & Kotaki, Y 1999, 'Semiconductor Optical Active Devices for Photonics Networks', Fujitsu Scien. Tech. J., vol. 35, pp. 100-106.

Wang, W, Zhao, Y, Zhou, H, Hao, Y, Yang, J, Wang, M & Jiang, X 2011, 'CMOS-Compatible 1x3 Silicon Electrooptic Switch with Low Crosstalk', IEEE Phot. Tech. Lett., vol. 23, no. 11, pp. 751-753.

White, AD, McHale, GB & Goerz, DA 2010, 'Advances in Optical Fiber-Based Faraday Rotation Diagnostics', IEEE PPC, pp. 1358-1363.

White, SR 1984, 'Concepts of Scale in Simulated Annealing', Proc. IEEE Intnl. Conf. on Computer Design, pp. 646-651.

Xu, CL & Huang, WP 1995, 'Finite difference beam propagation method for guided wave optics', Progress in Electromagnetics Res., vol. 11, pp. 1-49.

Yariv, A & Taylor, HF 1981, 'Guided-wave optics', Proc. IEEE, vol. 62, pp. 131-134.

Yariv, A 1973, 'Coupled mode theory for guided-wave optics', IEEE J. Quantum Electron., vol. QE-9, pp. 919-933.

Zeeman, P 1897, 'On the influence of Magnetism on the Nature of the Light emitted by a Substance', Phil. Mag., vol. 43, pp. 226-236.

Zehnder, L 1891, 'Ein neuer Interferenzrefraktor', Z. Instrumentenkunde, vol. 11, pp. 275-285.

Zhang, H, Yang, Q & Bai, F 2011, 'Microwave/Millimeter-Wave Garnet Films', IEEE Trans. Mag., vol. 47, no. 2, pp. 295-299.

Zhong, T, Zhang, XM, Liu, AQ, Li, J, Lu, C & Tang, DY 2007, 'Thermal-Optic Switch by Total Internal Reflection of Micromachined Silicon Prism', IEEE J. Sel. Topics Quantum Electron., vol. 13, no. 2, pp. 348-358.